

4

GL-TR-89-0292

AD-A220 417

Kinetic and Extraction Measurements on
 $^{12}\text{C}^{18}\text{O}_2$

y

C.H. Fisher
C.E. Hamilton
R.D. Mead
A.L. Pindroh

Spectra Technology, Inc.
2755 Northup Way
Bellevue, WA 98004-0460

31 October 1989

Final Report

6 September 1988 - 5 August 1989

DTIC
ELECTE
APR 10 1990
S B D

GEOPHYSICS LABORATORY
AIR FORCE SYSTEMS COMMAND
UNITED STATES AIR FORCE
HANSCOM AIR FORCE BASE, MASSACHUSETTS 01731-5000

DISTRIBUTION STATEMENT A

Approved for public release;
Distribution Unlimited

90

REPORT DOCUMENTATION PAGE

Form Approved
OMB No. 0704-0188

1a. REPORT SECURITY CLASSIFICATION Unclassified		1b. RESTRICTIVE MARKINGS	
2a. SECURITY CLASSIFICATION AUTHORITY		3. DISTRIBUTION/AVAILABILITY OF REPORT Approved for public release, distribution unlimited	
2b. DECLASSIFICATION/DOWNGRADING SCHEDULE		5. MONITORING ORGANIZATION REPORT NUMBER(S) GL-TR-89-0292	
4. PERFORMING ORGANIZATION REPORT NUMBER(S)		7a. NAME OF MONITORING ORGANIZATION Geophysics Laboratory	
6a. NAME OF PERFORMING ORGANIZATION Spectra Technology, Inc.	6b. OFFICE SYMBOL (If applicable)	7b. ADDRESS (City, State, and ZIP Code) Hanscom AFB Massachusetts 01731-5000	
6c. ADDRESS (City, State, and ZIP Code) 2755 Northup Way Bellevue, WA 98004-0460	8b. OFFICE SYMBOL (If applicable)	9. PROCUREMENT INSTRUMENT IDENTIFICATION NUMBER F19628-88-C-0141	
8a. NAME OF FUNDING/SPONSORING ORGANIZATION	8b. OFFICE SYMBOL (If applicable)	10. SOURCE OF FUNDING NUMBERS	
8c. ADDRESS (City, State, and ZIP Code)	PROGRAM ELEMENT NO. 62101F	PROJECT NO. 7670	TASK NO. 16 WORK UNIT OA
11. TITLE (Include Security Classification) Kinetic and Extraction Measurements on $^{12}\text{C}^{18}\text{O}_2$			
12. PERSONAL AUTHOR(S) C.H. Fisher, C.E. Hamilton, R.D. Mead, and A.L. Pindroh			
13a. TYPE OF REPORT Final Report	13b. TIME COVERED FROM 6 Sept 88 TO 5 Aug 89	14. DATE OF REPORT (Year, Month, Day) 1989 October 31	15. PAGE COUNT 90
16. SUPPLEMENTARY NOTATION Carbon Dioxide			
17. COSATI CODES		18. SUBJECT TERMS (Continue on reverse if necessary and identify by block number)	
FIELD	GROUP	Isotopic CO_2 Pulsed Laser Performance, $^{12}\text{C}^{18}\text{O}_2$ Isotope, Laser Gain Coefficient Measurements	
19. ABSTRACT (Continue on reverse if necessary and identify by block number) <u>Micrometer</u> A candidate transmitter source for a space borne pulsed Doppler wind-sensing lidar is the CO_2 laser. To minimize beam propagation losses due to atmospheric CO_2 extinction, a rare isotope is used as the active laser molecule. The particular rare isotope and laser transition is further determined by choosing a transition wavelength that minimizes the propagation losses and maximizes the backscatter coefficient of the atmospheric aerosol background. The $^{12}\text{C}^{18}\text{O}_2$ isotope R(20) transition at 9.11 μ coincides with a Sellmeyer resonance of predominant aerosol constituents and appears to be the optimum choice. The performance of a $^{12}\text{C}^{18}\text{O}_2$ laser capable of fulfilling the global wind-sensing mission was addressed analytically and experimentally in this study. Gain and collisional deactivation rate measurements were conducted in an x-ray preionized, self-sustained discharge laser tested, by observing the effect of propagation through the laser medium on a cw $^{12}\text{C}^{18}\text{O}_2$ laser probe beam. The kinetic rates derived from the measurements deviated significantly from similar published measurements for the abundant $^{12}\text{C}^{16}\text{O}_2$ isotope. The new rate <u>COA</u>			
20. DISTRIBUTION/AVAILABILITY OF ABSTRACT <input checked="" type="checkbox"/> UNCLASSIFIED/UNLIMITED <input type="checkbox"/> SAME AS RPT. <input type="checkbox"/> DTIC USERS		21. ABSTRACT SECURITY CLASSIFICATION Unclassified	
22a. NAME OF RESPONSIBLE INDIVIDUAL Steve Alejandro		22b. TELEPHONE (Include Area Code) (617) 377-7447	22c. OFFICE SYMBOL CL/OFA

BLOCK 18. Collisional Deactivation Rate Measurements, Extraction Efficiency Measurements, Laser Performance Scaling, Lasers for Global Wind Sensing.

Block 19. ^{↓ +10} ^{Microsecond} information was input into an existing kinetics code, and laser parameters required for a 10 J/pulse and 3 μs duration pulse were deduced. Extraction measurements were conducted using both x-ray preionized self-sustaining discharge and e-beam sustained discharge testbeds. Excellent agreement was observed between numerical predictions of the kinetics code, as updated by the measured kinetic rates, and the laser pulse characteristics observed experimentally (eg. the pulse power levels and temporal profiles). The increase in intrinsic efficiency predicted for laser gas mixtures having low helium content was verified by the experiments. Laser parameter scaling studies were conducted and the results were used to generate weight, size and efficiency estimates for on-orbit wind-sensing lidar transmitter.

Accession For	
NTIS GRA&I	<input checked="checked" type="checkbox"/>
DTIC TAB	<input type="checkbox"/>
Unannounced	<input type="checkbox"/>
Justification	
By	
Distribution/	
Availability Codes	
Dist	Avail and/or Special
A-1	



LIST OF FIGURES

Figure		Page
1-1	Atmospheric Transmittance Due to Molecular Absorption through a 10-km Horizontal Path at Sea Level.	1-5
1-2	Ozone Absorption spectrum in the CO ₂ Laser Wavelength Region at 30-km Altitude.	1-6
2-1	CO ₂ Vibrational Energy Levels and Transitions.	2-2
2-2	STI CO ₂ Kinetics Model	2-4
2-3	Boltzmann Solver Features	2-5
2-4	Discharge Power into Vibrational Modes for He/N ₂ /CO ₂ = 3/2/1 as a Function of E/N.	2-6
2-5	Discharge Energy into Vibrational Modes as a Function of E/N for the Gas Mix Used in the Lucy and Delilah Experiments	2-8
2-6	Fraction of Energy into the Sum of N ₂ and CO ₂ (ν ₃) Vibrational Modes for Two Gas Mixes Studied in the Experiments	2-9
3-1	Schematic Diagram of Lucy X-Ray Preionized Discharge Amplifier	3-3
3-2	Lucy Glass Tube Upgrade	3-4
3-3	Typical Voltage and Current Traces for the Discharge of Glass Lucy	3-5
3-4	Experimental Setup for the Deactivation and Gain Measurement	3-7
3-5	Typical Amplified Probe Signal for 828 CO ₂ II P(18) Transition.	3-11
3-6	ln(g _a) vs t for 250/50/10 He/N ₂ /CO ₂ Mix Calculated from the Trace of Figure 3-5	3-12
3-7	Schematic Diagram of Energy Transfer Processes for CO ₂ Lasers.	3-14
3-8	Collisional Decay Rate for C ¹⁸ O ₂ (00 ⁰ 1) Level as a Function of He Pressure.	3-16
3-9	Collisional Decay Rate for C ¹⁸ O ₂ (00 ⁰ 1) Level as a Function of N ₂ Pressure.	3-17

3-10	Collisional Decay Rate for $C^{18}O_2$ (00^0_1) Level as a Function of CO_2 Pressure.	3-18
4-1a	Experimental Voltage and Current	4-3
4-1b	Experimental and Theoretical Output Flux	4-3
4-2	Extracted Energy as a Function of Energy into the Discharge ($E_{dis} = \int V \cdot Idt$) and the II R(20) Line of $^{12}C^{18}O_2$ in Gas Mixture for the Lucy Self-sustained Discharge Laser.	4-6
4-3a	Experimental Voltage and Current.	4-8
4-3b	Experimental and Theoretical Output Flux.	4-8
4-4a	Experimental Voltage and Current.	4-9
4-4b	Experimental and Theoretical Output Flux.	4-9
5-1	General Overall Electrical Schematic of Delilah e-Beam Sustained Discharge Laser.	5-3
5-2	Delilah e-Beam Sustained Discharge Laser.	5-4
5-3a	Delilah: Experimental Voltage and Current.	5-6
5-3b	Delilah: Experimental and Theoretical Output Flux.	5-6
5-4a	Delilah: Experimental Voltage and Current.	5-7
5-4b	Delilah: Experimental and Theoretical Output Flux.	5-7
5-5a	Delilah: Experimental Voltage and Current.	5-8
5-5b	Delilah: Experimental and Theoretical Output Flux.	5-8
5-6	Model Predictions of the Peak Small Signal Gain as a Function of Energy Loading.	5-10
5-7	Energy Loading as a Function of Position Between the Electrodes for both e-Beam and Self-sustained Discharges.	5-12
5-8	Efficiency vs E/N for the e-Beam Sustained Discharge.	5-16
6-1	Boltzmann code Predictions Showing the Fractional Energy Distribution into the CO_2 and N_2 Vibrational Modes as a Function of E/N.	6-3
6-2	Fractional Energy Transfer into $CO_2 \nu_3 + N_2$ Vibrational Modes as a Function of E/N for Two Gas Mixtures Used in the Experiments of Sections 4 and 5.	6-4

6-3	Fractional Energy Transfer into CO_2 ν_3 + N_2 Vibrational Modes as a Function of N_2/CO_2 ratio for Three He Concentrations.	6-5
6-4	Projected Laser System Efficiency as a Function of N_2/CO_2 Ratio for Three He Concentrations.	6-7
6-5	Projected Laser System Efficiency as a Function of Pump Energy for Two Gas Mixtures.	6-8
6-6	Predicted Laser Pulse Shapes for Three Gas Mixtures, in a Self-Sustained Discharge Lasers.	6-9

LIST OF TABLES

Table		Page
2-1	CO ₂ Transition Dipole Moment Data	2-11
3-1	Operating Parameters for Lucy X-Ray Preionized Discharge Laser	3-6
3-2	Measured Decay Rates for He/N ₂ /CO ₂ Gas Mixture:	3-13
3-3	Quenching Rate Constants for the 00 ⁰ 1 Level	3-19
3-4	Small Signal Gains (He/N ₂ /CO ₂ = 325/50/25 torr)	3-22
4-1	R(20) Single-Line Extraction from Isotopic CO ₂ Excited by a Self-Sustained Discharge	4-10
5-1	R(20) Single-Line Extraction From Isotopic CO ₂ Excited by an E-beam Sustained Discharge	5-14

Section 1

INTRODUCTION

The goal of this program is to provide experimental data to construct and validate a reliable model to predict the performance of a candidate transmitter for on-orbit pulsed Doppler lidar for wind sensing, using $^{12}\text{C}^{18}\text{O}_2$ as the active molecule. The rationale for choosing the $^{12}\text{C}^{18}\text{O}_2$ isotope is discussed in this section. The body of knowledge about $^{12}\text{C}^{18}\text{O}_2$ lasers prior to this program was derived from cw low-signal gain measurements to extract optical transition probabilities and collisional deactivation rates under appropriate higher pressure excitation conditions. These measurements are described in Section 3. Using this baseline set of data as input to the STI laser performance codes described in Section 2, cavity designs were developed for self-sustained and e-beam sustained single-line extraction measurements, described in Sections 4 and 5, respectively. These experimental results have been used to update and improve the model. In Section 6, we compare laser performance using $^{12}\text{C}^{18}\text{O}_2$ with performance using $^{12}\text{C}^{16}\text{O}_2$ and examine the differences between e-beam and self-sustained excitation. In Section 7, we summarize the conclusions of our study.

1.1 GENERAL DISCUSSION

The choice of wavelength for long-range wind-sensing coherent laser radars requires careful consideration from both the atmospheric transmission and target reflectivity viewpoints. These properties can vary considerably over a relatively restricted wavelength region, e.g., that available using the CO_2 laser. Confining discussion to the CO_2 laser is justified for the near term by the current state of technology and the extensive efforts conducted world wide over the past 20 years in applying this laser to remote wind sensing. Consideration of other technologies for the source, e.g., eye-safe solid-state sources in the near-infrared, is premature for near-term deployment since the feasibility of such devices is only currently being investigated. The wavelength range of a CO_2 laser

spans the "so-called" 8 to 12- μ m atmospheric window, if rare-isotope variants are also considered. Within this spectral band, there are several important absorption bands due to standard atmospheric constituents (e.g., H_2O , O_3 , CO_2) as well as several minor (pollutant) constituents (e.g., SO_2 , NH_3 , C_2H_4). Naturally, the optimum choice of wavelength is that which avoids such bands, or less restrictively, strong lines within the bands. Also, within the 8 to 12- μ m band is a region of anomalous dispersion for characteristic atmospheric aerosol material. Such a region is characterized by large values of real and complex refractive indices which result in enhanced scattering properties and, thus, a positive factor for a laser radar source having this wavelength. Taking advantage of these factors translates into smaller transmitter optics and/or lower laser energy per pulse for a given lidar performance, which for an on-orbit lidar, translates into a more compact lidar with a decreased prime-power requirement.

1.2 BEAM TRANSMISSION CONSIDERATIONS

For a global wind-sensing space-lidar, it is important to evaluate the effects of CO_2 , H_2O and O_3 on transmission.

CO_2 - The transitions of a normal abundance isotope CO_2 laser match precisely the atmospheric CO_2 absorption bands. This has prompted the suggestion to use a rare CO_2 isotope as the active laser molecule. Since the abundance of a rare isotope is low, negligible atmospheric CO_2 attenuation or dispersion results. In comparison, the transmission of a zenith-pointed normal-abundance CO_2 laser beam, oscillating on the P20 transition is 53%. Alternate schemes have been proposed such as operating the laser off line-center, which also decreases the laser gain and does not totally eliminate atmospheric attenuation. The laser can be operated in the sequence-band mode, which utilizes the anharmonicity of the molecule to detune the laser from the conventional $\nu = 1 + \nu = 0$ transition to the $\nu = 2 + \nu = 1$ transition, such that the heavily populated ground state of atmospheric CO_2 does not contribute to extinction. Both these schemes have an adverse effect on overall laser efficiency and, thus, are undesirable from the viewpoint of a space lidar transmitter. Spectra Technology, Inc.

(STI) completed a wavelength assessment for a ground-based long-range lidar to operate through the atmosphere for MIT/Lincoln Laboratory in conjunction with the Firepond lidar upgrade. The $^{13}\text{C}^{16}\text{O}_2$ rare isotope was selected as the active laser molecule (which has transitions in the 10.7 to 11.3- μ region) and hardware based on this selection has been manufactured and delivered by STI.

H_2O - Water vapor extinction in the infrared is characterized by a weak continuum on which are superimposed narrow, strongly-absorbing lines. A weak minimum in the continuum occurs at 8.9 μm . Therefore, avoidance of the strongly-absorbing lines becomes the dominant requirement.

O_3 - All three vibrational frequencies of the O_3 molecule are active in infrared absorption. They form vibrational-rotational bands centered at $\nu_1 = 1110 \text{ cm}^{-1}$ (9.1 μm), $\nu_2 = 710 \text{ cm}^{-1}$ (14.1 μm) and $\nu_3 = 1043 \text{ cm}^{-1}$ (9.6 μm). The ν_1 band is very weak, with band strength only 1% of the ν_3 band. Avoidance of the 9.6- μm band becomes an absolute necessity for a long-range laser radar.

Minor Species - The average mixing ratio of various pollutant molecules (e.g., SO_2 , NH_3 , C_2H_4 , N_2O , HNO_3 , CH_4) are small and their contribution to the bulk extinction is negligible. All have spectra in the 8 to 12- μm wavelength region. Nevertheless, correspondence with strong absorption lines should be avoided to minimize extinction over localized areas that have an abundance of these pollutants.

1.3 PARTICULATE SCATTERING CROSS-SECTION CONSIDERATIONS

Measurement of the dispersion curves of atmospheric particulates⁽¹⁾ show a region of anomalous dispersion in the vicinity of 9 μm . At wavelengths corresponding to such regions, the light scattering effects of a given size particle is considerably enhanced. It has been postulated that the wavelength of choice for a wind-sensing lidar should be in the vicinity of 9 μm .

1.4 $^{12}\text{C}^{18}\text{O}_2$ LASER MOLECULE SELECTION RATIONALE

Combining the requirements of Sections 1.2 and 1.3 led to the choice of the $^{12}\text{C}^{18}\text{O}_2$ isotope for further analysis as the active molecule for an on-orbit wind-sensing lidar laser. This molecule has transitions in the vicinity of $9.1\ \mu\text{m}$, to enhance the expected backscattering, and, since it is a rare isotope, the extinction due to atmospheric CO_2 will be negligible. The $9.1\text{-}\mu\text{m}$ wavelength is also close to the minimum water vapor extinction wavelength. In addition, there is a slight improvement in the SNR for a coherent lidar as the wavelength is lowered due to antenna effects alone. Since it is the R-branch of the $\text{OO}^0_1 - (\text{10}^0_0 + \text{02}^0_0)_{11}$ mode of the $^{12}\text{C}^{18}\text{O}_2$ that has its transitions around $9.1\ \mu\text{m}$, a wavelength corresponding to the strongest line within this branch is selected for consideration, viz., the R20 transition at a wave number of $1097.15\ \text{cm}^{-1}$ ($9.1145\ \mu$). Figure 1-1 shows the AFCRL transmittance plot⁽²⁾ over a wave number range from 1040 to $1110\ \text{cm}^{-1}$. The plot shows that, in the vicinity of wave number $1097.15\ \text{cm}^{-1}$, there is very little structure. An intriguing possibility is the overlap of the 828 isotope R24 CO_2 line at $1099.46\ \text{cm}^{-1}$ with the water line at $1099.6\ \text{cm}^{-1}$, which could be used for water vapor dial measurements. Thus, the same laser could be used for both wind and DIAL measurement. Since the spectrum shown in Figure 1-1 is for ground level, the contribution from ozone is small. A review of measured ozone spectra obtained using balloon-borne instrumentation at 30 km (Figure 1-2) indicates that there is not a correspondence between 828 II R20 line at $1097.15\ \text{cm}^{-1}$ and the lines of the weak $9.1\text{-}\mu\text{m}$ ozone band. The selection of the R20 line appears to be appropriate from both the transmission and target reflectivity points of view. In addition, the lack of spectral correspondence with the spectra of all minor constituents (except SO_2) has been verified.

In assessing transmission losses from an on-orbit lidar, the effects of the Doppler shift ($\sim 1.5\ \text{GHz}$) of the transmitted beam, due to the spacecraft velocity ($7.5\ \text{km/sec}$), also need to be evaluated. This shift is

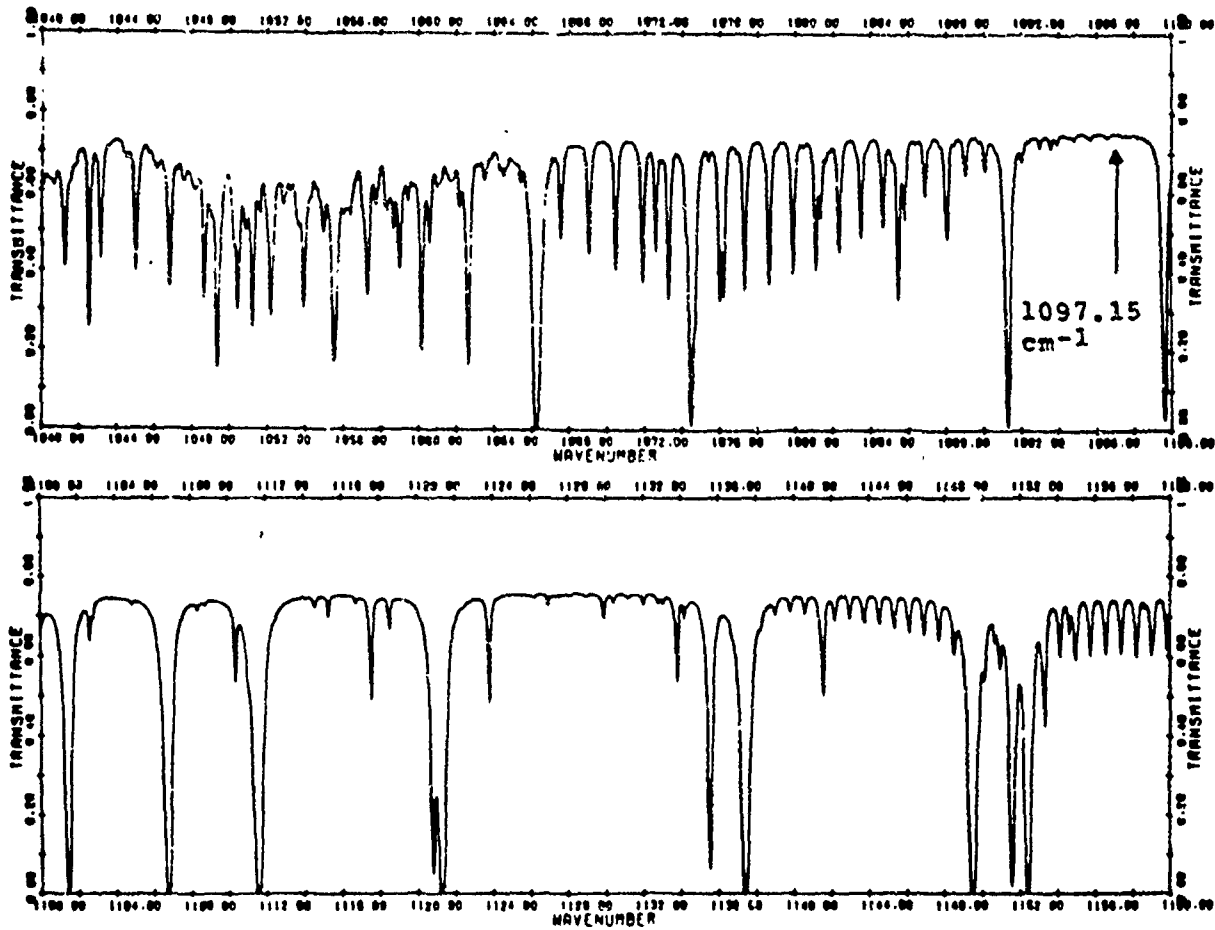


Figure 1-1. Atmospheric Transmittance Due to Molecular Absorption Through a 10-km Horizontal Path at Sea Level.

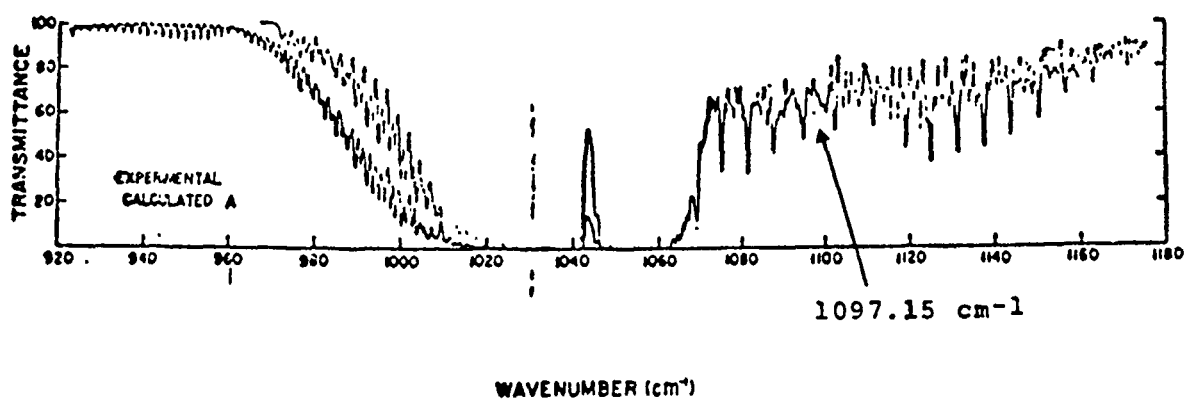


Figure 1-2. Ozone Absorption Spectrum in the CO₂ Laser Wavelength Region at 30-km Altitude. Data taken using a balloon-borne spectrograph.

a function of the azimuth of the transmitted beam relative to the orbital plane. Absorption profiles for three CO_2 lines (including the one of interest), propagating through various model atmospheres at a 62° nadir angle and a 15° azimuth relative to the orbital plane, are shown in Figure 1-3.

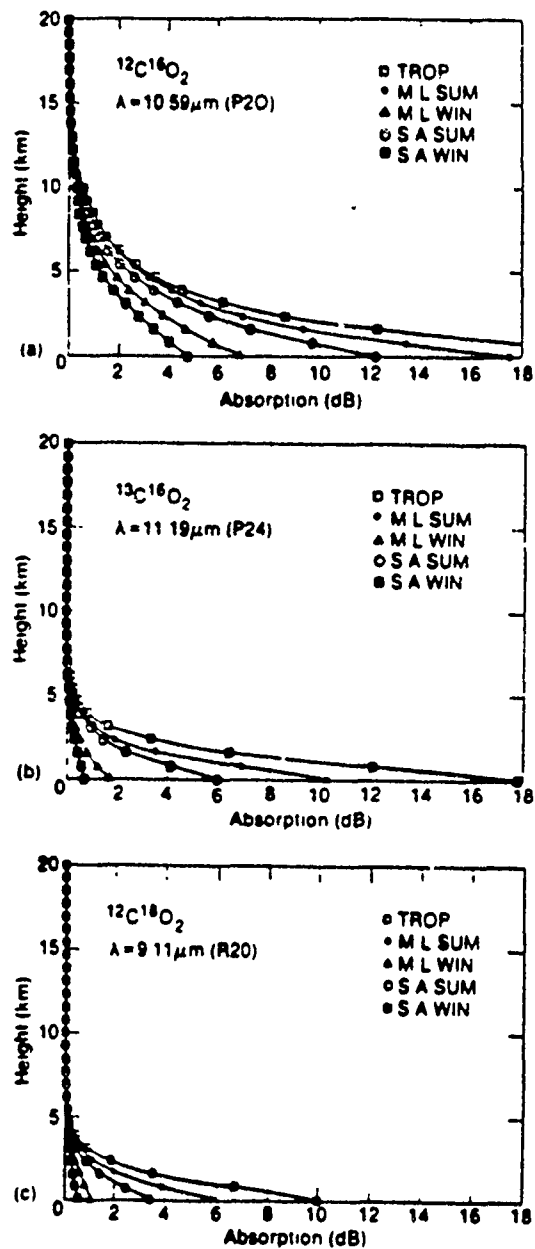


Figure 4-3. Two-way Absorption Profiles for Three CO_2 Laser Lines Propagating Through Various Model Atmospheres at 62° Nadir Angle, 15° Azimuth.

Section 2

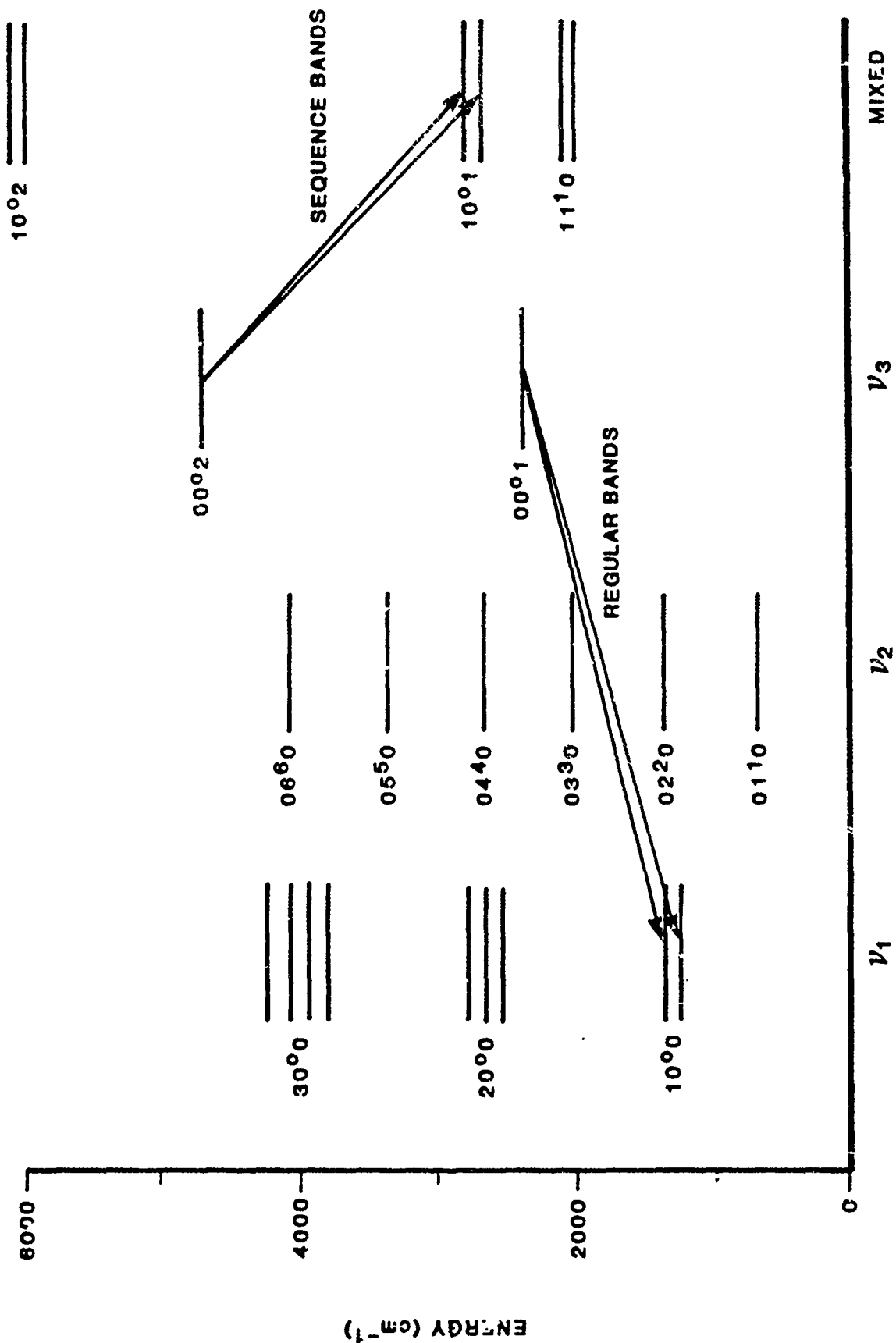
LASER KINETIC MODEL

2.1 INTRODUCTION

Over the past fifteen years, STI has developed a comprehensive CO_2 kinetics model that can be used to compare with experiments and to predict the performance of new lasers. This model has been proven by comparing its predictions with the performance of several discharge excited CO_2 lasers. The model has been updated whenever new information became available or whenever serious disagreement with experiments was identified. This model is a valuable tool for predicting the performance of new lasers because a large and fairly complete body of work has been reported in the literature for 626 CO_2 (this shorthand notation lists the last digit in the atomic weight of each atom in the CO_2 molecule, e.g., 626 refers to $^{16}\text{O}^{12}\text{C}^{16}\text{O}$). Much less information is available for the 828 CO_2 isotope. However, during this program, the measured results for 828 CO_2 have been compared with those for 626 CO_2 under the same excitation conditions, and the information obtained used to incorporate the specifics of 828 CO_2 into the model. The assumption has been made that 626 and 828 CO_2 isotopes behave similarly except for a few specific processes that may be sensitive to the details of the isotopic energy level spacing and transition probabilities. Using these assumptions and the experimental results, a model has been developed which can be used to design and predict the performance of $^{12}\text{C}^{18}\text{O}_2$ active molecule high pressure pulsed lasers.

2.2 CO_2 ENERGY LEVEL STRUCTURE

Figure 2-1 presents an energy level diagram showing the lowest vibrational levels for 626 CO_2 . The normal modes are labeled as follows: ν_1 is the symmetric stretch, ν_2 is the bending mode and ν_3 is the asymmetric stretch. The mixed mode column shows levels that have two or more normal modes excited; thus, the level 10^01 , which is the lower level for the sequence bands, has one quantum of symmetric stretch and one



87 15527

Figure 2-1. CO₂ Vibrational Energy Levels and Transitions

quantum of asymmetric stretch excited. The levels within each mode are grouped according to the convention of Rothman, et al., used in the AFGL tables.⁽³⁾ Therefore, the 10^0_0 and 02^0_0 unperturbed levels, which are mixed by Fermi resonance, are shown as both belonging to the symmetric stretch mode, and the unperturbed levels 11^1_0 and 03^1_0 are both shown as the mixed 11^1_0 levels. The normal 9 and $10\text{-}\mu\text{m}$ laser transitions are shown as transitions between the 00^0_1 level and the 10^0_0 Fermi couplets. The sequence band 9 and $10\text{-}\mu\text{m}$ laser transitions originate from the 00^0_2 second excited level of the asymmetric stretch mode, and end on the 10^0_1 mixed mode Fermi couplet.

2.3 CO_2 KINETICS/DISCHARGE MODEL

The CO_2 kinetics/discharge model is a two-part computer model and is presented schematically in Figures 2-2 and 2-3. The first part is a computer program that utilizes the electrical excitation cross sections for He, N_2 and CO_2 to solve the Boltzmann equation for the electron distribution function versus E/N . The cross sections used are taken from the JILA compilation by Kieffer.⁽⁴⁾ The electron excitation cross-sections are then integrated over the electron energy distribution functions to give the distribution of pump energy among the excitation channels as a function of E/N . The excitation rates as a function of E/N are then placed in a look-up table to be used as input to the kinetics model.

Figure 2-4 shows the results of the Boltzmann code calculations for the fraction of the discharge power going into the N_2 and CO_2 vibrational modes as a function of E/N for a $\text{He}/\text{N}_2/\text{CO}_2 = 3/2/1$ gas mixture. The optimum E/N can be estimated by finding the value that maximizes power into the sum of the N_2 and CO_2 (ν_3) curves. From this figure, it can be seen that the optimum E/N for $3/2/1$ mix is about $2 \times 10^{-16} \text{ V-cm}^2$. The Boltzmann code also calculates the fraction of the power that goes into electronic excitation and ionization, but these terms are not used in the kinetics code; the fractional power into electronic excitation and ionization can be estimated from Figure 2-4 by subtracting the sum of the other three curves from the numerical value one.

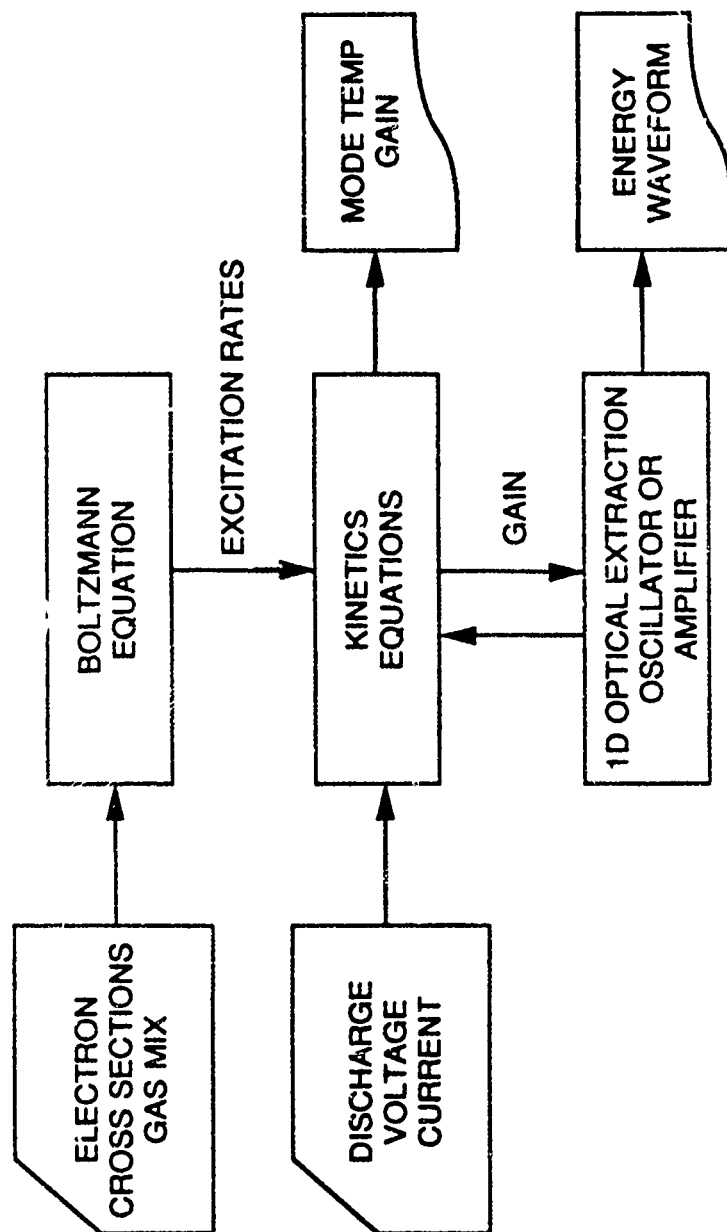


Figure 2-2. STI CO₂ Kinetics Model

89 17561

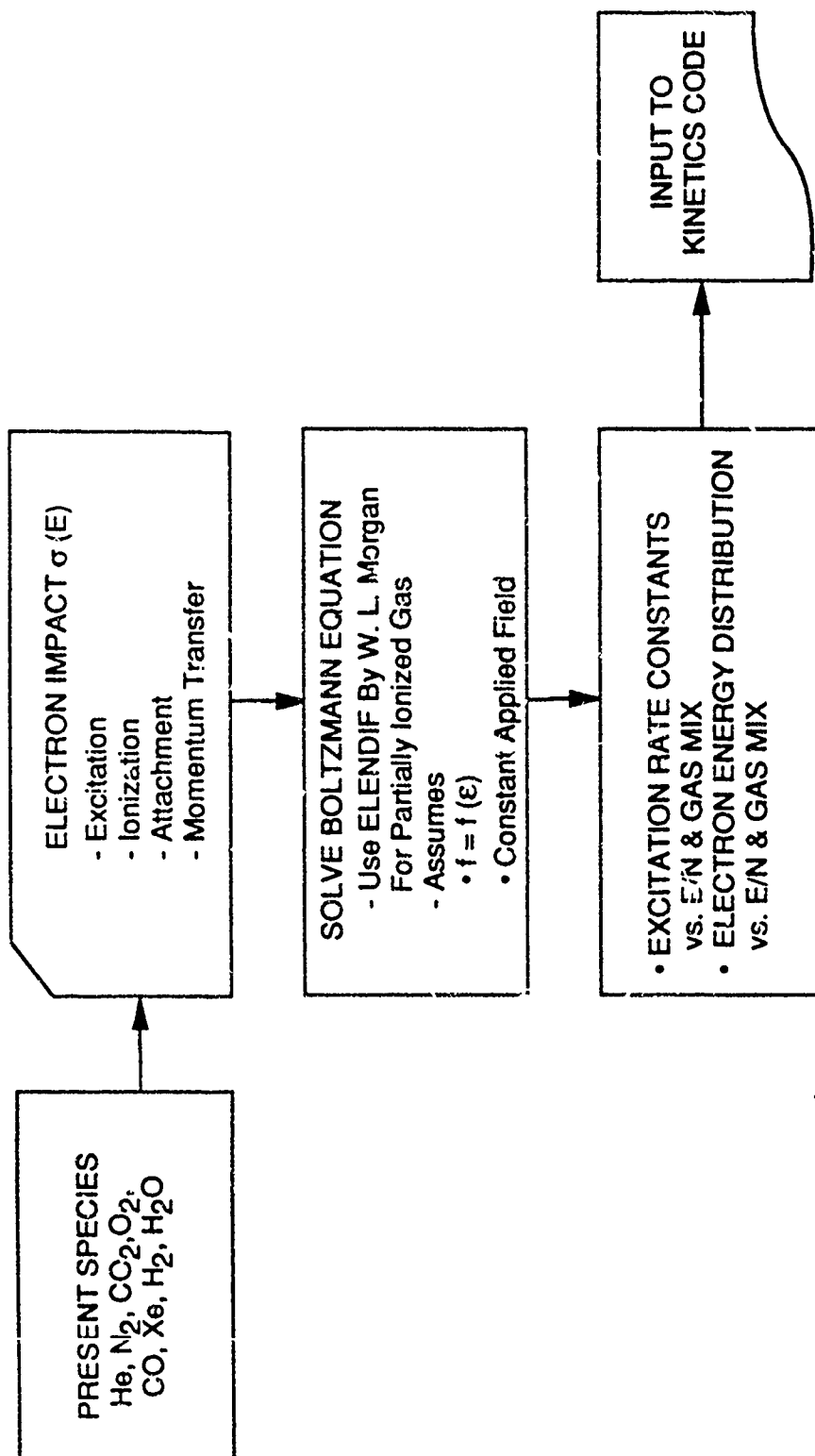
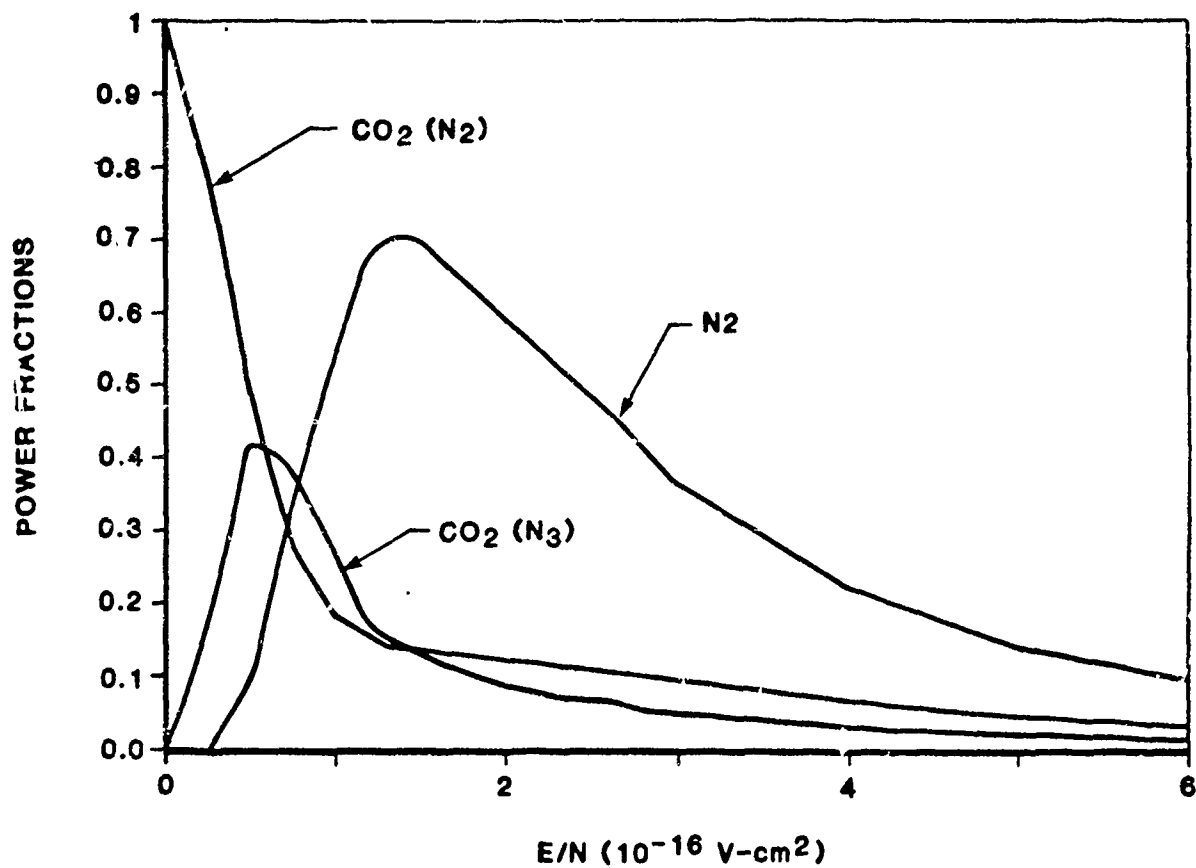


Figure 2-3. Boltzmann Solver Features

89 17562



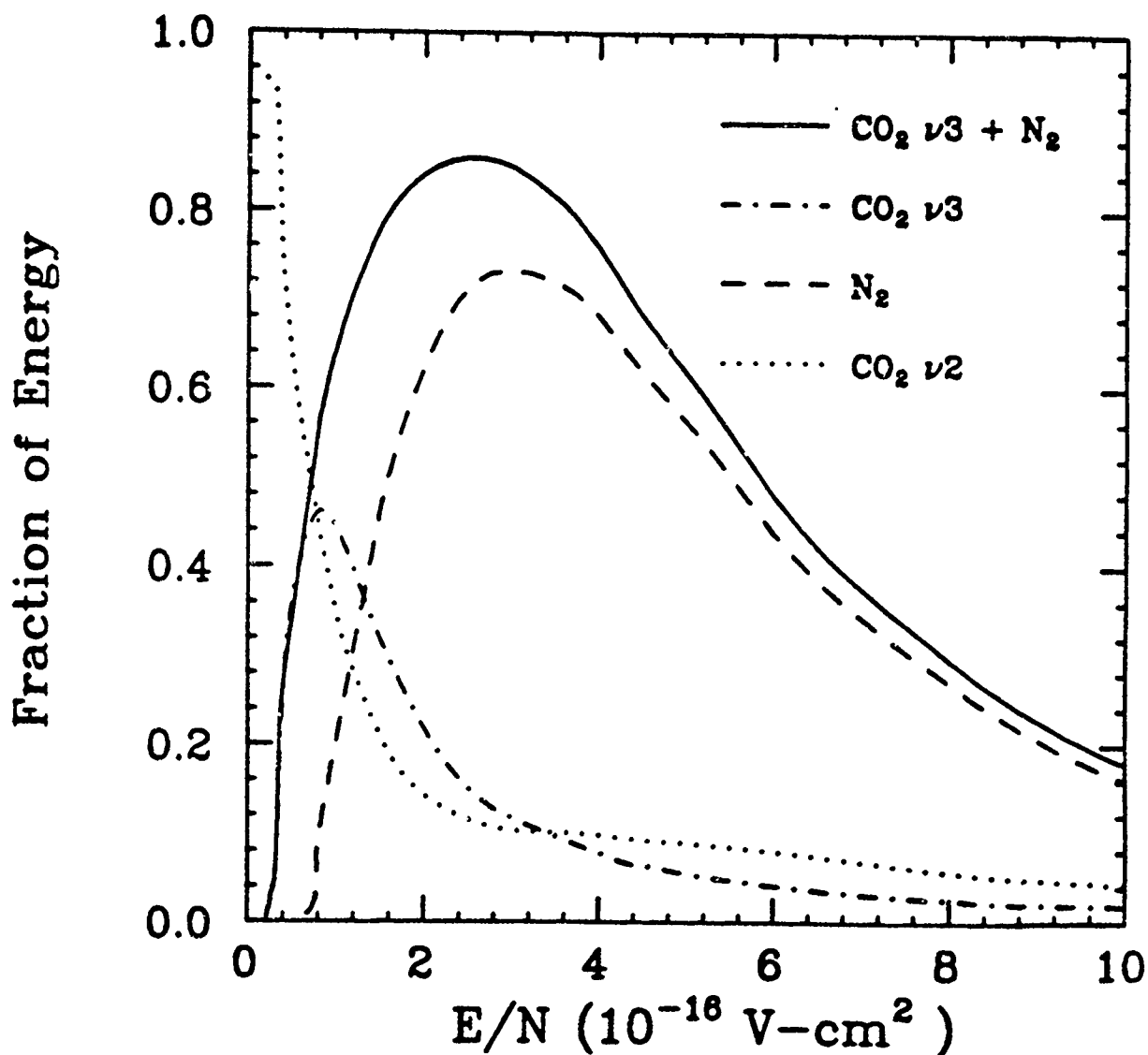
87 15027

Figure 2-4. Discharge Power into Vibrational Modes for $\text{He}/\text{N}_2/\text{CO}_2 = 3/2/1$ as a Function of E/N

Figure 2-5 shows the Boltzmann code predictions for the fractional discharge power going into excitation of the N_2 and CO_2 vibrational modes as a function of E/N for a $He/N_2/CO_2 = 45/40/15$ gas mix. This gas mix showed very good efficiency and energy loading characteristics in the Lucy self-sustained discharge experiments. The optimum pumping efficiency from the curves in Figure 2-5 occurs for E/N values from $2-3 \times 10^{-16} \text{ V-cm}^2$.

Figure 2-6 compares the total fractional power into the sum of $N_2 + CO_2(\nu_3)$ vibrational modes for the $He/N_2/CO_2 = 45/40/15$ gas mix with the more standard $He/N_2/CO_2 = 8/1/1$ gas mix used in self-sustained discharge CO_2 lasers. Also indicated in the figures is the self-sustaining E/N for each of these mixtures. For e-beam sustained discharges, the E/N can be adjusted to give the optimum excitation efficiency for the mixture. However, the self-sustaining E/N is fixed at the value at which the total ionization rate equals the total attachment rate for the mixture. These curves show that the self-sustained discharge excitation efficiency for the $He/N_2/CO_2 = 45/40/15$ mix is much higher than for the $He/N_2/CO_2 = 8/1/1$ mix. In addition, because of the higher N_2 and CO_2 content, the lower He gas mix can have much higher volumetric energy loading before the discharge becomes unstable or the gas temperature becomes high enough to kill the gain.

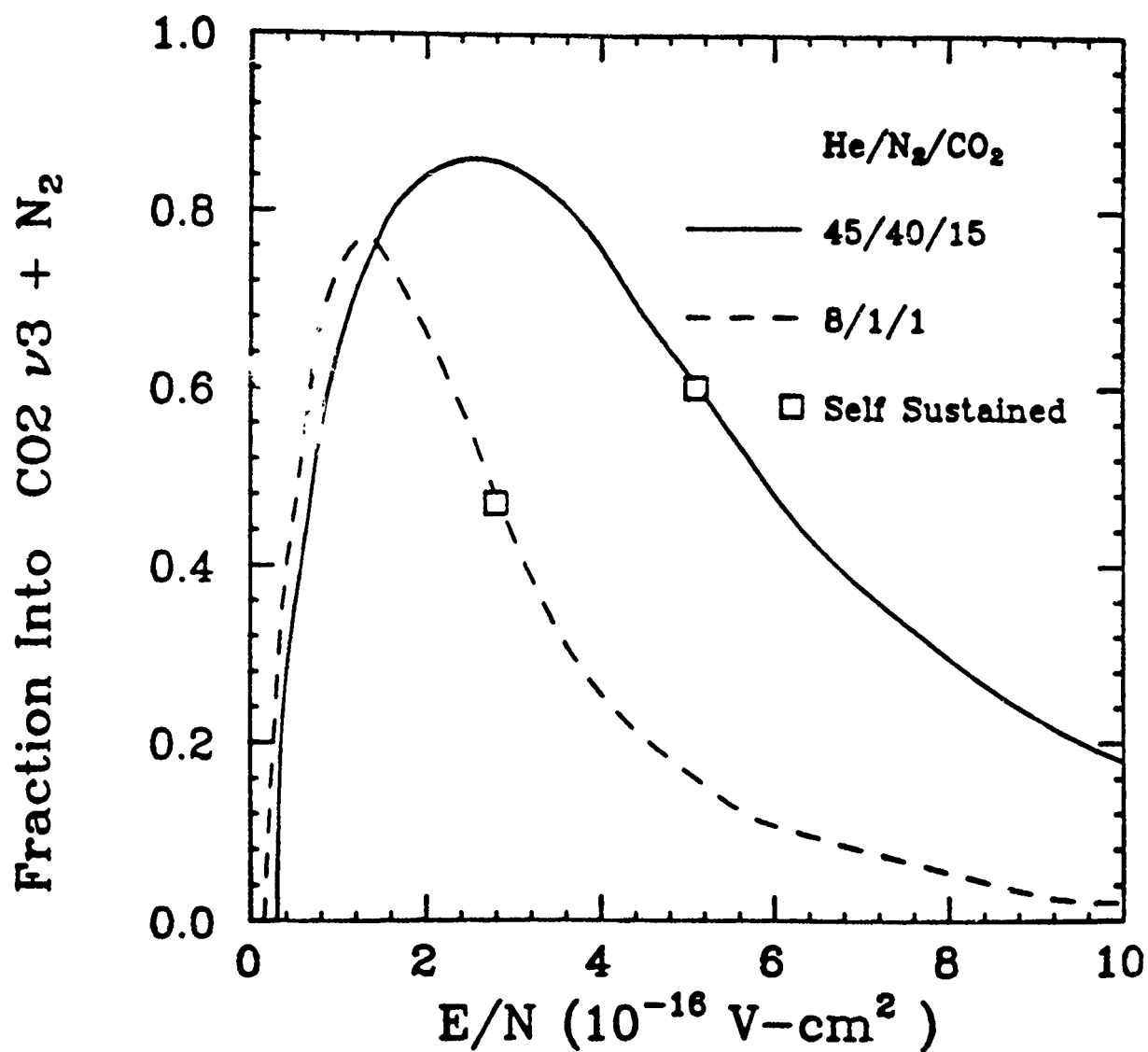
The kinetics model is a five-temperature model that uses input voltage and current pulses plus the excitation rates from the Boltzmann solver to calculate the five temperatures as a function of time. The five temperatures are the translational temperature, the N_2 vibrational temperature, the CO_2 symmetric and asymmetric stretch mode vibrational temperatures, and the CO_2 bending mode temperature. The model assumes full equilibration within each mode and also that the translational and rotational temperatures are in equilibrium. The kinetics model includes the rates for intermode vibrational transfer and for vibration-translation relaxation so that the mode temperatures can be calculated as a function of time. The rate constants, used along with their corresponding temperature dependence, have been obtained from the comprehensive review paper by Taylor and Bitterman.⁽⁵⁾ The small signal gain is calculated as a function



DISCHARGE ENERGY DISTRIBUTION

$$\text{He}/\text{N}_2/\text{CO}_2 = 45/40/15$$

Figure 2-5. Discharge Energy into Vibrational Modes as a Function of E/N for the Gas Mix Used in the Lucy and Delilah Experiments



DISCHARGE ENERGY DEPOSITION

Figure 2-6. Fraction of Energy into the Sum of N₂ and CO₂(ν_3) Vibrational Modes for Two Gas Mixes Studied in the Experiments

of time by evaluating the appropriate Boltzmann factors for the vibrational and rotational populations for the upper and lower laser levels and subtracting them to determine the population difference. The optical cross sections used for 626 CO_2 were the same as those reported in AVCO data.⁽⁶⁾

For use with 828 CO_2 , the model has been modified to incorporate the smaller energy level spacings for the 828 CO_2 isotope. For lack of information, it has been assumed that the electrical excitation fractions are the same as for 626 CO_2 . This is a good assumption since the small differences in energy levels are too small to significantly affect the excitation cross sections. The vibrational-relaxation rate constants for the upper laser level have been modified to incorporate the experimental data obtained in the Lucy experiments. However, the other intermode vibrational-transfer rates and the temperature dependence of the rate constants have been assumed to be the same as for 626 CO_2 because of the lack of any measurements. These assumptions may not be justified; however, for the conditions of the measurements in this program, the sensitivity to any differences that may show in these other rate constants is not large.

Optical transition moment data for 828 CO_2 was obtained by multiplying the radiative lifetime for 626 CO_2 by the constant factor that gave best agreement with the small signal gain measurements to be described in Section 3. This factor was most sensitive to the peak small signal gain and was not affected much by small changes in the decay time constants.

Optical transition dipole moment data for 626 CO_2 is summarized in Table 2-1, along with the data from the present experiments for 828 CO_2 . For 828 CO_2 , the shorter wavelength $00^0_1 \rightarrow 02^0_0$ band at 9.2 μm has almost twice the transition moment of the longer wavelength $00^0_1 \rightarrow 10^0_0$ band at 10.3 μm . The higher transition moment results in higher small signal gain for the 828 CO_2 $00^0_1 \rightarrow 02^0_0$ transition at 9.11 μm than for the 626 CO_2 $00^0_1 \rightarrow 10^0_0$ transition at 10.6 μm for identical pumping conditions.

Table 2-1
CO₂ TRANSITION DIPOLE MOMENT DATA

SOURCE	$ R_u ^2 (00^0_1 \rightarrow 10^0_0)$ (10 ⁻³ DEBYE ²)		$ R_u ^2 (00^0_1 \rightarrow 02^0_0)$ (10 ⁻³ DEBYE ²)	
	626 CO ₂	636 CO ₂	828 CO ₂	828 CO ₂
AFGL	1.57	2.25		
Compilation ⁽⁴⁾				
Brimacombe & Reid ⁽⁷⁾	1.38			
Abubakar & Shaw ⁽⁸⁾	1.45	1.62		
Klaus Siensen ⁽⁹⁾	1.38	1.73		
AVCO ⁽⁶⁾	1.36			
STI Model	1.36	1.96	0.96	1.73

2.4 CO₂ OSCILLATOR/AMPLIFIER MODEL

The optical extraction portion of the CO₂ kinetics code is a one-dimensional model that assumes uniform extraction over the full aperture and can model either an oscillator or an amplifier configuration. The oscillator model treats the buildup from an initial intensity, which can be either background fluorescence or an injected signal. The model accommodates mirror separations that are longer than the active length, and losses which are lumped in with the mirror reflectivities. This optical model is fully coupled with the kinetics model so that the effect of the energy extraction is fed back into the kinetics model and is used to update the gain and mode temperatures.

The amplifier model includes a one dimensional optical extraction code. The amplified output flux Φ_{out} is calculated as

$$\phi_{out} = \phi_{in} \exp (\langle g \rangle L)$$

where ϕ_{in} is the time-dependent input flux to the amplifier and $\langle g \rangle$ is the average gain for the amplifier of length L. The use of an average gain for the entire amplifier may not intuitively seem like a good assumption. However, calculations at STI, which divided the amplifier into five equal sections lengthwise and at AVCO for twenty segments,⁽⁶⁾ gave identical results to the one segment approximation. The model accommodates a time-dependent input intensity and self consistently saturates the small-signal gain as a function of time. This program allows prediction of the power gains or energy extraction for any proposed amplifier design and input pulse shape. These predictions can be correlated with experimental measurements of power gains to evaluate the extraction characteristics of the amplifier for both 626 and 828 CO₂ isotopes.

Section 3

LASER KINETICS MEASUREMENTS

3.1 INTRODUCTION

The purpose of the work described in this section is to investigate collisional quenching of the upper laser level of $C^{18}O_2$ in a high pressure, pulsed laser and provide a set of quenching rate constants that can be used in modeling the gain and output characteristics of $C^{18}O_2$ laser systems. The collision partners for which quenching rate constants were measured are He, N_2 and $C^{18}O_2$, the normal constituents of a CO_2 laser gas mixture. The quenching rate constants were determined by using a transient gain technique in which the gain medium is provided by a high pressure He/ N_2 / $C^{18}O_2$ discharge. Since the excited CO_2 is generated by the discharge, the rate constants that are reported here pertain to operation of a pulsed CO_2 laser. Non-equilibrium conditions, especially in the vibrational degrees of freedom, may exist in such high pressure discharges, so that the rate constants may not correspond to the room temperature values. The $C^{18}O_2$ rate constants that we measure here are compiled with similar rate constants for $^{13}CO_2$ that were measured with the same apparatus in an earlier study, and the room temperature values of the rate constants for normal CO_2 . In addition to the quenching rate constants, we describe small signal gain measurements for specific gas mixtures and energy loadings in He/ N_2 / CO_2 discharges. The small signal gains are measured on both CO_2 lasing bands. The small signal gains were compared directly with similar gains for normal CO_2 so that estimates of the transition strengths can be made.

3.2 EXPERIMENTAL

3.2.1 Lucy Discharge Laser

A schematic diagram of the Lucy x-ray preionized self-sustained discharge laser is shown in Figure 3-1 and a photograph is shown in Figure 3-2. The Lucy discharge region consists of two aluminum electrodes contained in a glass tube. To minimize isotopic exchange with rare CO_2 isotopes, the other materials are limited to stainless steel for the window flange assemblies, NaCl windows and viton o-rings. To allow operation at 1 atm, the electrode profiles were designed using the ELF and PANDIRA field-analysis codes, modified with a flat region at the center. The resulting profile gives a well-defined discharge of width 3.6 cm between the electrodes spaced 4-cm apart. The length of the active region is 90 cm, giving an active volume of 1.3 liters. The total volume of the chamber is about 20 liters.

The x-ray source is a converted cold cathode e-beam with a Ta foil placed between the hibachi and 3-mil Al foil to convert the high-voltage electrons to x-rays. The e-beam operating voltage was approximately 230-kV and the electron current at the foil was of the order of $3\text{-}5\text{ A/cm}^2$. The x-rays are collimated by lead apertures placed between the source and the laser tube. Preionization electron densities of approximately 10^8 electrons/ cm^3 have been previously measured on this device. The x-ray gun is typically triggered 500 ns before the PFN and crowbarred immediately after the PFN is triggered. The pulse forming network for the gain cell is a ten-section pulse forming network that delivers 38 J of energy to the discharge in a 10- μs pulse. The circuit is shown schematically in Figure 3-1 and typical operating parameters are summarized in Table 3-1. Typical discharge voltage and current traces are shown in Figure 3-3. The voltage spike at the beginning of the pulse avalanches the electron density from the initial value of 10^8 electrons/ cm^3 to the final value of 10^{12} electrons/ cm^3 . After the gas is broken down, the PFN delivers its energy in an approximately square 10- μsec pulse. A small mismatch between the discharge PFN impedance results in a small afterpulse ($\leq 10\%$ of the main pulse). In all of our measurements, the current and voltage at the cathode of the gain cell are recorded for each pulse in order to determine the energy loading.

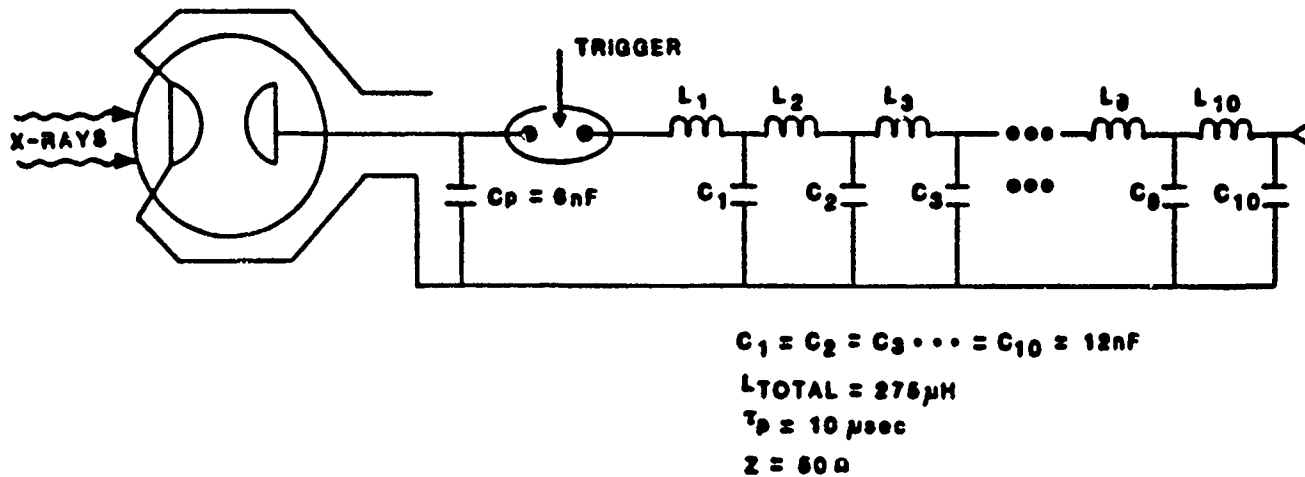


Figure 3-1. Schematic Diagram of Lucy X-Ray Preionized Discharge Amplifier

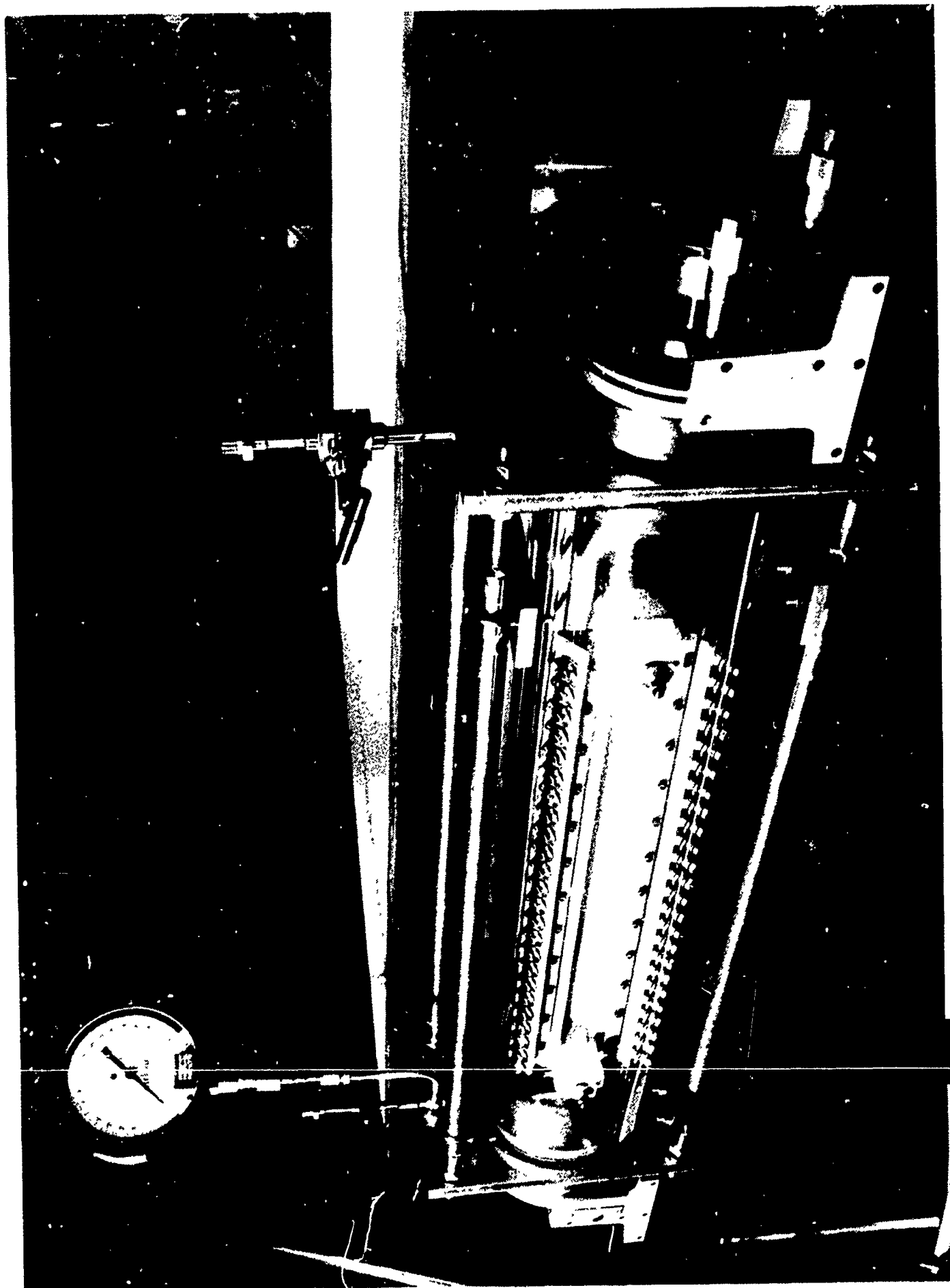


Figure 3-2. Lucy Glass Tube Upgrade

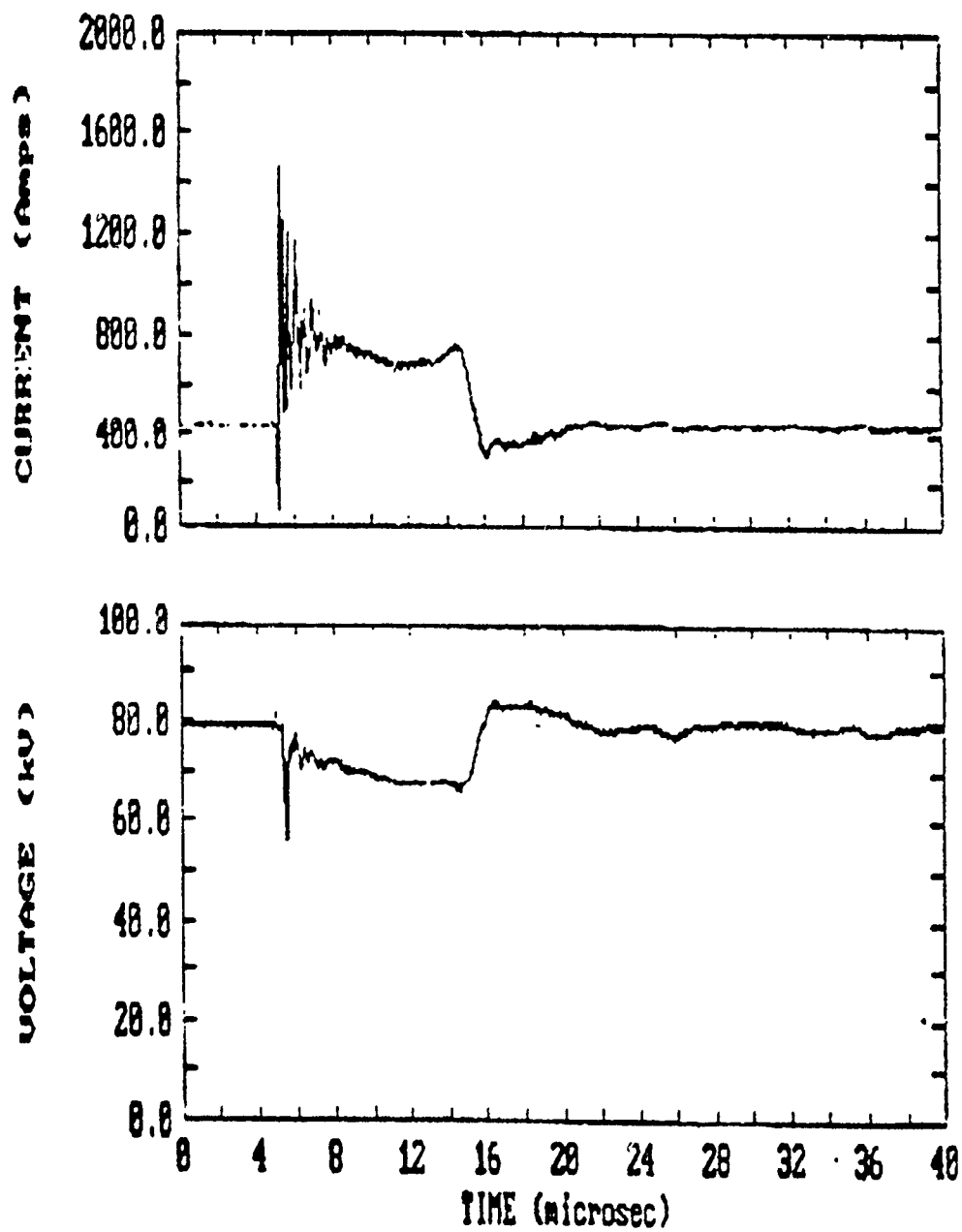


Figure 3-3. Typical Voltage and Current Traces for the Discharge of Glass Lucy

Table 3-1

OPERATING PARAMETERS FOR LUCY X-RAY
PREIONIZED DISCHARGE LASER

Parameter	Glass LUCY
Aperture (cm)	4 x 3.5
Length (cm)	90
Gas Mixture (He/N ₂ /CO ₂)	13/2/1
Pressure (atm)	0.5
Pump Pulse Duration (μsec)	10
Discharge E/N (V-cm ²)	2.3 x 10 ⁻¹⁶
Discharge Current (A/cm ²)	0.8
Pump Power (kW/cm ³ -atm)	5.0
Energy Loading (J/l-atm)	50

3.2.2 Gain Diagnostics

Figure 3-4 shows the experimental setup for the deactivation and gain measurements. A cw C¹⁸O₂ laser capable of delivering 5 W on a single line is used as the probe laser. The probe beam is expanded and collimated to give a nominal 1/e² diameter of 0.5 cm as it passes through the gain cell. The probe beam is attenuated with a germanium flat so that the power entering the gain cell is 400 mW, nominally. Upon exiting the gain cell, the amplified probe signal is detected with either a Ge:As detector or a HgCdTe detector. The characteristics of these detectors differ considerably. The Ge:As detector has a very linear response at 9 μm over a 0 to 3-W range of direct incident power on the detector. On the other hand, the HgCdTe detector begins to saturate with as little as 0.5 mW of direct power. The Ge:As detector was used in all of the measurements of deactivation rates because of the linearity. The response time of the Ge:As detector is approximately 1 μs while that of the HgCdTe detector is approximately 10 ns. Even though the response time of the Ge:As detector is significantly longer, this was not a problem since the measured decay

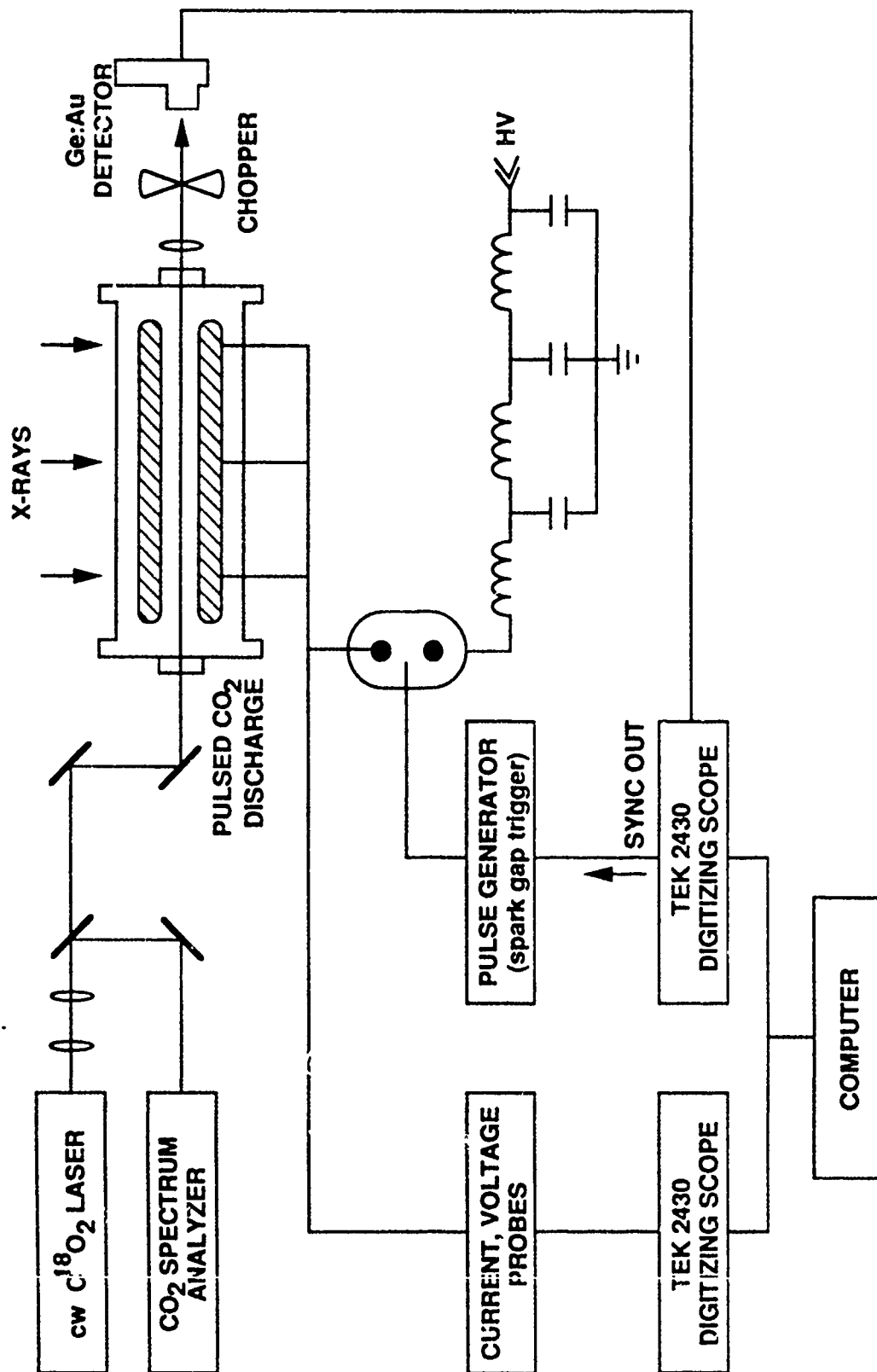


Figure 3-4. Experimental Setup for the Deactivation and Gain Measurement

89 17973

times were typically 100 μ s or greater. The HgCdTe detector was used for all of the small signal gain measurements, since the Ge:As detector has poor sensitivity for the weaker 828 ($10^0_0 - 00^0_1$) band. The beam exiting the gain cell was attenuated sufficiently to keep the response of the detector nearly linear. Linearity was checked by measuring the small signal gain at different power levels of the probe laser. The probe power was varied over a 100 to 400-mW range.

The signal from the detector as well as the current and voltage traces from the gain cell were acquired with two digitizing oscilloscopes and transferred to a computer for further analysis. The unamplified probe signal was measured by chopping the cw probe beam between the gain cell and the detector. The probe beam was focused onto the chopper to shorten the rise and fall times of the chopped waveform. In the gain measurement, a 7% duty cycle was used with the chopper being open for 700 μ s. The discharge was delayed by 300 to 400 μ s after the rising edge of the chopped signal to eliminate a small overshoot in probe laser signal immediately following the rising edge of the chopper window. The overshoot appears to be a function of how the chopper is oriented in the focal region of the probe beam. The overshoot is less than 5% of the probe signal amplitude. However, this is still large enough to cause an underestimation of the small signal gain, especially at longer times when the population in the upper laser level is small. Effects of the overshoot are avoided by determining the amplitude of the probe signal from that part of the trace that lies within 150 μ s of the gain pulse.

In all measurements, the gain cell was operated with total pressures of 200 - 400 Torr. The gas mixtures were prepared by adding the gases sequentially to the gain cell. The order of addition was CO_2 , N_2 and He so that the gases were well mixed. The purities of the C^{18}O_2 , N_2 and He gases were 99.8% (isotopic purity), 99.998% and 99.995%, respectively. The gases were used without further purification. Isotopic exchange inside the gain cell was prevented by reducing the surfaces with atomic hydrogen and then exposing the surfaces to $^{18}\text{O}_2$ before C^{18}O_2 was used. Atomic hydrogen was generated by running discharges in a 250/50/16 Torr He/ N_2 / H_2 mixture. The reduction was essentially complete after 40 discharges. The laser was then

exposed to five 250/50 Torr He/ $^{18}\text{O}_2$ mixtures. The exposure time was 20 minutes per mixture. This procedure proved very effective at preparing the surfaces for ^{18}O . A gas mixture consisting of 230/50/20 Torr He/ $\text{N}_2/\text{C}^{18}\text{O}_2$ showed no sign of deteriorated gain after 40 discharges following this surface preparation procedure.

3.3 RESULTS AND DISCUSSION

3.3.1 Vibrational Deactivation

The rate constants for collisional deactivation of C^{18}O_2 (00^0_1) by He, N_2 and C^{18}O_2 were determined by measuring the gain decay of the CO_2 discharge as a function of the He, N_2 and CO_2 partial pressures. Here, the small signal gain, g_0 , on the ($00^0_1 - 02^0_0$) P(18) transition is used to monitor the 00^0_1 population. To a good approximation, g_0 scales directly with the 00^0_1 population, provided the population of the 02^0_0 level does not build up significantly during the decay. However, since this gain technique actually measures the decay of the $[00^0_1] - [02^0_0]$ population difference, bottlenecking (population buildup in the lower level) could cause the measured decay rates to exceed the decay time of the 00^0_1 level. It is highly unlikely that this occurs. Collisional quenching of ν_2 in 628 CO_2 , particularly by helium, is very rapid compared to quenching of the upper laser level. The rate constant for quenching the 02^0_0 level by helium is $1.1 \times 10^{-13} \text{ cm}^3 \text{ molec}^{-1} \text{ s}^{-1}$, which is two orders of magnitude higher than the rate constant for quenching of the 00^0_1 level by helium. Because ν_2 quenches so rapidly, bottlenecking generally does not occur with 628 CO_2 . In fact, one of the purposes of using helium as a buffer gas is to avoid bottlenecking. Most likely, helium quenches ν_2 very rapidly in 828 CO_2 as well.

In our measurements, the smallest amount of helium used in any of the 828 mixtures is 150 Torr. If it is assumed that the 628 and 828 quenching rates are the same, the ν_2 quenching rate on the order of $5 \times 10^5 \text{ s}^{-1}$ in these mixtures. This is one to two orders of magnitude higher than our fastest measured decay rate, which suggests that bottlenecking does not affect the measured decays to any significant extent. As a check for

bottlenecking, gain decays were measured for a 230/50/20 torr mixture of He/N₂/CO₂ using the P(18) line of the 00⁰1 - 02⁰0 band and the P(18) of the 00⁰1 - 10⁰0 band. If bottlenecking is significant, the [00⁰1]-[10⁰0] and [00⁰1]-[02⁰0] population differences may evolve differently, due to different quenching rates for the 10⁰0 and 02⁰0 levels. The measured gain decay rates for the I and II band transitions were 12800 s⁻¹ and 12800 s⁻¹, respectively, which suggests that bottlenecking is not occurring or that the 10⁰0 and 02⁰0 levels decay together due to their strong coupling.

Collisional quenching of the 00⁰1 level is pseudo-first order, so that g_0 is expected to show a single exponential decay. Figure 3-5 shows a typical amplified probe signal trace for 828 CO₂ II P(18) transition. The initial probe signal I_0 is amplified during the CO₂ discharge pulse and then decays after the discharge pulse is over. The gain was calculated from $g_0 = \ln(I/I_0)$. Figure 3-6 shows the temporal dependence of $\ln(g_0)$ calculated for the same trace shown in Figure 3-5. The linearity of $\ln(g_0)$ vs t is characteristic of all of the gain traces. The part of the gain trace that was used to determine the decay rates is that which lies 30 μ s beyond the firing of the gain cell. This delay was used primarily to avoid any transient effects of the discharge such as residual pumping that may occur after the initial 10- μ s pulse. On each gain trace, the decay rate was extracted from a weighted fit of $\ln(g_0)$ vs t to a straight line, where the fit typically covers one decade of decay. The measured decay rates for each gas mixture are shown in Table 3-2. The rates are averaged over five shots for each mixture.

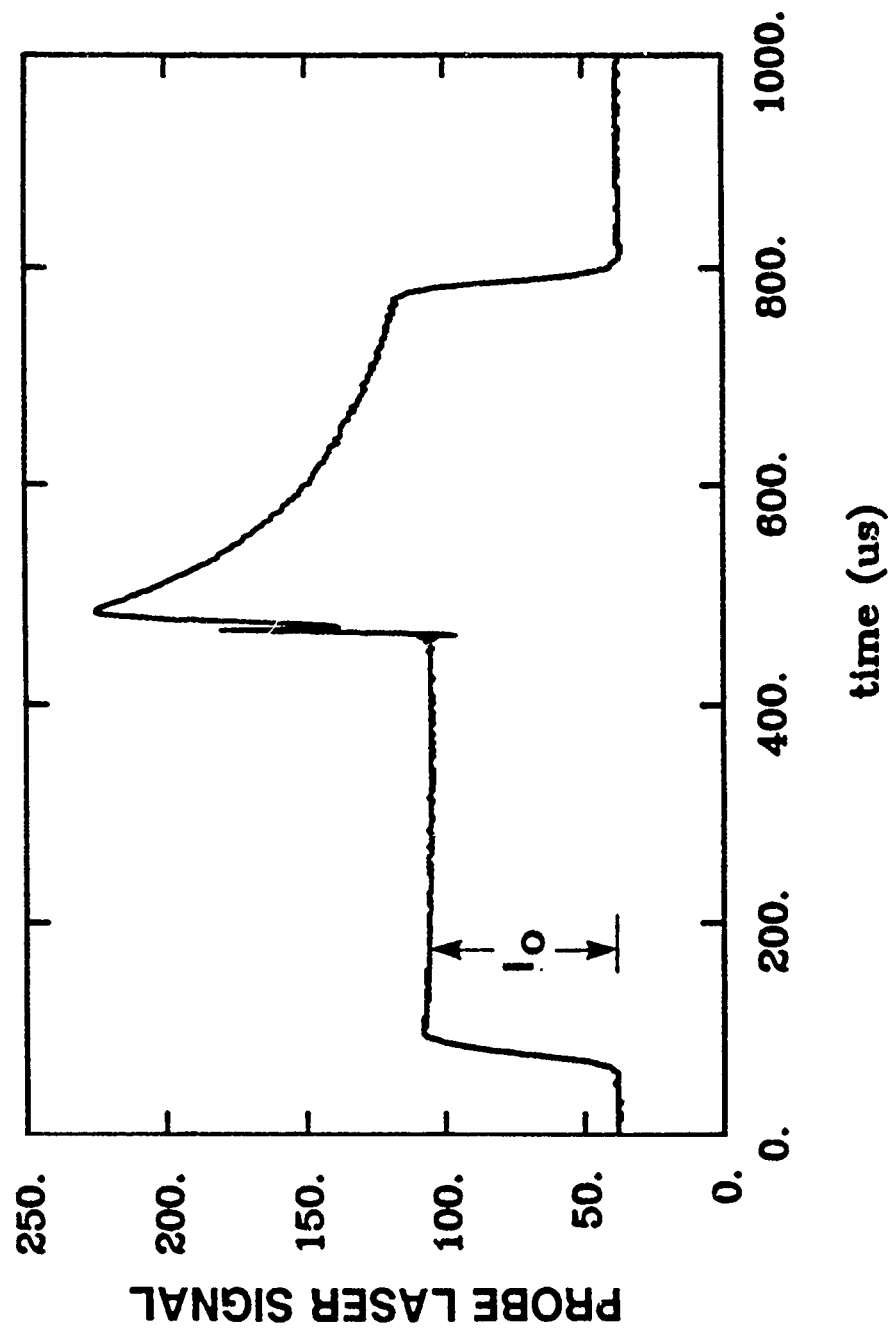


Figure 3-5. Typical Amplified Probe Signal for 828 CO_2 II P(18) Transition.
 $\text{He}/\text{N}_2/\text{CO}_2 = 250/50/10$ torr.

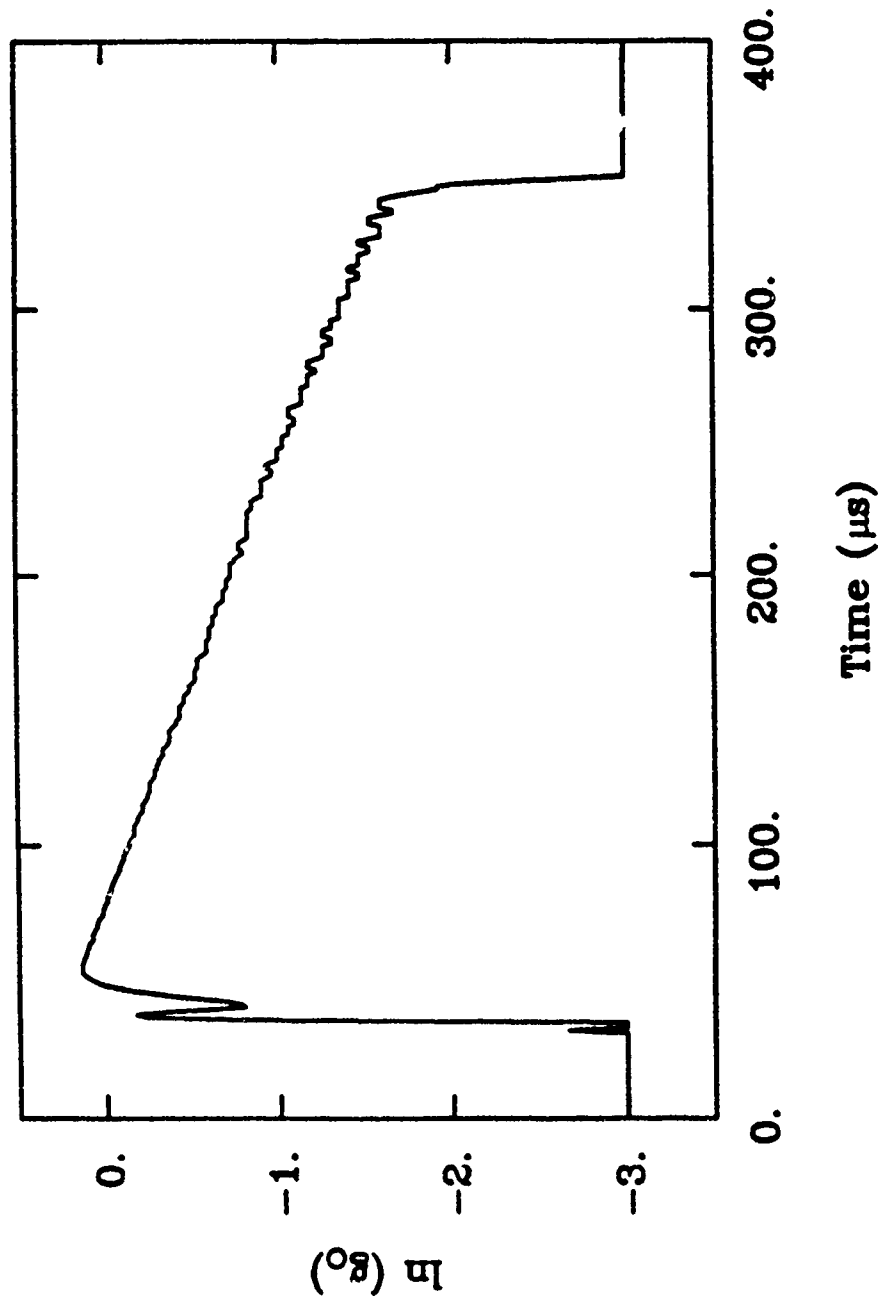


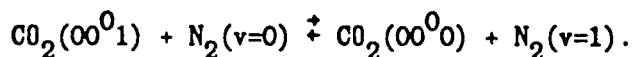
Figure 3-6. $\ln(g_0/g)$ vs t for 250/50/10 He/N₂/CO₂ Mix Calculated from the Trace of Figure 3-5.

Table 3-2

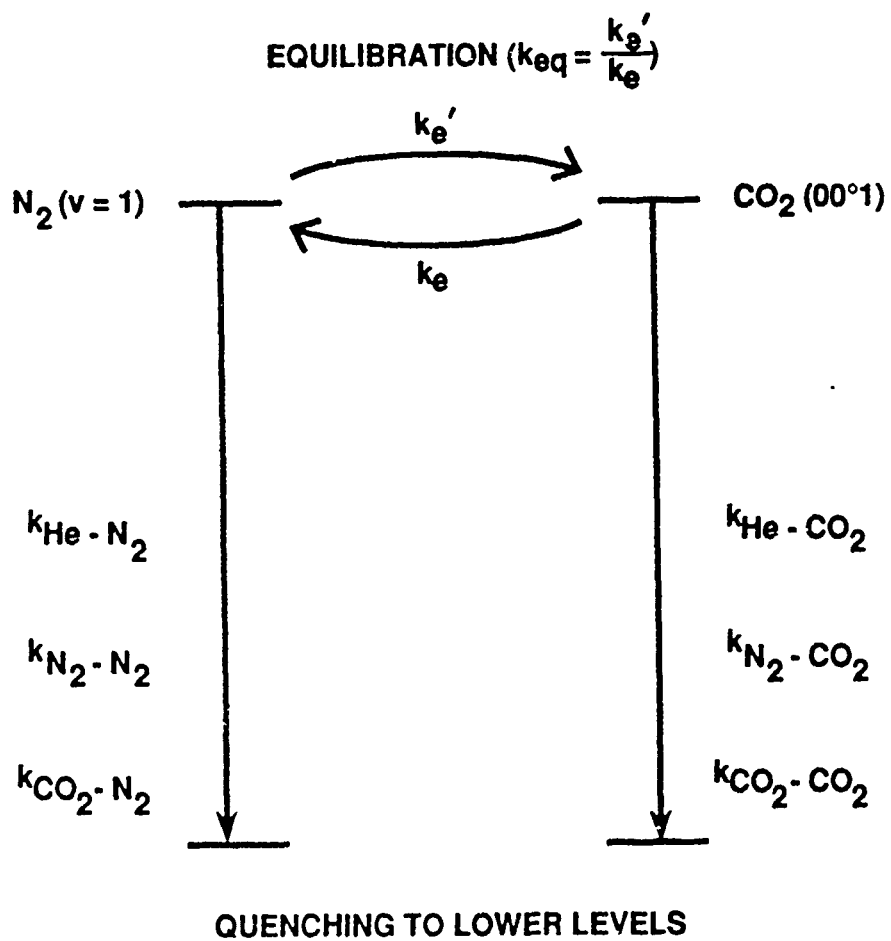
MEASURED DECAY RATES FOR He/N₂/CO₂ GAS MIXTURES

He/N ₂ /CO ₂ Pressures (torr)	Decay Rate (sec ⁻¹)
149.3/51.7/10.1	5294
252.4/51.7/10.1	6089
353.2/51.7/10.1	7130
453.9/51.7/10.1	8207
554.1/51.7/10.1	9352
231.1/51.0/19.9	12770
152.8/28.3/10.2	6572
152.8/75.4/10.2	5808
152.8/100.1/10.2	4708
152.8/125.4/10.2	4602
252.9/51.7/5.2	3293
249.1/50.6/10.1	6072
254.4/50.5/15/1	9349
251.3./50.2/20.0	12860
251.1/49.3/25.3	16670

The energy transfer processes that govern the decay of the CO₂(00⁰1) level are the rapid transfer between N₂(v=1) and CO₂(00⁰1), and collisional deactivation of CO₂(00⁰1) and N₂(v=1). These processes are depicted in Figure 3-7. The fastest process is certainly the near resonant energy exchange between N₂(v=1) and CO₂(00⁰1)



It is well known that any population in the CO₂(00⁰1) level equilibrates with N₂(v=1) on a time scale that is much shorter than collisional decay to the lower levels. Since N₂(v=1) and CO₂(00⁰1) are so strongly coupled, the decay times that are measured are for the combined N₂(v=1) + CO₂(00⁰1) populations. If it is assumed that the only processes that are important are the equilibration and the collisional quenching of CO₂(00⁰1) and N₂(v=1) to lower levels, the decay time is related to the quenching rate constants by the following expression.



89 17974

Figure 3-7. Schematic Diagram of Energy Transfer Processes for CO_2 Lasers.

$$\tau^{-1} = [\text{CO}_2] / ([\text{CO}_2] + K_{\text{eq}}[\text{N}_2]) \left\{ k_{\text{He-CO}_2}[\text{He}] + \left(k_{\text{N}_2\text{-CO}_2} + K_{\text{eq}}k_{\text{CO}_2\text{-N}_2} \right) [\text{N}_2] \right. \\ \left. + k_{\text{CO}_2\text{-CO}_2}[\text{CO}_2] + K_{\text{eq}}k_{\text{He-N}_2}[\text{He}][\text{N}_2]/[\text{CO}_2] + K_{\text{eq}}k_{\text{N}_2\text{-N}_2}[\text{N}_2]^2/[\text{CO}_2] \right\} \quad (3-1)$$

Here, the subscripts on the rate constants are such that the collision partner is identified first and the molecule being quenched second. The equilibrium constant pertains to the $\text{N}_2(v=1) - \text{CO}_2(00^01)$ energy exchange, and it has a value of 0.924 at 300 K for 828 CO_2 .

Of the terms shown in (3-1), only the first three contribute significantly to the decay rate. The last two terms, which pertain to quenching of $\text{N}_2(v=1)$ by He and N_2 , are at least two orders of magnitude smaller than any measured decay rate, $(([\text{CO}_2] + K_{\text{eq}}[\text{N}_2])/[\text{CO}_2])\tau^{-1}$, and so can be neglected. As such, the only rate constants considered here were $k_{\text{He-CO}_2}$, $k_{\text{CO}_2\text{-CO}_2}$ and $(k_{\text{N}_2\text{-CO}_2} + K_{\text{eq}}k_{\text{CO}_2\text{-N}_2})$. The rate constant for quenching by N_2 , $(k_{\text{N}_2\text{-CO}_2} + K_{\text{eq}}k_{\text{CO}_2\text{-N}_2})$, is a composite of quenching of $\text{CO}_2(00^01)$ by N_2 and quenching of $\text{N}_2(v=1)$ by CO_2 . The two components cannot be distinguished in these measurements. The quenching rate constants were extracted from an analysis in which the measured decay rates for the various He/ N_2 / CO_2 mixtures were fit to Eq. (3-1) using a standard matrix inversion procedure. The data base contains the decay rate measured on each gain shot, so that no averaging of decay rates was done prior to evaluating the rate constants. In addition to this fitting procedure, Stern-Volmer analyses of the decays were done for the He, N_2 and C^{18}O_2 collision partners. Stern-Volmer plots for all collision partners are shown in Figures 3-8, 3-9 and 3-10. The rate constants that result from both fitting procedures are shown in Table 3-3 along with a similar set of rate constants for $^{13}\text{CO}_2$ and the room temperature values of the rate constants for normal CO_2 .⁽⁶⁻⁹⁾ The agreement between the two fitting procedures is generally good. The differences in the rate constants obtained with the two procedures are probably more representative of the errors in the rate constants than the $\pm 1\text{-}2\%$ errors that result from either fitting method. The error in each rate constant is taken to be $\pm 20\%$ of the value.

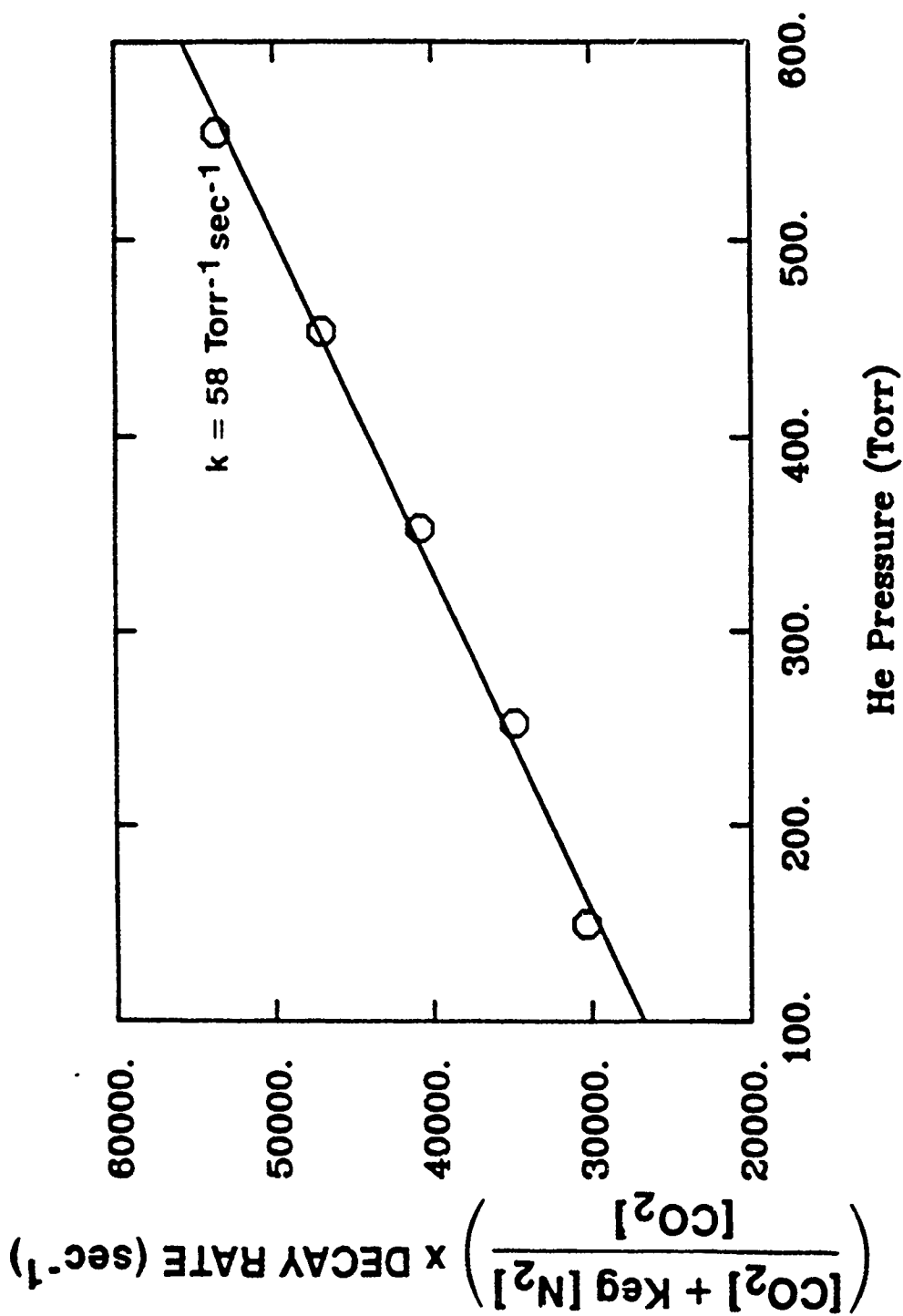


Figure 3-8. Collisional Decay Rate for C^{18}O_2 (00^0_1) Level as a Function of He Pressure. Each point is an average of five measured decays. $[\text{N}_2] = 52 \text{ torr}$ and $[\text{CO}_2] = 10 \text{ torr}$.

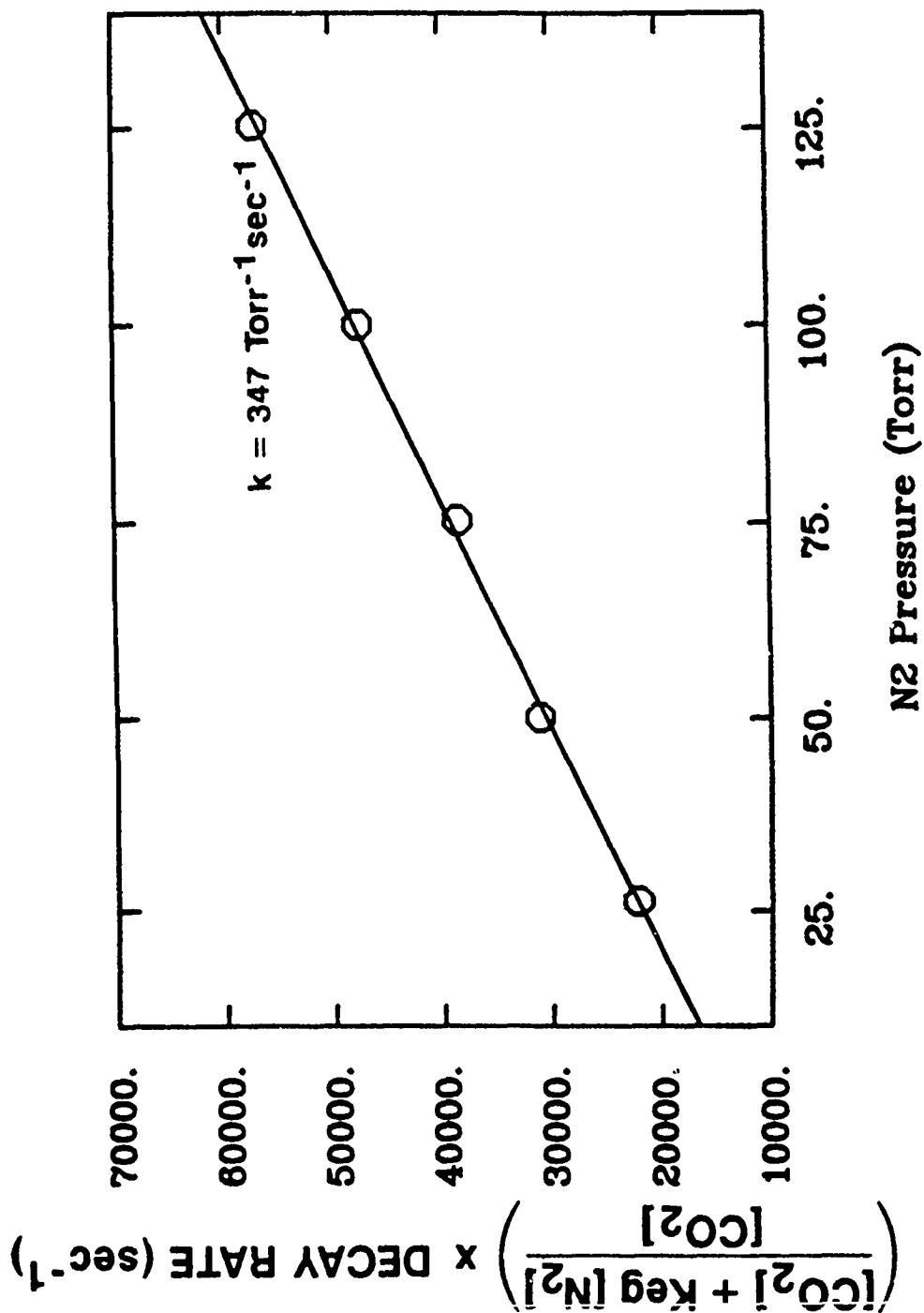


Figure 3-9. Collisional Decay Rate for $C^{18}O_2$ (001) Level as a Function of N_2 Pressure. Each point is an average of five measured decays. $[He] = 153 \text{ torr}$ and $[CO_2] = 10 \text{ torr}$.

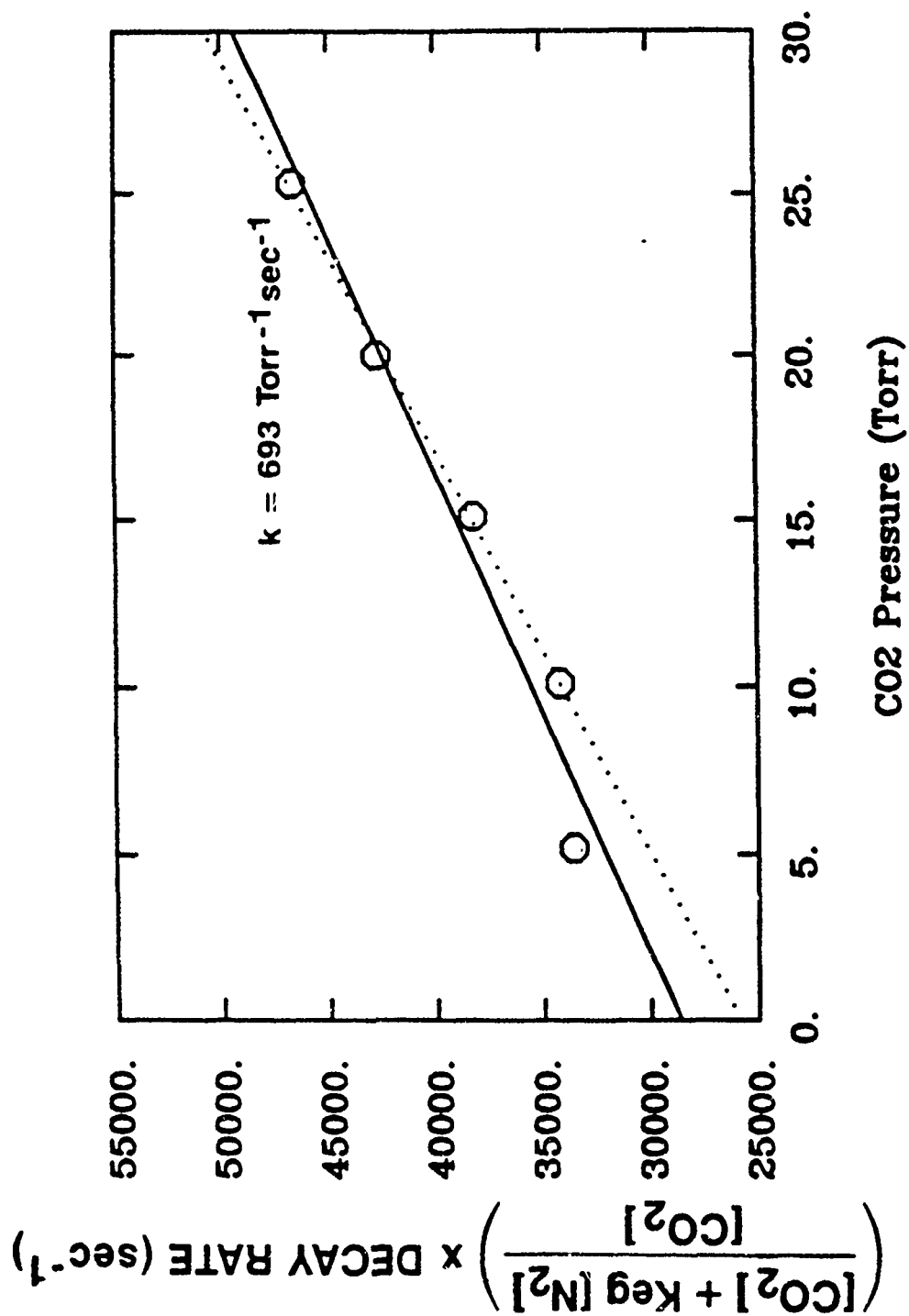


Figure 3-10. Collisional Decay Rate for C^{18}O_2 (00⁰) Level as a Function of CO_2 Pressure. Each point is an average of five measured decays.

Table 3-3

QUENCHING RATE CONSTANTS FOR THE CO_2^0 LEVEL $C^{18}O_2$ (multiple regression analysis):

k_{He-CO_2}	1.5×10^{-15}	cm^3	$molec^{-1}$	s^{-1}
$(k_{N_2-CO_2} + K_{eq} k_{CO_2-N_2})$	9.6×10^{-15}	cm^3	$molec^{-1}$	s^{-1}
$k_{CO_2-CO_2}$	2.2×10^{-14}	cm^3	$molec^{-1}$	s^{-1}

 $C^{18}O_2$ (Stern-Volmer analysis):

k_{He-CO_2}	1.7×10^{-15}	cm^3	$molec^{-1}$	s^{-1}
$(k_{N_2-CO_2} + K_{eq} k_{CO_2-N_2})$	1.1×10^{-14}	cm^3	$molec^{-1}$	s^{-1}
$k_{CO_2-CO_2}$	2.4×10^{-14}	cm^3	$molec^{-1}$	s^{-1}

 $^{13}CO_2$:

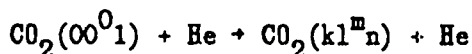
k_{He-CO_2}	2.8×10^{-15}	cm^3	$molec^{-1}$	s^{-1}
$(k_{N_2-CO_2} + K_{eq} k_{CO_2-N_2})$	1.1×10^{-14}	cm^3	$molec^{-1}$	s^{-1}
$k_{CO_2-CO_2}$	4.4×10^{-14}	cm^3	$molec^{-1}$	s^{-1}

 $^{12}C^{16}O_2$ (room temperature values):^a

k_{He-CO_2}	2.6×10^{-15}	cm^3	$molec^{-1}$	s^{-1}
$(k_{N_2-CO_2} + K_{eq} k_{CO_2-N_2})$	3.3×10^{-15}	cm^3	$molec^{-1}$	s^{-1}
$k_{CO_2-CO_2}$	1.1×10^{-14}	cm^3	$molec^{-1}$	s^{-1}

^a Reference 9

Several differences are apparent in the $C^{18}O_2$, $^{13}CO_2$ and normal CO_2 rate constants. Considering the He collision partner first, collisional quenching of $C^{18}O_2$ by He is much less efficient than quenching of either $^{13}CO_2$ or normal CO_2 . This could simply be a kinematic effect, where the heavier terminal ^{18}O atoms are perturbed less by the He collision partner than the ^{16}O atoms would be. The variation may be due to slight differences in where target levels of CO_2 lie with respect to the 00^0_1 level and on the degree of mixing of the vibrational levels.^(16,17) Examples of target vibrational levels that may be born in collisional quenching by CO_2 ,



are the 12^0_0 , 11^1_0 , 20^0_0 , 03^1_0 and 04^0_0 levels. The rate constants with a CO_2 collision partner show the greatest variation among the different isotopic forms. Again, the difference in the rate constants may be due to different positioning of the target levels with respect to the 00^0_1 levels. The target levels will be the same as those just mentioned. Another contributing factor to the variation in the rate constants would be differences in the infrared activity of the CO_2 vibrations among the isotopic forms. Infrared activity plays an important role in enhancing the quenching rate, as has been shown for collisional quenching of $^{12}C^{18}O_2(00^0_1)$ by various infrared-active and infrared-inactive collision partners.⁽¹⁸⁾ The only significant difference in rate constants with an N_2 collision partner is that the normal CO_2 rate constant is significantly lower than either the $C^{18}O_2$ or $^{13}CO_2$ rate constants. As with the He and CO_2 collision partners, the difference might be explained by positioning of the target levels. The situation with N_2 is complicated somewhat by the fact that $N_2(v = 1)$ is quenched by CO_2 as well. Greater than 2000 cm^{-1} of energy needs to be dissipated when $N_2(v = 1)$ is quenched. However, this path could proceed via a direct energy transfer path from $N_2(v = 1)$ to excite CO_2 levels have one or more bending mode quanta, followed by a rapid vibration to translational relaxation of the bending mode. Regarding any of these comments, it has to be realized that in making comparisons of the $C^{18}O_2$ or $^{13}CO_2$ rate constants to the room temperature values for normal CO_2 from

laser-induced fluorescence experiments, the high pressure discharge leads to non-equilibrium conditions or high temperatures in the internal degrees of freedom, so that such comparisons to measurements at close to equilibrium conditions might not be appropriate.

3.3.2 Small Signal Gain

In a separate experiment, we have measured the maximum value of the small signal gain for several of the $C^{18}O_2$ transitions. The specific transitions tested were R(20) and P(18) of the $(00^0_1) - (02^0_0)$ band, and P(18) of the $(00^0_1) - (10^0_0)$ band. In addition, the small signal gain was determined for the P(18) transitions of both bands in normal CO_2 as a reference. The gas compositions for all of the measurements was 325/50/25 torr of He/ N_2 / CO_2 , and the energy loading was 50 J/l-atm. The measured gains are shown in Table 3-4. The gain on each transition is an average over five measurements. Also listed in Table 3-4 are small signal gains for the P(18) transitions of both bands in $^{13}CO_2$ that were determined in an earlier study at STI.⁽⁶⁾ The gas composition and the energy loading were comparable to those used here.

The temporal gain traces for the measurements reported in Table 3-4 were compared with model predictions in order to estimate the transition moments for the 828 CO_2 $(00^0_1 + 10^0_0)$ and $(00^0_1 + 02^0_0)$ bands. These were summarized in Table 2-1 and compared with similar data for 828 and 636 CO_2 . The collisional-relaxation rate constants measured in this section were used in our CO_2 kinetics model after adjusting for the appropriate 828 energy level spacings. The transition dipole moment was then adjusted to give the best agreement with the measured gain curves as described in Section 2.

Table 3-4

SMALL SIGNAL GAINS ($\text{He/N}_2/\text{CO}_2 = 325/50/25$ torr)

CO_2 Line	I/I_0	g_0 ($\% \text{ cm}^{-1}$)
C^{18}O_2 ($00^0_1 - 02^0_2$) P(18)	4.64 ± 0.08	1.71 ± 0.03
C^{18}O_2 ($00^0_1 - 02^0_0$) R(20)	4.07 ± 0.07	1.56 ± 0.03
C^{18}O_2 ($00^0_1 - 10^0_0$) P(18)	1.85 ± 0.02	0.68 ± 0.02
C^{18}O_2 ($00^0_1 - 02^0_0$) P(18)	2.74 ± 0.03	1.12 ± 0.02
C^{18}O_2 ($00^0_1 - 10^0_0$) P(18)	3.11 ± 0.03	1.26 ± 0.02
$^{13}\text{C}^{16}\text{O}_2$ ($00^0_1 - 02^0_0$) P(18)		0.73
$^{13}\text{C}^{16}\text{O}_2$ ($00^0_1 - 10^0_0$) P(18)		1.8

Section 4

SELF-SUSTAINED DISCHARGE, SINGLE-LINE EXTRACTION MEASUREMENTS

4.1 INTRODUCTION

Under self-sustained conditions, the ionization necessary for conduction by the discharge is provided by the discharge itself, through electron-impact ionization of the laser medium itself. Such lasers must be preionized immediately before application of the discharge pulse, but require no additional ionization source during the discharge. Although potentially simpler to implement than electron-beam sustained lasers, they are subject to discharge instabilities that limit the energy loading (and therefore extracted energy). Furthermore, the E/N of the discharge is determined by internal factors, and cannot be controlled externally as is possible in an E-beam sustained laser. The discharge may operate at an E/N leading to poor excitation of the upper laser level, so this loss of control over the discharge conditions can lead to inefficient operation. The goal of the single-line extraction, self-sustained discharge measurements was to measure the efficiency and extractable energy on the 9.11- μm R(20) line of $^{12}\text{C}^{18}\text{O}_2$, to allow comparison of self- and E-beam sustained discharge excitation and provide a basis for later critical system trade-off studies.

4.2 EXPERIMENTAL ARRANGEMENT

The Lucy self-sustained discharge laser used in the small-signal gain and relaxation measurements was also used for single-line extraction measurements. The glass tube and electrode structure was as described in Section 3.2, as was the x-ray preionization system.

The nine-section PFN appropriate for the small-signal gain and relaxation measurements was changed for the extraction measurements, because the low impedance of that PFN was incorrect for "rich" gas mixes containing large fractions of N_2 and CO_2 . The PFN was replaced with a

seventeen-section PFN with $C = 50 \text{ nF}$ and $L = 130 \text{ } \mu\text{H}$. The PFN was tapered by reportioning the inductance between sections to produce desirable voltage and current waveforms for high energy loading. As shown in Figure 4-1a, the waveform begins with a strong voltage spike to over avalanche the laser gas, followed by a sustaining pulse. The sustaining pulse voltage is made to decrease slightly over its $5\text{-}\mu\text{sec}$ duration, suppressing the tendency of the discharge to become unstable and arc near the end of the pulse. The same PFN configuration was used for all gas mixtures and pressures, but the PFN was reasonably well matched for all the cases studied. As for the gain and relaxation measurements, Tektronix 2430 digitizing oscilloscopes recorded the discharge current and voltage. The data were stored on an IBM PC and transferred to a VAX mainframe computer network for analysis.

All the measurements for this phase of the program were done by filling the Lucy system with the appropriate partial pressures of He, N_2 , and CO_2 containing the appropriate isotope. Gas regeneration was found to be unnecessary for the number of shots typically fired in one series of measurements, and lack of rapid gas degradation was verified by the slight but insignificant decrease in extracted energy during measurements on a given gas fill.

The laser cavity was a simple multi-mode stable resonator, consisting of a grating (150 lines/mm, $9\text{-}\mu\text{m}$ blaze) and a ZnSe output coupler (radius of curvature 10 m, 60% reflectivity). The dimensions of the optics slightly exceeded the area of the pumped region, defined by the 4-cm electrode spacing and 3.6-cm discharge width. The laser output impinged upon the surface of a calibrated calorimeter connected to a chart recorder. The calorimeter and chart recorder were calibrated using a regulated power supply to apply a constant voltage to the calibrated resistance wire inside the calorimeter. The results given here conservatively assume 100% absorption of the CO_2 laser radiation by the calorimeter; if the absorption were less, the actual extracted energies and efficiencies would exceed those reported here. A fast Ge: Au photodetector measured the laser temporal profile by observing the diffuse scatter from the surface of the calorimeter. The waveform from the photodetector was recorded by a Tektronix 2430 digital oscilloscope (a second Tektronix 2430 recorded the

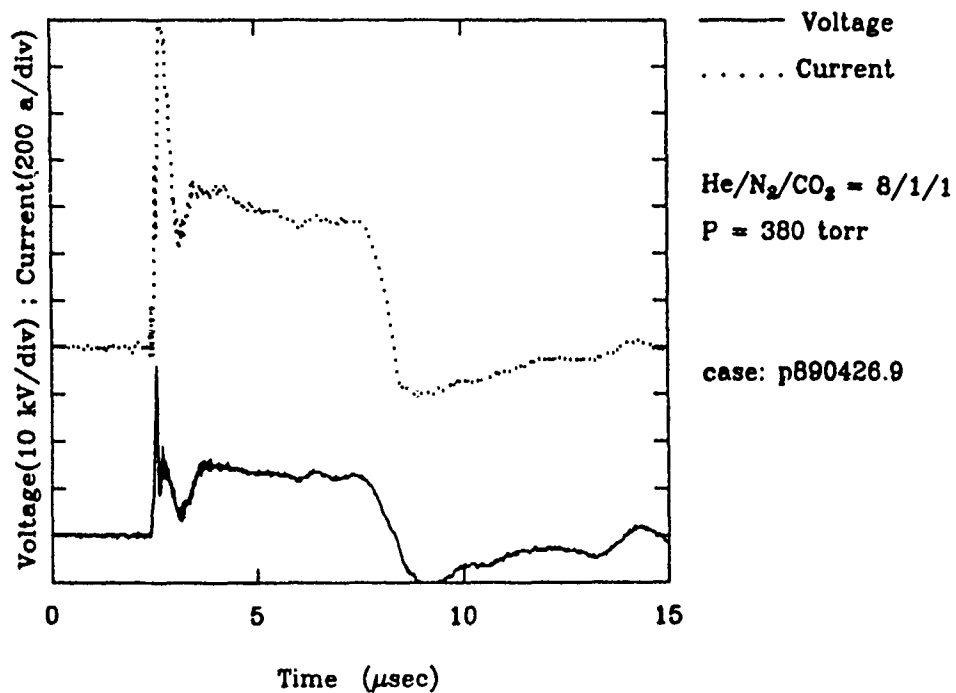


Figure 4-1a. Experimental Voltage and Current.

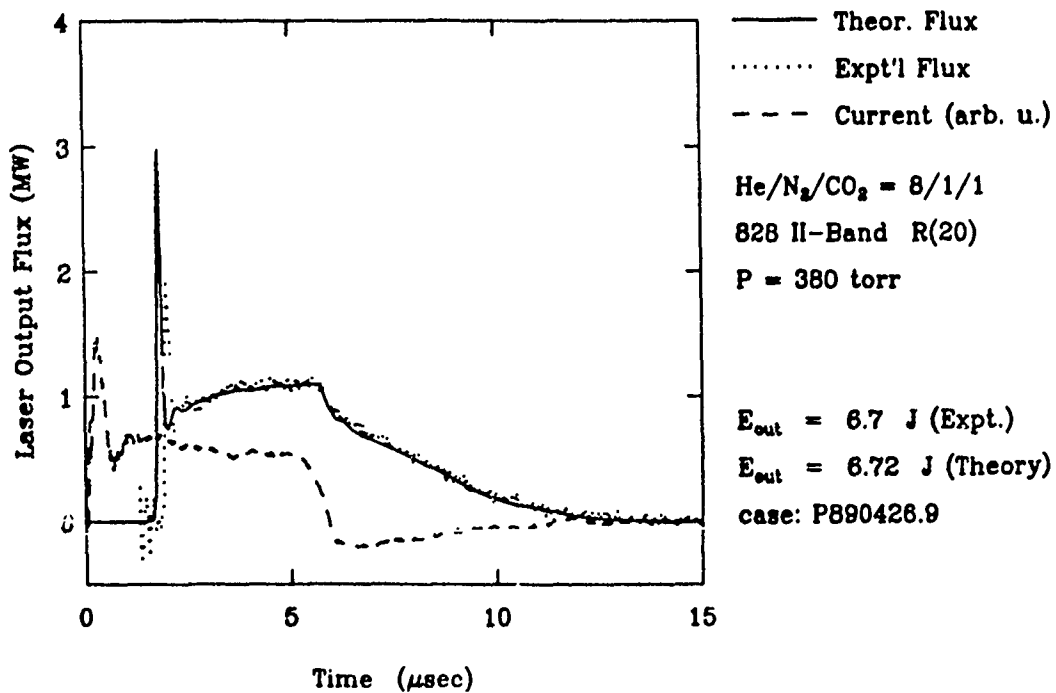


Figure 4-1b. Experimental and Theoretical Output Flux.

voltage and current waveforms) and stored by the IBM PC computer. Periodically, the output was directed into a spectrum analyzer to verify that the output consisted of the particular line of interest. Burn patterns of the output were also taken to confirm proper optical alignment.

Subsequent to the recording of the self-sustained discharge data on Lucy, it was realized that at the highest output energies obtained, the signal observed by the photodetector did not precisely reproduce the laser output, probably due to plasma formation at the calorimeter surface. This difficulty did not affect the data at lower extracted energies, and only the recording of laser waveform (not the discharge characteristics or total extracted energy) was affected at the higher energies.

4.3 ENERGY EXTRACTION RESULTS

4.3.1 General Features

Results were first obtained extracting on the II R(20) line of $C^{16}O_2$. Examples of the voltage and current waveforms are shown in Figure 4-1a. The PFN has been designed to give a strong leading voltage spike to efficiently avalanche the laser gas, then to supply energy at a decreasing rate as the excitation continues. The observed laser output corresponding to the excitation of Figure 4-1a is shown in Figure 4-1b, along with the results of the STI CO_2 laser model. The optical pulse shows a gain-switched spike, followed by a pulse which begins to decay exponentially as the excitation pulse terminates.

4.3.2 Effects of Energy Loading

The energy loaded into the discharge can be varied by changing the charging voltage of the PFN. Only a limited range of energy loadings is available for a given gas mixture and PFN configuration, because too much energy loading leads to runaway instabilities in the gas, causing arcing, while obtaining low energy loading requires charging voltages too low to sufficiently avalanche the discharge. A range of energy loadings with a given PFN configuration can be examined by changing gas composition.

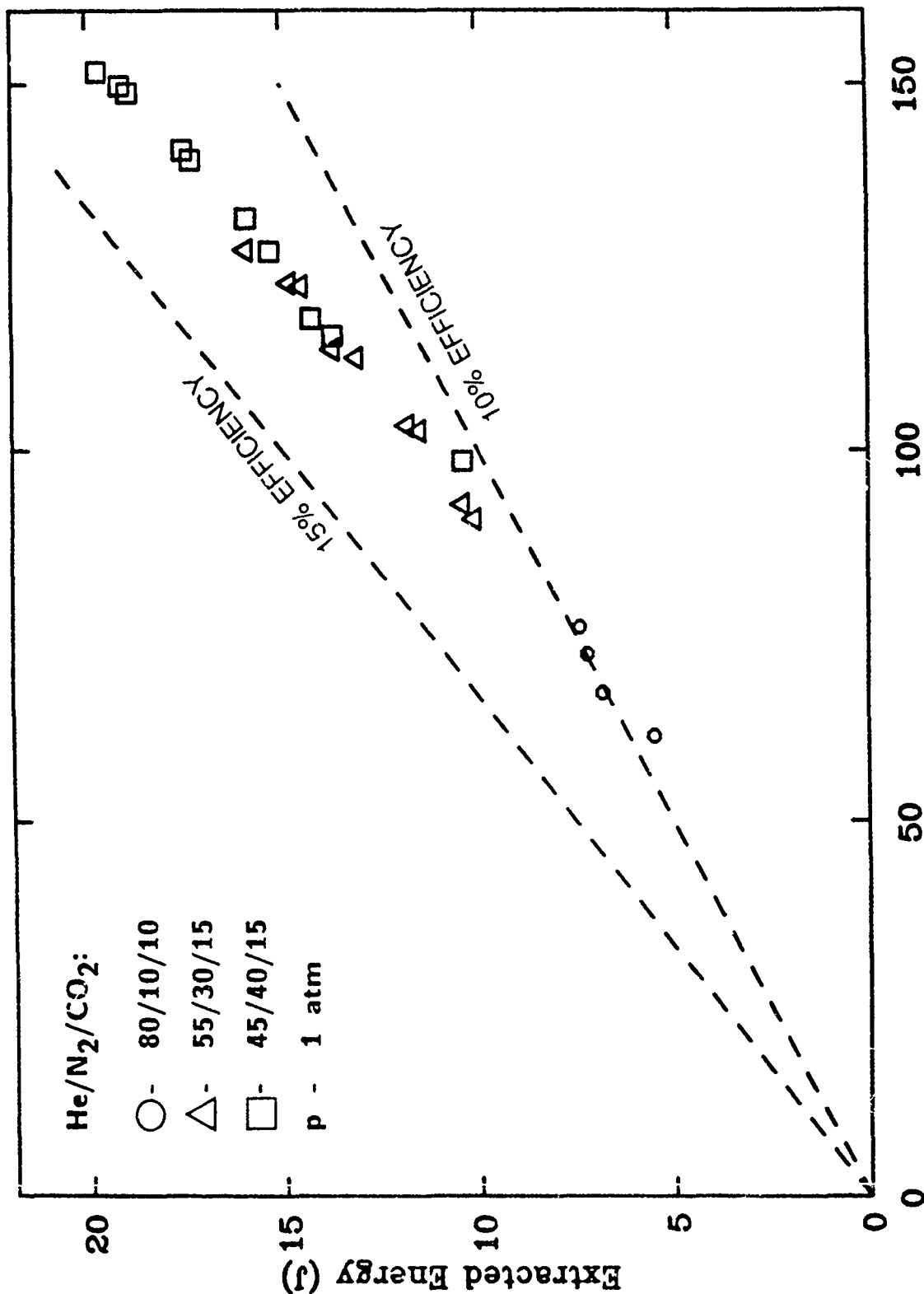
Higher energy loading can be applied to mixtures containing higher concentrations of N_2 and CO_2 , because their large heat capacities allow more energy to be deposited without excessive instabilities. Their presence leads to higher breakdown and sustaining voltages, however.

To measure energy extraction over a wide range of energy loading, energy extracted on the R(20) line of $^{12}C^{16}O_2$ was measured over a range of PFN charge voltages, for several different gas mixtures. The results are plotted in Figure 4-2. Although the data follow a linear trend, it may be seen that the intrinsic efficiency apparently increases with energy loading. There are a number of factors which influence efficiency, including the details of the PFN design and the composition of the laser gas. The results of the STI CO_2 laser model show that the ratio of nitrogen to carbon dioxide strongly influences the efficiency under self-sustained excitation, as discussed later in Section 6.3.

4.3.3 Extraction Efficiency

Of the several gas mixtures examined, two mixtures were chosen for detailed studies: a "lean" mixture, with proportions of helium, nitrogen, and carbon dioxide in the ratio 80/10/10, and a "rich" mixture, with ratio 45/40/15. These mixtures were studied both at a total pressure of one atmosphere and also at 0.5 atm, which may be desirable to minimize chirp. Since the same PFN was used for all gas mixtures, it was not possible to optimize the performance for each mixture. Nevertheless, the matching of the PFN to the laser gas was sufficiently good that the PFN delivered little or no energy after the nominal 5- μ sec excitation pulse.

As was done for the gain measurements, a series of discharges in a hydrogen mixture were run to prevent contamination of the rare isotope by ordinary CO_2 . Only after this treatment was the laser re-filled with laser mixtures containing the rare isotope, and the laser was operated for tens of shots on a fill containing the new isotope before filling with the isotopic mixtures on which the data reported here were taken. The performance of mixtures containing the rare isotope was found to degrade no more rapidly than the performance of mixtures containing the ordinary isotope.



Loaded Energy (J)

Figure 4-2. Extracted Energy as a Function of Energy into the Discharge ($E_{dis} = \int V \cdot Idt$) and the II R(20) Line of $^{12}C^{16}O_2$ in Gas Mixture for the Lucy Self-sustained Discharge Laser.

Examples of the $^{12}\text{C}^{18}\text{O}_2$ data are shown in Figures 4-1, 4-3, and 4-4. Data were taken at the benchmark pressures and mixtures used for the experiments on the normal isotope and also for a mixture containing an intermediate concentration of N_2 . For the lean mixture at 0.5 atm, 8.7 J were obtained on the 828 II R(20) line at $9.1\ \mu\text{m}$. The current, voltage, optical, and model traces are shown in Figure 4-1. The lean mixture at reduced pressure shows a relatively long decay time, augmented in this case by slight additional pumping past the nominal 5- μsec pulse duration. The same mixture at one atmosphere (Figure 4-3) shows a more rapid relaxation rate, primarily due to the factor of two increase in absolute CO_2 concentration, which is the most effective relaxer in the system. Figure 4-4 shows data for a rich mixture at 1-atm total pressure.

A summary of our measurements near the maximum energy loading for each gas mixture and pressure are reported in Table 4-1. Very good energy extraction was achieved in the measurements on the normal CO_2 isotope, indicating that the optical design was reasonably efficient and that the preionizer and discharge circuitry were performing properly. Considerably higher energy could be obtained from a mix rich in N_2 and CO_2 , and the laser produced significantly higher output at 1 atm than at 0.5 atm, due to the higher energy loading achieved for these cases. Experiments extracting on the R(24) line of the C^{18}O_2 isotope yielded results essentially identical to the results for the R(20) line. (Although the gain of the R(24) line is lower, the laser is operating in the gain-saturated regime.) The gain on the 626 II R(24) line is anomalously high due to overlap with sequence band transitions.⁽⁷⁾ It was necessary to increase the gain in the model to match the experimental turn-on times.

The trends observed in the $^{12}\text{C}^{16}\text{O}_2$ data were confirmed in the $^{12}\text{C}^{18}\text{O}_2$ data. The richer mixes allowed greater specific energy loading, and exhibited significantly higher efficiencies than the lean mixture. Slightly better efficiencies were obtained at 0.5 atm than at 1 atm, although the difference was more pronounced for the lean mixture than for the rich mixture. The efficiency of mixtures containing $^{12}\text{C}^{18}\text{O}_2$ was consistently better than the efficiency of mixtures containing $^{12}\text{C}^{16}\text{O}_2$.

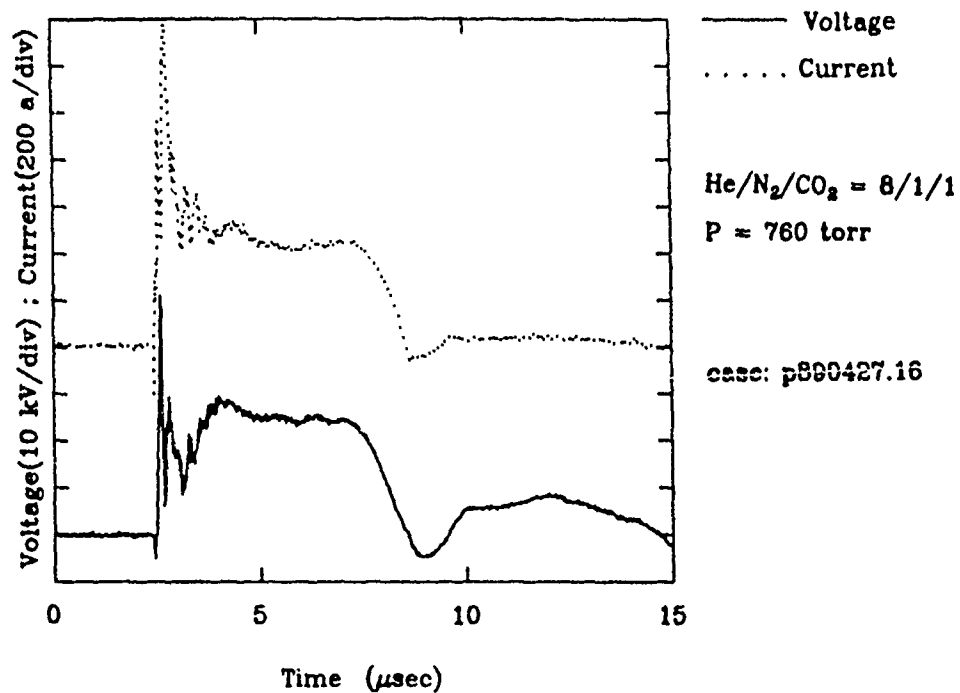


Figure 4-3a. Experimental Voltage and Current.

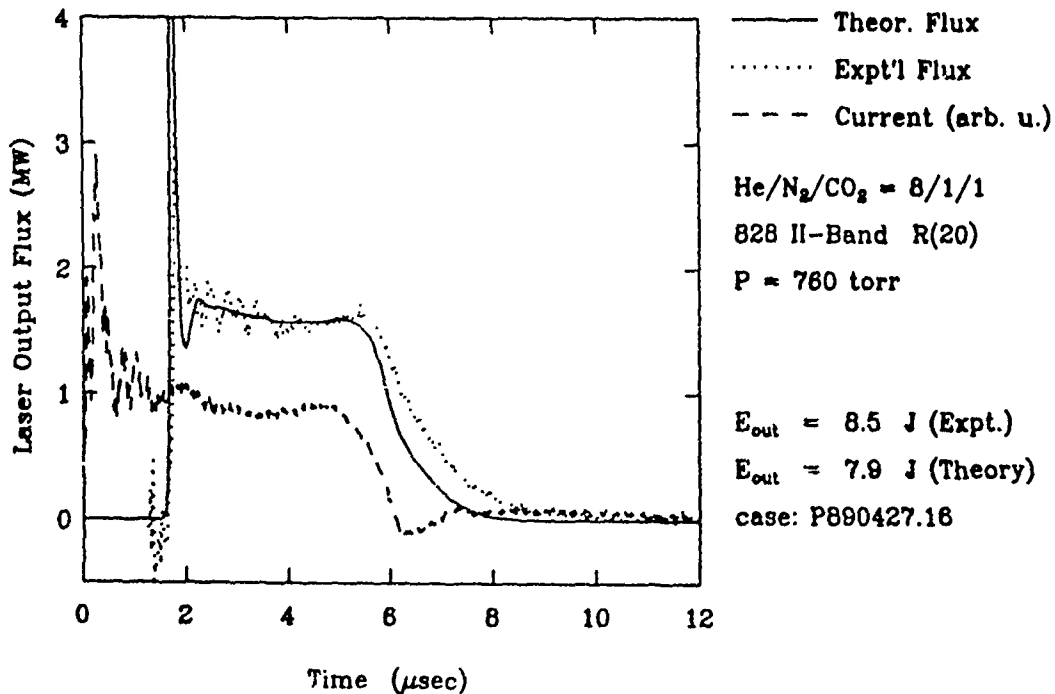


Figure 4-3b. Experimental and Theoretical Output Flux.

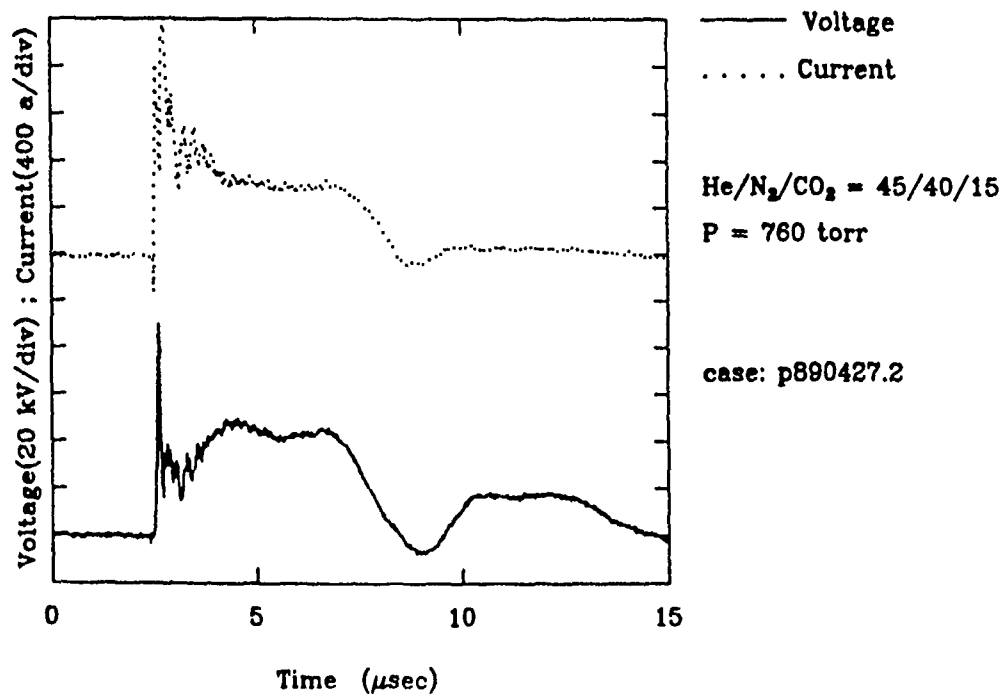


Figure 4-4a. Experimental Voltage and Current.

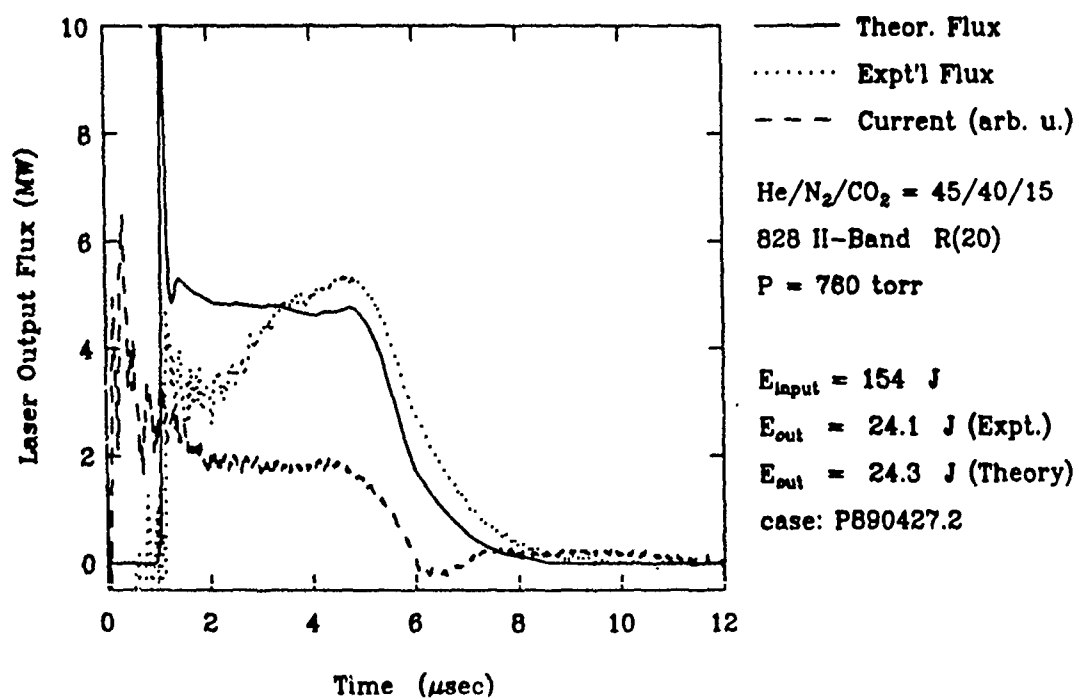


Figure 4-4b. Experimental and Theoretical Output Flux.

Table 4-1

R(20) SINGLE-LINE EXTRACTION FROM ISOTOPIC CO₂
EXCITED BY A SELF-SUSTAINED DISCHARGE

Isotope	Mixture He/N ₂ /CO ₂	Pressure (torr)	Energy Loading (J/l-atm)	Extracted Energy		Intrinsic Efficiency(%) *
				Total(J)	(J/l-atm)	
626	80/10/10	380	75.0	5.7	8.8	11.7
828	80/10/10	380	75.0	6.7	10.3	13.8
626	45/40/15	380	117.8	11.2	17.2	14.6
828	45/40/15	380	117.2	12.0	18.5	15.7
626	80/10/10	760	52.3	7.4	5.7	10.9
828	80/10/10	760	52.5	8.5	6.5	11.4
828	63/27/10	760	94.3	19.2	14.8	15.7
626	45/40/15	760	119.0	19.7	15.2	12.8
828	45/40/15	760	119.3	24.1	18.5	15.5
828	45/40/15	760	127.5	25.2	19.4	15.2

R(24) Single-Line Extraction

626	80/10/10	380	78.4	6.3	9.7	12.4
626	45/40/15	380	117.8	11.2	17.2	14.6
626	80/10/10	760	57.7	7.8	6.0	10.4
626	45/40/15	760	114.5	20.5	15.8	13.8

* Intrinsic Efficiency = Laser Energy / $\int V \cdot I \cdot dt$

4.4 CORRESPONDENCE WITH MODEL

The STI CO_2 laser model accurately reproduces the results obtained using the Lucy self-sustained discharge laser. The model predicts the extracted energies very well, including the better performance by $^{12}\text{C}^{18}\text{O}_2$ over $^{12}\text{C}^{16}\text{O}_2$. This indicates that the pumping, loss, and extraction processes are appropriately treated by the model. The agreement between the model and the actual laser waveforms is also very good, as can be seen in Figures 4-1 and 4-3. The delay between the onset of pumping and lasing is determined by the gain of the medium and the various loss and outcoupling mechanisms. The close agreement here confirms the small-signal gain measurements, and the values chosen or measured for cavity losses and outcoupling. The model employs relaxation rate constants determined by the work described in Section 3. These relaxation rates are important to the prediction of the laser decay after pumping terminates, so the agreement between model and experiment in the waveforms supports these results as well.

4.5 SUMMARY

The results show that efficient operation of self-sustained $^{12}\text{C}^{18}\text{O}_2$ lasers is possible, particularly for certain gas mixtures. Extracted energy and efficiency from C^{18}O_2 were actually higher in all cases than the very good values obtained from the normal isotope. This is probably due to the higher gain for the 828 - R(20) transition resulting in a faster laser turn-on time. In fact, intrinsic efficiencies greater than 15% were readily obtainable in this self-sustained discharge laser, and extracted energies approaching 20 J/l-atm were attained. These numbers are unusually high for self-sustained discharge lasers, which more typically operate at efficiencies of 10% and extracted energies o. 10 J/l-atm. Improvements beyond these results could be made by optimization of gas mix and pressure, improvements in the pulse-forming network, and optimization of the optical system.

Section 5

E-BEAM SUSTAINED DISCHARGE, SINGLE-LINE EXTRACTION MEASUREMENTS

5.1 INTRODUCTION

In an E-beam sustained discharge laser, the ionization necessary for discharge conduction is provided by an externally generated electron beam. This configuration is comparatively resistant to discharge instabilities, and consequently is capable of high energy loading. Because the E-beam allows independent control of the discharge characteristics, the discharge E/N may be adjusted for optimum pumping efficiency.

E-beam sustained devices are more complex than self-sustained devices, both in terms of the required hardware and in the many factors which must be considered in measurements and assessments of overall efficiency. Consequently, our experimental research program included spatially-resolved gain measurements of the discharge, and variation of pressure, mixture, isotopic composition, and degree of e-beam preionisation. These results spurred detailed modeling efforts that have led to new understandings of the effects of discharge conditions and gas mixture upon the efficiencies of E-beam and self-sustained discharge lasers.

5.2 DELILAH APPARATUS

The DELILAH device was used to gather data on single-line extraction from electron-beam sustained $^{12}\text{C}^{18}\text{O}_2$ laser discharges. DELILAH utilizes a row of ten plasma-diode electron guns to provide the ionizing E-beam. The plasma-diode E-beam source employs a high voltage discharge (about 100 kV) in low-pressure (30-60 mTorr) helium. The advantages are that the device uses a cold cathode and avoids the complexity of a hot cathode e-beam, can produce long pulse durations if necessary, and is a simple technology that is easily implemented.

A conceptual diagram of the DELILAH device is shown in Figure 5-1, illustrating the essential features of the plasma diode E-beam sustained discharge. The electrons are accelerated by applying approximately 100 kV between the solid aluminum cathodes and the screen anodes of the plasma diodes. The electrons pass through the anode screen and through a drift region until they reach the foil. After passing through the foil, which separates the low pressure plasma diode region from the high pressure discharge region, the high energy electrons pass through a 3-cm drift region between the foil and the discharge anode screen before entering the discharge region itself. These high energy electrons ionize the gas molecules in the discharge region, providing secondary electrons to carry the current when the low E/N discharge pump pulse is applied. Since the current carrying electrons are supplied by the external E-beam source and not the discharge itself, the discharge E/N can be adjusted for optimum pumping of the CO_2 and N_2 vibrational levels.

A photograph of the DELILAH E-beam sustained discharge laser is shown in Figure 5-2. The cylindrical discharge chamber is 30 cm in diameter by 140-cm long, with a total volume of 80 l. The spacing between the cathode screen and the anode was adjusted to 4 cm. The anode has a flat region 7.8-cm wide, but the discharge width is strongly influenced by a 3-cm wide aperture in the anode screen through which electrons pass. The discharge length was 90 cm.

The plasma diode E-beam source is powered by two-stage Marx bank. Typically, the E-beam source was switched on 2 μsec before firing the PFN to allow the E-beam current to stabilize, and crowbarred several microseconds after the PFN pulse terminated. In a few studies, the Marx bank was crowbarred as the PFN was triggered, allowing DELILAH to run as an e-beam preionized, self-sustained discharge laser. The discharge was powered by a 7-stage type-E PFN, consisting of seven 50-nF capacitors with an 18- μH inductor, giving a 5- μsec discharge pulse. As for the other measurements carried out for this program, Tektronix 2430 digitizing oscilloscopes recorded the discharge current and voltage waveforms. Data were stored on an IBM PC and analyzed after transfer to a VAX mainframe computer network.

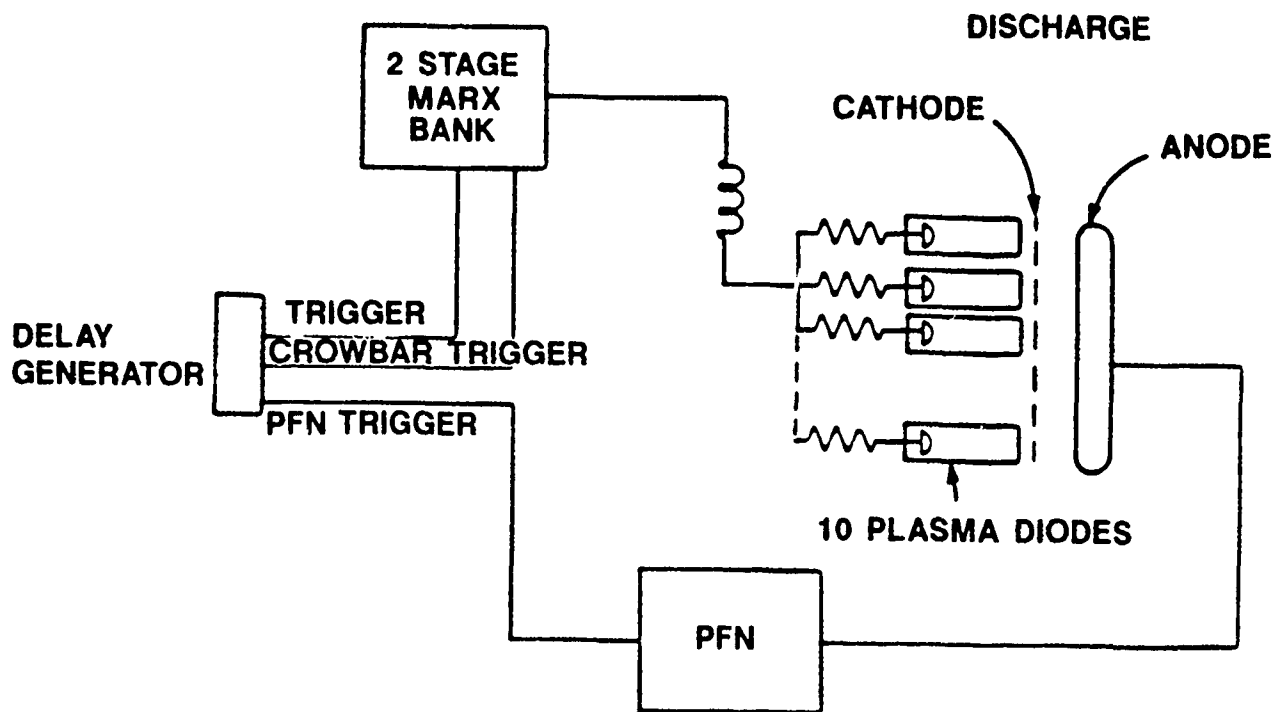


Figure 5-1. General Overall Electrical Schematic of Delilah e-Beam Sustained Discharge Laser.

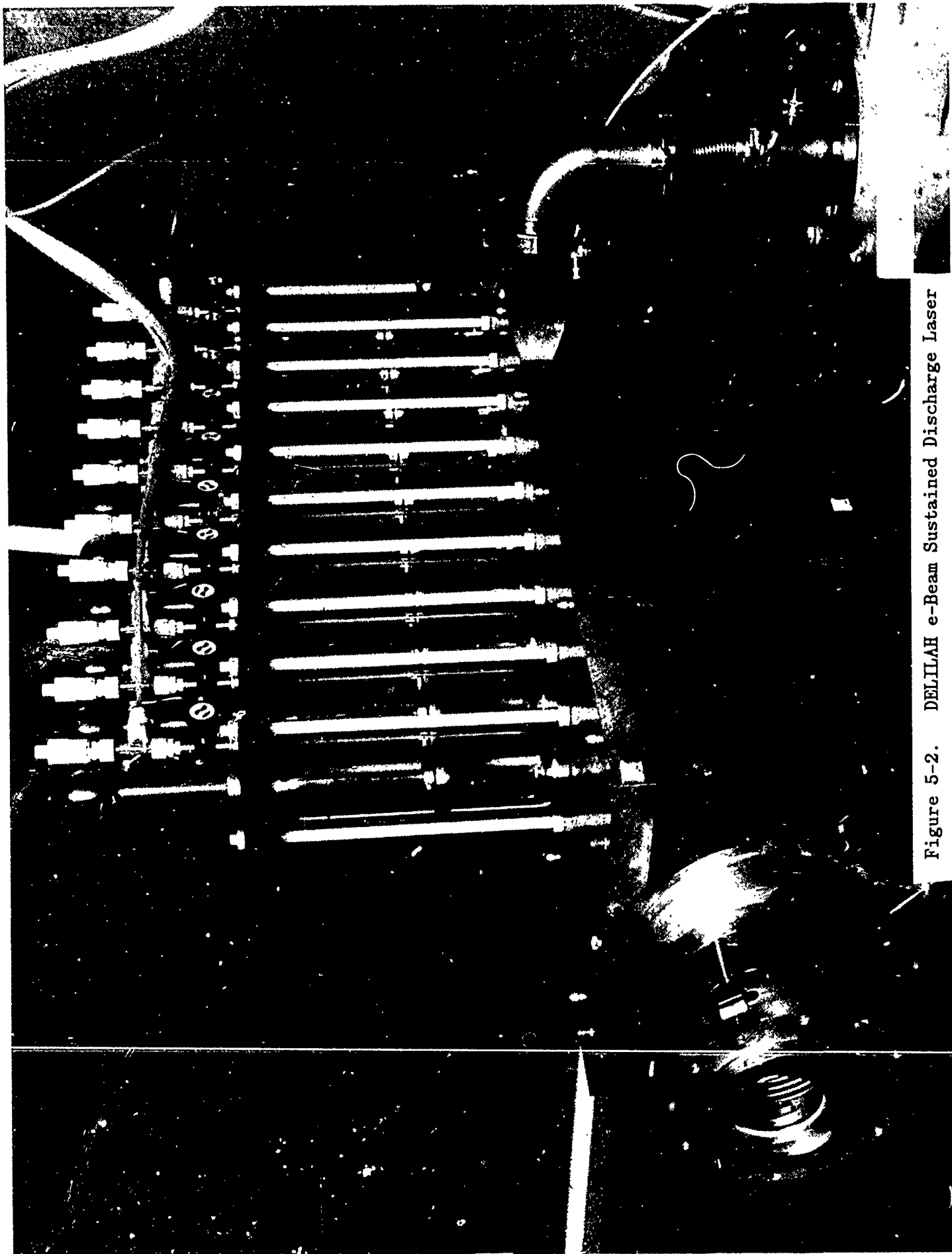


Figure 5-2. DELILAH e-Beam Sustained Discharge Laser

All the measurements for this phase of the program were done by filling the DELILAH system with the appropriate partial pressures of He, N₂, and CO₂ containing the appropriate isotope. Gas regeneration was found to be unnecessary for the number of shots typically fired in one series of measurements, and lack of rapid gas degradation was verified by the insignificant decrease in extracted energy during measurements on a given gas fill.

As for the measurements on the Lucy device, a series of discharges in a hydrogen mixture were run prior to experiments using ¹²C¹⁸O₂, to prevent contamination of the rare isotope by ordinary CO₂. Only after this treatment was the laser re-filled with laser mixtures containing the rare isotope, and the laser was operated for tens of shots on a fill containing the new isotope before filling with the isotopic mixtures on which the data reported here were taken. The performance of mixtures containing the rare isotope was found to degrade no more rapidly than the performance of mixtures containing the ordinary isotope.

5.3 DISCHARGE PERFORMANCE

Samples of the discharge voltage and current for the DELILAH device are shown in Figures 5-3a thru 5-5a. At 1-atm total pressure, the E-beam sustained results (Figure 5-3a) show an initial phase of high discharge voltage and increasing discharge current lasting approximately 1 μ sec. The discharge then settles down to conditions typical of E-beam sustained conditions, with $E/N \approx 2 \times 10^{-16}$ V cm². After about 5 μ sec, the discharge terminates. E-beam sustained operation at 0.5 atm (Figure 5-4a) has similar characteristics, although there is partial voltage collapse near the end of the discharge due to impedance mismatch with the PFN under these conditions. Self-sustained operation (Figure 5-5a) was also possible at 0.5 atm, by crowbaring the Marx bank supplying the plasma diode E-guns when the PFN was triggered. Here we see sustaining voltage yielding $E/N \approx 4 \times 10^{-16}$ V cm². Although there is some voltage ringing under the self-sustained conditions, due to the higher discharge impedance, the pumping rate after 5 μ sec is low.

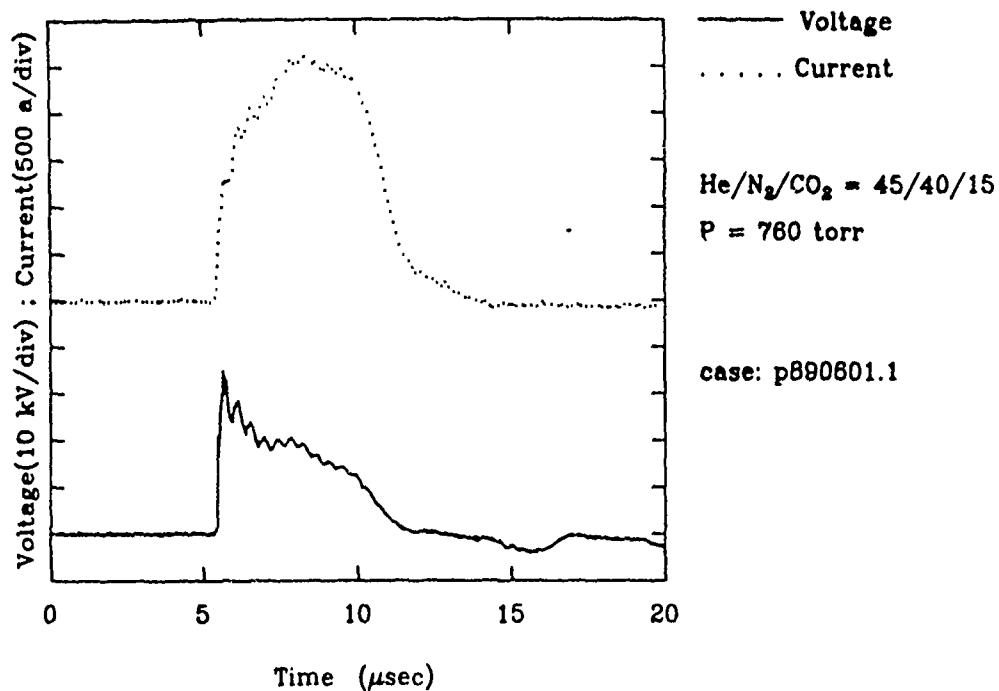


Figure 5-3a. Delilah: Experimental Voltage and Current.

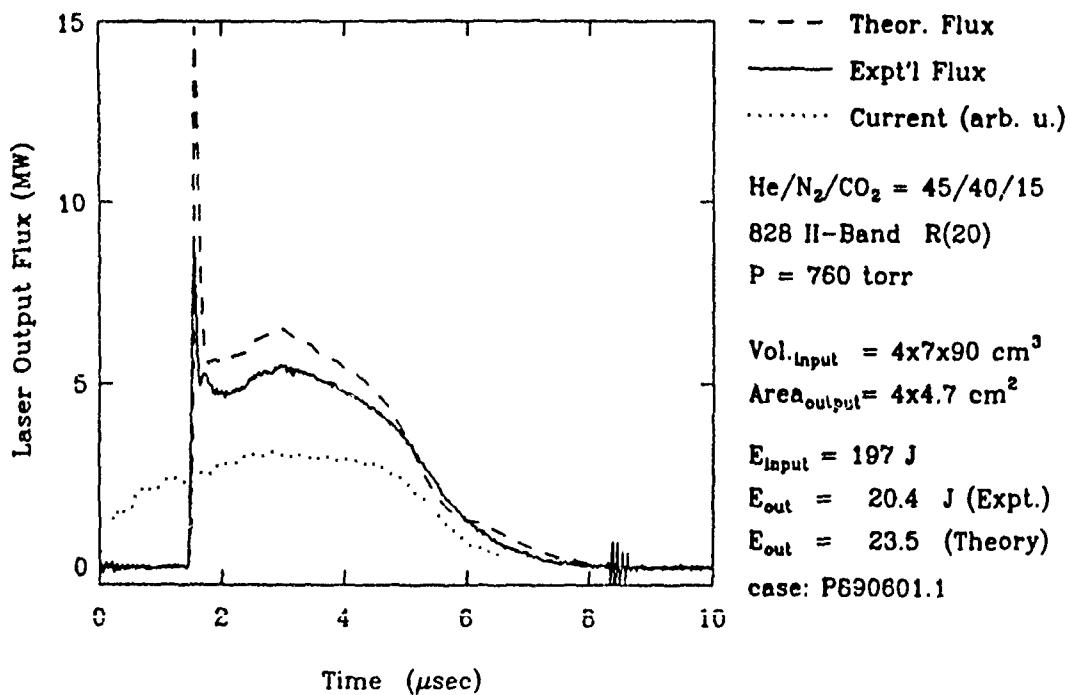


Figure 5-3b. Delilah: Experimental and Theoretical Output Flux.

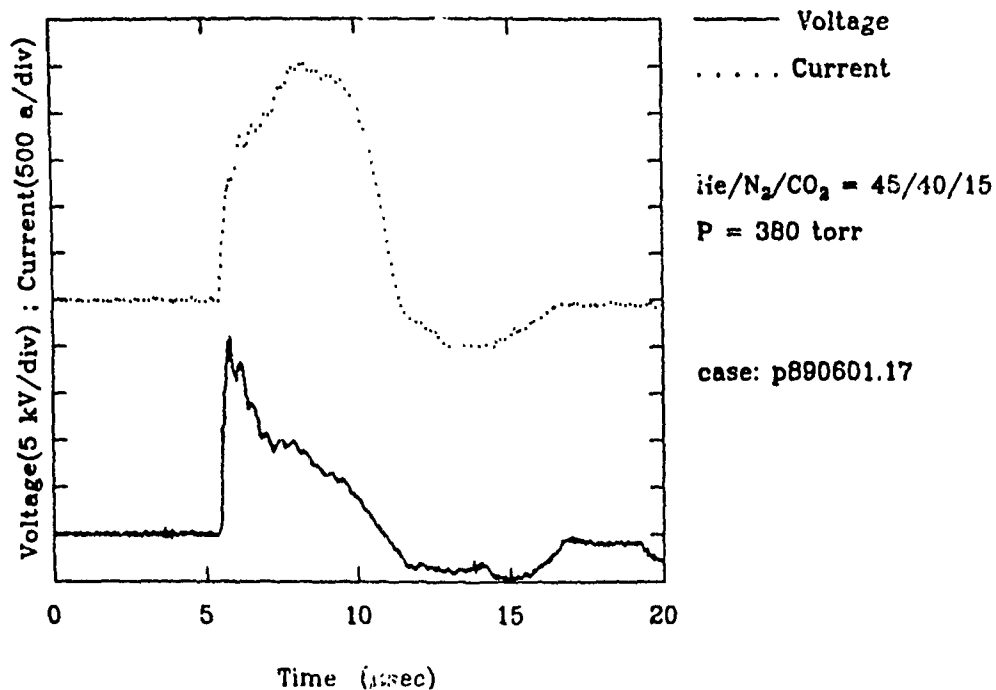


Figure 5-4a. Delilah: Experimental Voltage and Current.

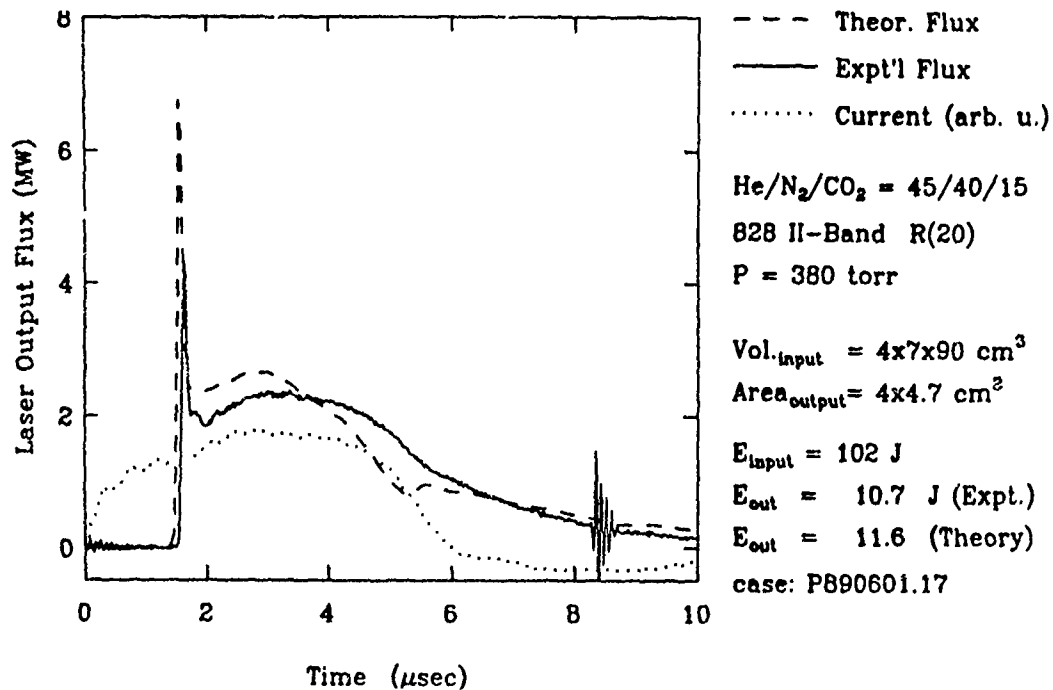


Figure 5-4b. Delilah: Experimental and Theoretical Output Flux.

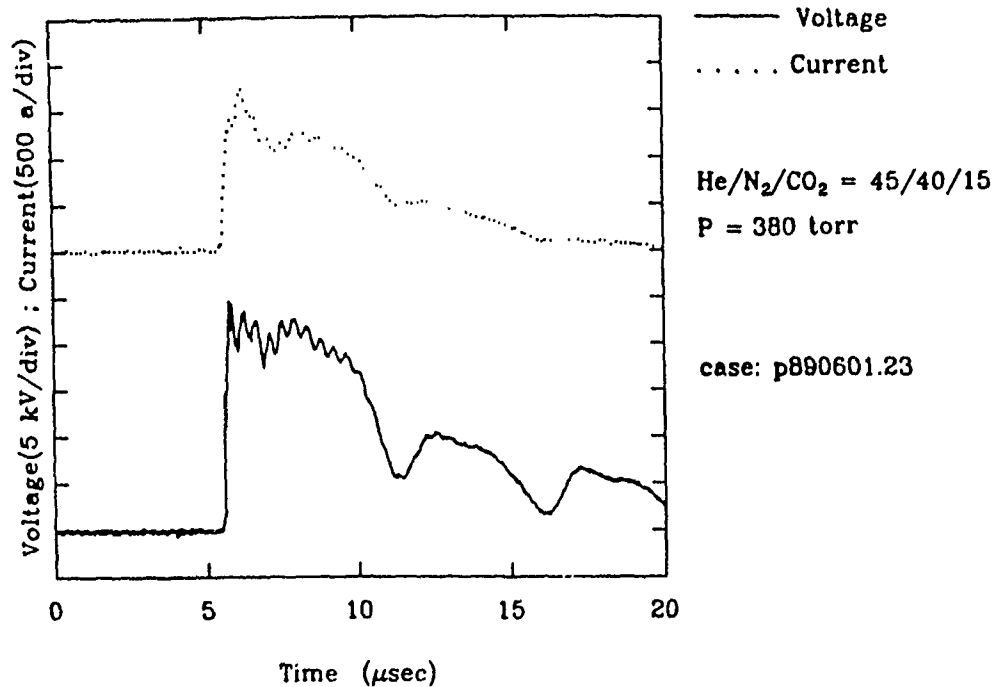


Figure 5-5a. Delilah: Experimental Voltage and Current.

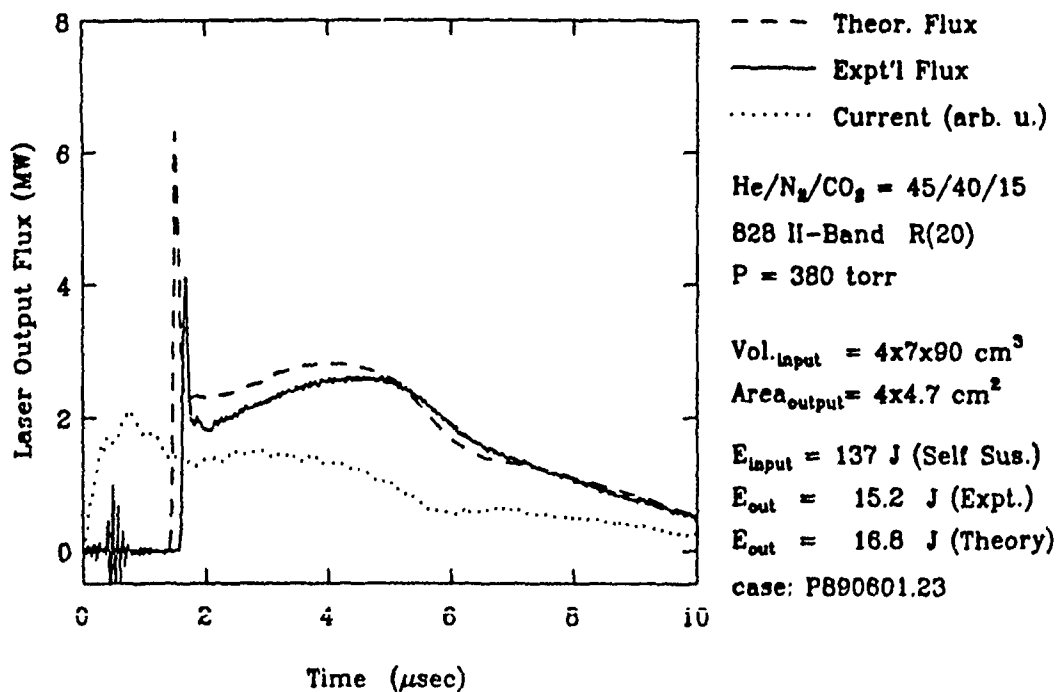


Figure 5-5b. Delilah: Experimental and Theoretical Output Flux.

5.4 GAIN MEASUREMENTS

5.4.1 Gain Diagnostics

The configuration of diagnostic equipment for gain measurements on DELILAH was essentially similar to the configuration used on the Lucy device, as described in Section 3.

5.4.2 Results

To characterize the spatial variation of the energy loading, the gain of the DELILAH device operating with $^{12}\text{C}^{18}\text{O}_2$ was measured in a pattern of eleven points, covering essentially the entire pumped volume. These gain measurements were carried out under e-beam sustained conditions both at 1 atm and at 0.5 atm. In addition, gain was measured at 0.5 atm with the laser running E-beam preionized, self sustained, to allow direct comparison between the two modes of operation.

The timing of the experiment is arranged so in a single trace, a baseline (with no probe laser) is observed, the unamplified probe is observed, and finally the probe amplified by the active discharge is observed. This allows unequivocal baseline correction of the data to be performed. The decay of laser gain may also be analyzed, for comparison with the kinetic data described in Section 3. The logarithm of the raw data sets is taken to transform the data to g_0 in %/cm. Laser gains as high as 3.6%/cm were observed in the DELILAH laser.

For the purpose of understanding the spatial dependence of the energy deposition into the discharge, model calculations were carried out to obtain the energy loading in the laser from the observed gains. Figure 5-6 shows how the gain depends upon energy loading, for the 828 isotope under E-beam and self-sustained conditions, and for a sample 826 line. All the gain data were analyzed by reading the energy loading corresponding to the observed peak gain appropriate from the curve in Figure 5-6 to derive the spatial dependence of the energy loading under various discharge conditions.

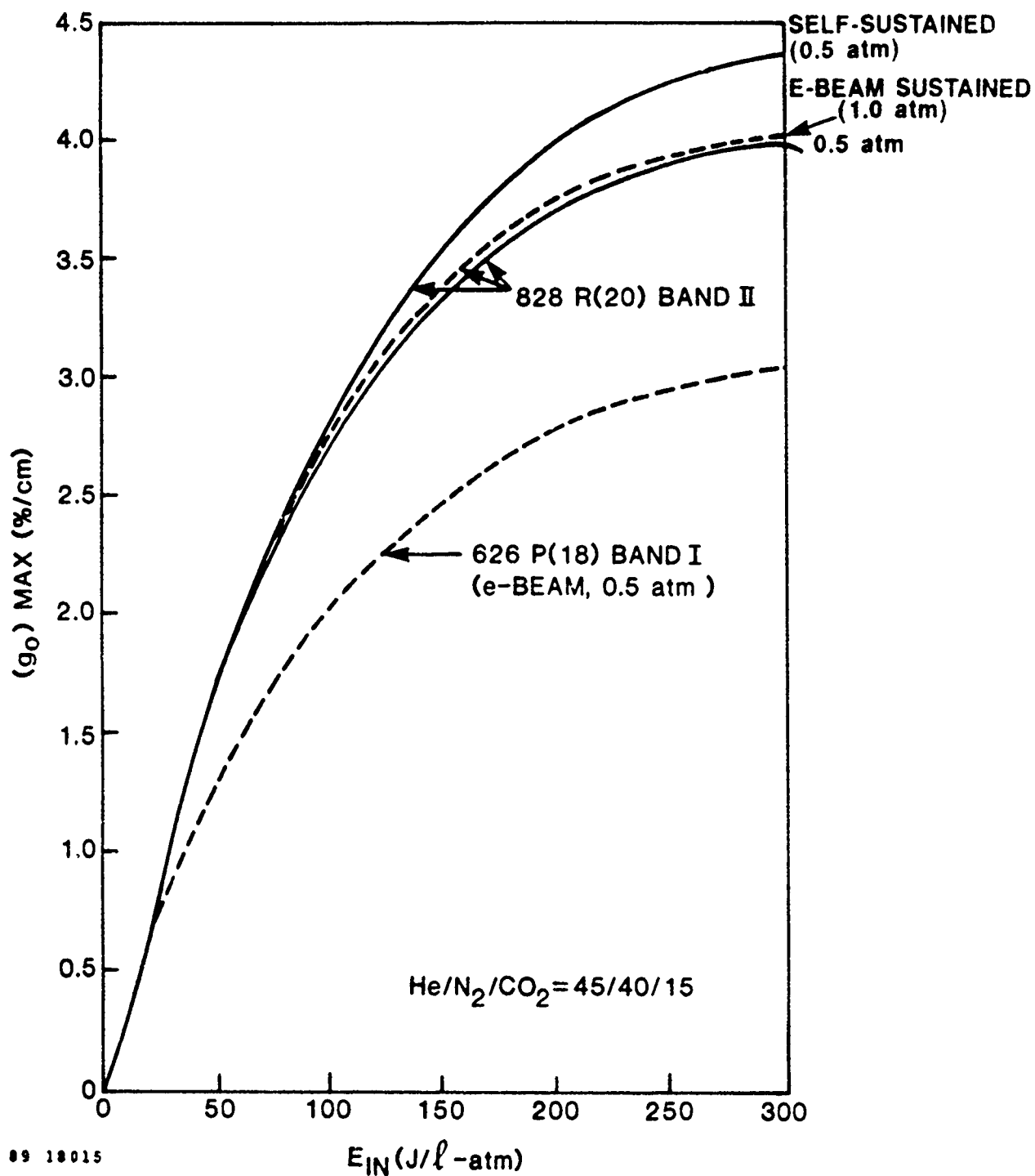


Figure 5-6. Model Predictions of the Peak Small Signal Gain as a Function of Energy Loading.

The energy loading as a function of the position between the electrodes is shown in Figure 5-7. The points connected by solid lines identify data collected on the centerline of the discharge, while dashed lines identify data collected away from the centerline, where the electron beam flux is less. It is easily seen that lower electron flux leads to lower energy loading in these regions away from the central axis. The results also reflect decreasing E-beam activity near the discharge anode, particularly in the data taken at 1-atm total pressure. The energy of the electrons produced by the plasma diodes is only 100 keV and will have even lower mean energies after transiting the foil and the drift region between the foil and the screen cathode. The electrons are, therefore, significantly attenuated and scattered by the gas in the laser. The measurements show that spatial homogeneity of the pumping is better under self-sustained conditions than E-beam sustained.

5.5 EXTRACTION MEASUREMENTS

5.5.1 Optical system and diagnostics

The laser cavity utilized the same optics as were used on the Lucy device, consisting of a grating (150 lines/mm, 9- μ m blaze) and an output coupler (radius of curvature 10 m, 80% reflectivity) arranged as a simple stable resonator. Although the dimension of the optics along the direction of the discharge exceeded the 4-cm electrode spacing, they could not extract the entire discharge width. The width of the grating limited the extracted region to 4.7 cm. The front mirror was also masked to a 4.7-cm width, both to define the extracted region and also to improve the wavelength purity of the extracted output. Based upon the results of the gain measurements, the extracted region included 75% of the energy deposited under self-sustained conditions, and 78% of the energy deposited when e-beam sustained.

Because of the difficulties with the laser waveform measurement encountered in the Lucy experiments, a different monitoring arrangement was employed for the DELILAH data. A NaCl beamsplitter coupled out a fraction of the laser output, directing it through a lens into a Cu integrating

sphere. A fast Ge: Au photodetector measured the laser temporal profile through a small aperture in the integrating sphere. The waveform from the photodetector was recorded by a Tektronix 2430 digital oscilloscope (a second Tektronix 2430 recorded the voltage and current waveforms) and stored by the IBM PC computer. The beam transmitted through the beamsplitter impinged upon the surface of a calibrated calorimeter connected to a chart recorder. The beamsplitter was calibrated by measuring the decrease it caused in the calorimeter signal when inserted into the output beam. The calorimeter and chart recorder were calibrated using a regulated power supply to apply a constant voltage to resistance wires inside the calorimeter. The results given here conservatively assume 100% absorption of the CO_2 laser radiation by the calorimeter; if the absorption were less, the actual extracted energies and efficiencies would exceed those reported here.

5.5.2 Extracted Energies and Efficiencies

Single-line extraction measurements were carried out on $^{12}\text{C}^{18}\text{O}_2$ in 80/10/10 He/ N_2 / CO_2 mixtures and 45/40/15 mixtures, extracting on either R(20) or R(24). The 45/40/15 mix is more characteristic of mixtures usually chosen for E-beam sustained lasers, but the 80/10/10 mixture was also measured to allow comparisons with the self-sustained results described in Section 4. Single-line extraction measurements were also carried out on the R(20) line of $^{12}\text{C}^{18}\text{O}_2$ at $9.11 \mu\text{m}$, in 45/40/15 mixtures. Measurements at both 1 atm and at 0.5 atm were performed on both isotopes.

Examples of the observed laser waveforms under e-beam sustained conditions are shown in Figures 5-3b and 5-4b (the corresponding current/voltage traces are Figures 5-3a and 5-4a). They show a gain-switched spike, a pulse several microseconds long and a decay dependent upon total pressure.

The loaded and extracted energies for the various isotopes, mixtures, and extracted lines are shown in Table 5-1. As was observed in the measurements on self-sustained discharges, the 80/10/10 mixtures are less efficient than the 45/40/15 mixtures. The difference in efficiency is

Table 5-1

R(20) SINGLE-LINE EXTRACTION FROM ISOTOPIC CO₂
EXCITED BY AN E-BEAM SUSTAINED DISCHARGE

Isotope	Mixture He/N ₂ /CO ₂	Pressure (torr)	Energy Loading (J)	Extracted Energy Total(J)	Intrinsic Efficiency(%)
626	80/10/10	380	82.7	8.2	9.9
626	45/40/15	380	101.0	11.0	10.9
828	45/40/15	380	98.6	10.7	10.9
828	45/40/15	380	130.3	15.2	11.7
626	80/10/10	760	103.3	9.4	9.1
626	45/40/15	760	1.2	20.0	9.9
828	45/40/15	760	203.4	20.4	10.0
828	45/40/15	760	248.7	25.7	10.3

R(24) Single-Line Extraction

626	45/40/15	380	97.7	9.9	10.1
626	80/10/10	760	103.4	8.3	8.0
626	45/40/15	760	186.6	18.3	9.8

related to the electron excitation efficiencies of the various vibrational modes of the laser gas, as will be discussed in Section 6. The 0.5 atm results show higher efficiencies than at 1 atm. This may be due to nonuniformities in energy deposition caused by electron-beam attenuation, as evidenced by the curves in Figure 5-7. In contrast to the self-sustained results obtained in the Lucy experiments, $^{12}\text{C}^{18}\text{O}_2$ mixtures do not show significantly different efficiency than $^{12}\text{C}^{16}\text{O}_2$ mixtures.

To further resolve the differences between self-sustained operation, as observed in the Lucy device and E-beam sustained operation studied in DELILAH, a few experiments using DELILAH as an E-beam preionized, self-sustained laser were performed. In these experiments, the e-beam was crowbarred simultaneously with the onset of the discharge pulse. The DELILAH laser is not well-suited to self-sustained operation, since the screen electrode is not smooth and might be expected to encourage discharge instabilities. Nevertheless, we found in our studies (carried out in 380 Torr of a 45/40/15 mix of the 828 isotope extracted on the R(20) line) that self-sustained operation yielded the same or slightly higher extracted energies and efficiencies than E-beam sustained operation.

To examine the differences more carefully, a series of laser shots were taken varying the E-beam flux, which alters the E/N of the discharge. The E-beam flux was varied by changing the helium pressure in the plasma diodes, which varies their impedance but makes little change in the electron energy spectrum they produce. The results are shown in Figure 5-8, where the efficiency (defined as the ratio of extracted to loaded energy) is plotted versus the E/N observed for the discharge. The vertical error bars are estimates of the relative errors of the measurements, while the horizontal error bars show the range of E/N predominating during the pump pulse. While there is some variation in efficiency, the relative variation of only about 5% over an E/N range of nearly a factor of three is surprising.

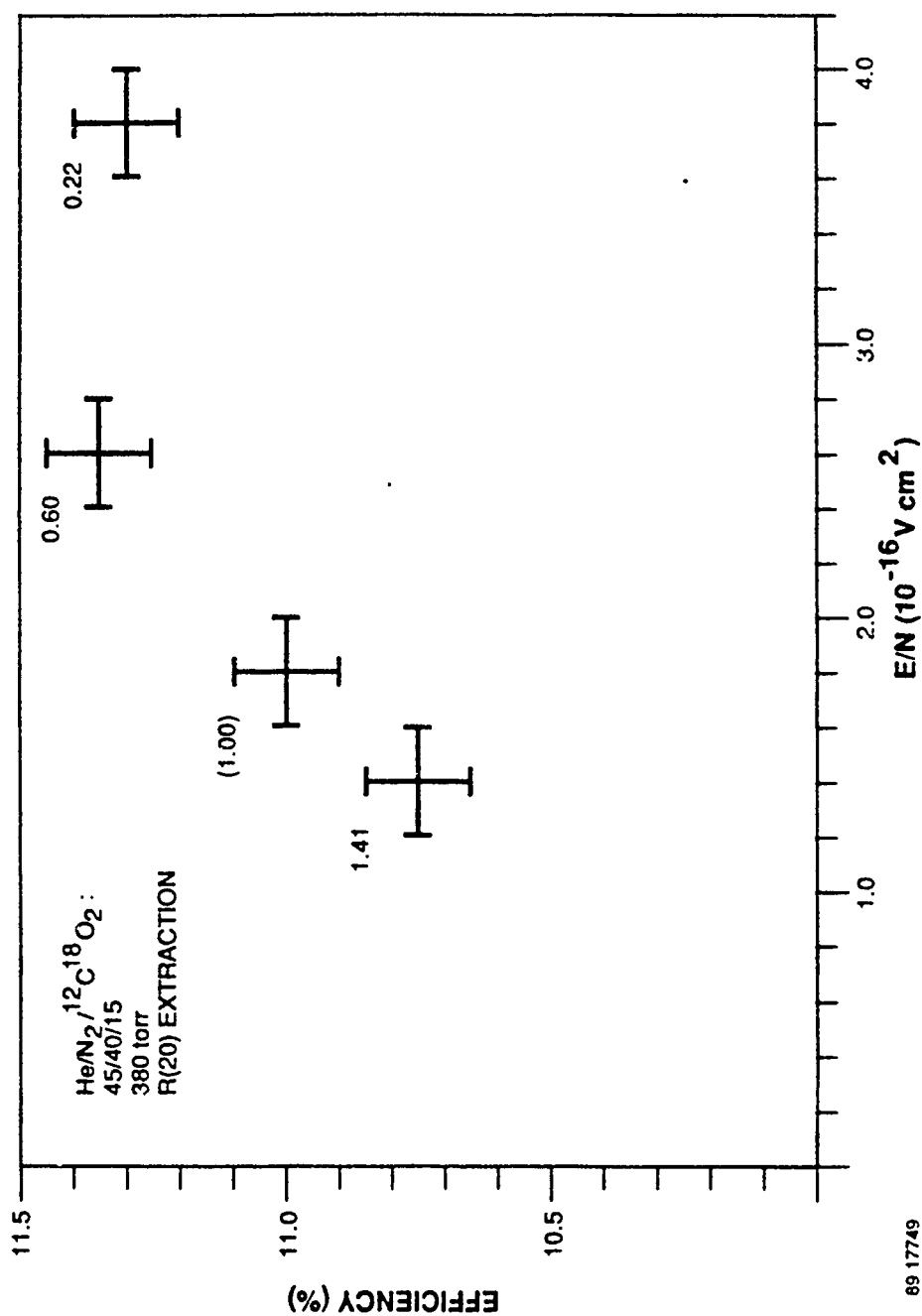


Figure 5-8. Efficiency vs. E/N for the e-Beam Sustained Discharge. The numbers in the parentheses show the e-beam flux relative to the value at $E/N = 1.8 \times 10^{-18} \text{ V/cm}^2$.

Many factors influence the relative efficiencies, including the fraction of energy deposited in the region extracted by the optics in each case, the details of the pump waveforms, the electrode shape and smoothness, and the appropriateness of the output coupling for each case. Direct comparisons of E-beam against self-sustained operation are therefore complex and many factors should be considered. The trade-offs between self- and e-beam sustained operation will be discussed fully in Section 6.

5.6 COMPARISON WITH MODEL

Correct computation of extracted energies was found to depend upon accurate energy deposition profiles of the type shown in Figure 5-7. Knowledge of the overlap between the extraction optics and the energy deposition profile is important, because energy was deposited in unextracted regions. When the distribution of energy deposition is derived from the gain distribution as described in Section 5.4, the STI CO₂ laser model reproduces the data well. The model has been benchmarked to actual ¹²C¹⁸O₂ extraction results, so accurate computations of extraction efficiency for other optical and discharge configurations will be practicable.

5.7 SUMMARY

Measurements comparing the gain and extraction efficiencies of mixtures containing the 826 and the 828 isotope were carried out under a variety of conditions in an electron-beam sustained laser. Good efficiency (properly accounting for limitations of the extraction optics) under single-line extraction conditions was obtained, with nitrogen-rich mixtures producing better results than lean mixtures. The performance of the 826 and the 828 isotopes were found to be very similar. The results suggest that for rich mixtures, the efficiencies under e-beam and self-sustained conditions are similar.

Section 6

DISCUSSION

6.1 INTRODUCTION

The choice of design architecture for an orbiting wind-sensing laser depends upon the intrinsic efficiency of the lasing gas under various excitation conditions. In this section, we first draw the comparison between pulsed, single-line operation of conventional $^{12}\text{C}^{16}\text{O}_2$ lasers with lasers operating on the $^{12}\text{C}^{18}\text{O}_2$ isotope. Then we discuss the influence of gas composition on the performance under self-sustained and e-beam sustained excitation, and the implications of these results for the design of pulsed laser oscillators.

6.2 $^{12}\text{C}^{18}\text{O}_2$ vs $^{12}\text{C}^{16}\text{O}_2$

Of fundamental importance are the gain and efficiency of pulsed lasers operating on $^{12}\text{C}^{18}\text{O}_2$. Previous studies* have shown that under cw excitation conditions, the gains of 828 laser lines are lower than the gains of comparable 626 laser lines. As discussed in Section 3, our measurements using pulsed excitation have shown higher gain for the 828 isotope than for the 626 isotope. This translated into better extraction efficiencies for 828 laser gas mixtures in measurements on the LUCY self-sustained laser.

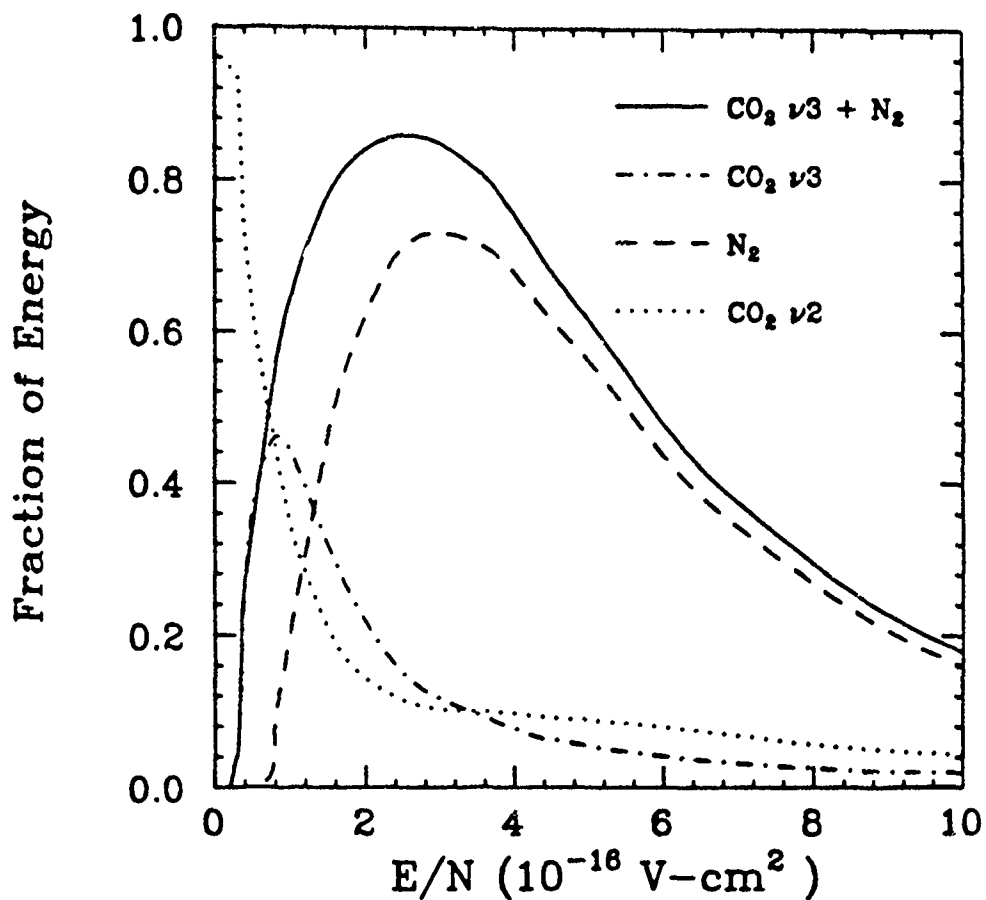
A similar enhancement was not seen under e-beam sustained conditions. It is possible that at the lower E/N values characteristic of e-beam sustained operation, the lower laser level of the 828 molecule is discharge-excited to a greater degree than the lower laser level of the 626 molecule, because the isotopic substitution drops the lower laser level.

6.3 GAS COMPOSITION EFFECTS

The pumping efficiency of the upper laser level depends upon the laser gas composition. Figure 6-1 shows how energy deposited by the discharge is proportioned among the various vibrational modes in the laser gas, for the 45/40/15 He/N₂/CO₂ mixture used in many of our experiments. The distribution depends upon the E/N of the discharge, with the most efficient pumping occurring at the maximum of the CO₂ (ν_3) + N₂ curve. Figure 6-2 compares the same CO₂ (ν_3) + N₂ curve with a similar curve for an 8/1/1 gas mixture. In an e-beam sustained discharge with a fixed impedance PFN, the E/N may be adjusted by variation of the electron beam flux. Self-sustained discharges operate at a specific E/N determined by the balance between ionization and attachment which is function of gas composition. Also shown in Figure 6-2 are the operating points for self-sustained discharge operation. Notice that at the self-sustaining E/N, energy is more efficiently deposited into the desired modes using the richer (higher N₂ + CO₂) mixture.

Figure 6-3 shows the Boltzmann code predictions for the fraction of energy going into CO₂ (ν_3) + N₂ vibration as a function of N₂/CO₂ ratio for three different He concentrations. Figure 6-3 shows that the enhanced efficiency of the 45/40/15 gas mixture under self-sustained conditions is not ascribable to the reduced He concentration, but instead to the higher ratio of N₂ to CO₂. The results indicate that for efficient operation, the concentration ratio N₂/CO₂ should be at least 2-3.

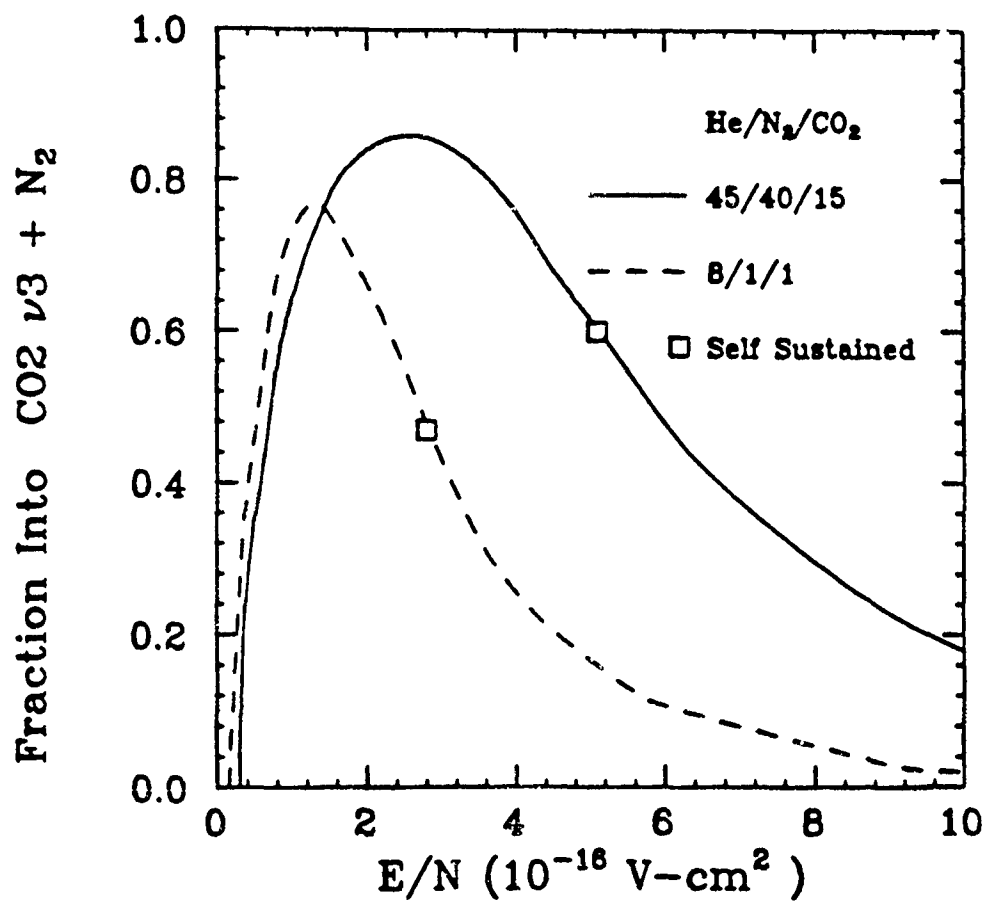
We have used the STI kinetics model updated with the results of the kinetics and extraction measurements for 828 CO₂ to investigate the configuration for a 10-J space-based CO₂ laser. For this preliminary investigation, a square excitation pulse with a duration of 5 μ sec was assumed. We have concentrated on the self-sustained discharge for this study because eliminating the high electron-beam diode make a much simpler system even though there is an efficiency advantage for e-beam sustained discharges. The efficiencies shown in the following figures are much lower than those reported in Sections 4 and 5 because realistic estimates of PFN energy transfer efficiencies and optical extraction efficiencies due to



DISCHARGE ENERGY DISTRIBUTION

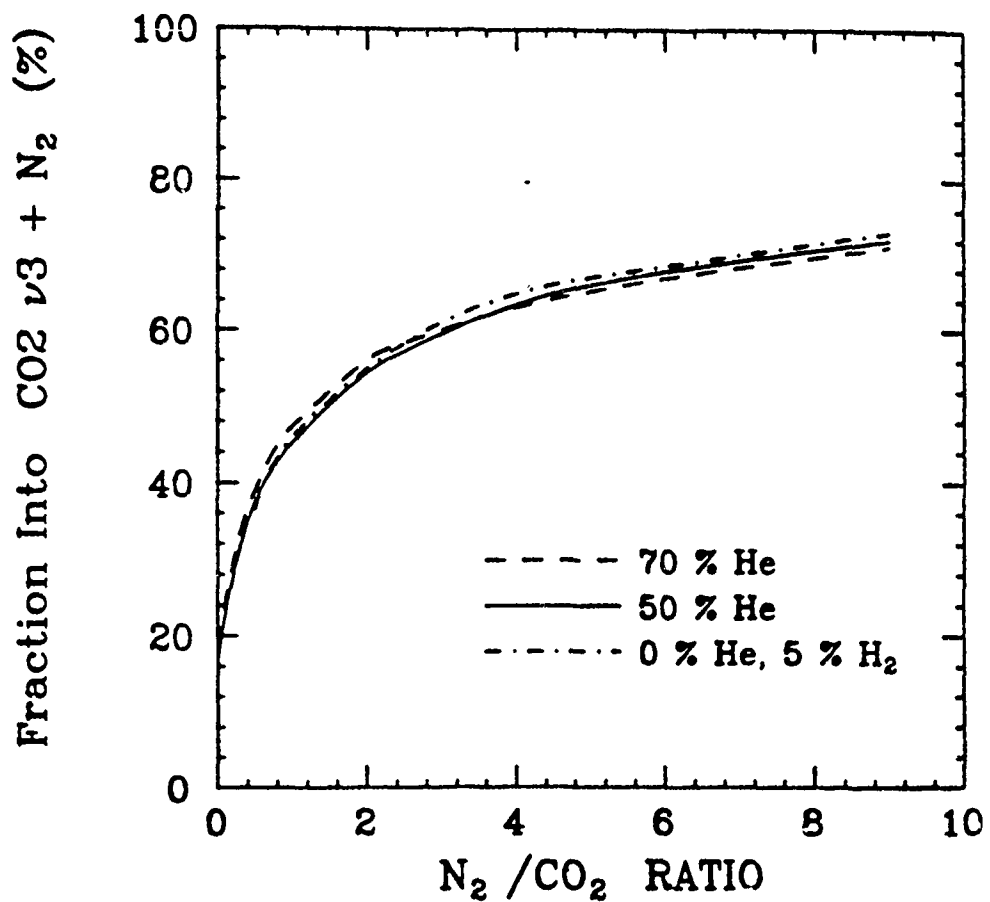
$$\text{He}/\text{N}_2/\text{CO}_2 = 45/40/15$$

Figure 6-1. Boltzmann Code Predictions Showing the Fractional Energy Distribution into the CO_2 and N_2 Vibrational Modes as a Function of E/N .



DISCHARGE ENERGY DEPOSITION

Figure 6-2. Fractional Energy Transfer into CO₂ ν₃ + N₂ Vibrational Modes as a Function of E/N for Two Gas Mixtures Used in the Experiments of Sections 4 and 5.



SELF-SUSTAINING DISCHARGE ENERGY DISTRIBUTION

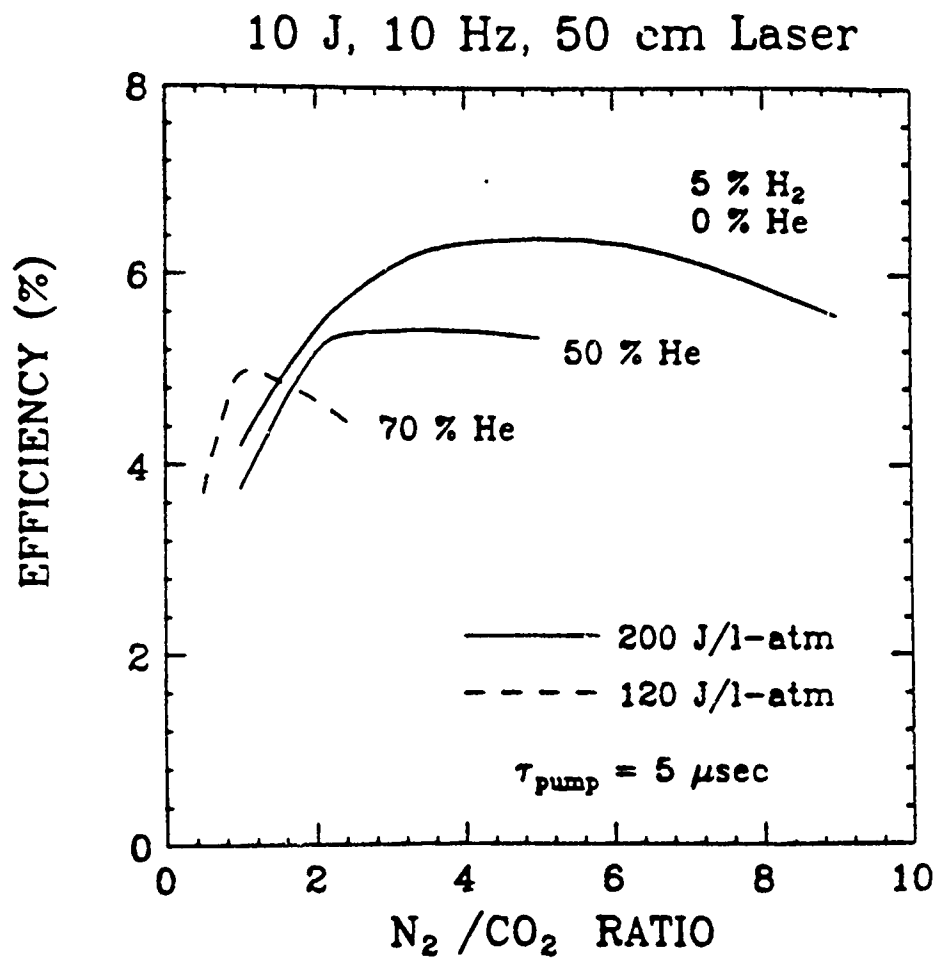
Figure 6-3. Fractional Energy Transfer into $\text{CO}_2 \nu_3 + \text{N}_2$ Vibrational Modes as a Function of N_2/CO_2 Ratio for Three He Concentrations.

extracting a circular beam from the rectangular discharge aperture and leaving guard bands for acoustical disturbances have reduced the efficiency from the maximum achievable. Calculations were done for both 0.5 and 1 atm; however, even though 10 J can be obtained from a smaller aperture at 1 atm, the acoustical guard bands not extracted represent a larger fraction of the aperture resulting in lower system efficiency. In addition, the higher pressure requires a higher PFN voltage, which is less desirable from the system point to view.

Using the complete STI laser model, efficiencies under practical extraction conditions can be calculated. The overall efficiencies of 50-cm long lasers providing 10-J pulses were computed, assuming 78% PFN energy transfer efficiencies and assuming a practical set of extraction conditions. These conditions assumed extraction of a circular beam (from a square discharge region) with an annular "guard band" (unextracted region) a few millimeters wide to block the areas of acoustically-disturbed gas at the discharge boundaries. The actual discharge area was varied with the operating conditions to maintain the 10-J output parameter.

Efficiencies for self-sustained systems determined in this way are shown in Figures 6-4 and 6-5. Clearly the highest overall efficiency is obtained for gas mixtures containing little or no He, with relatively high N_2/CO_2 ratios. Further insight is provided by Figure 6-5, where the mixture containing no He is the most efficient. The drop in efficiency for large energy loading is due to the larger relative area of the guard bands as the aperture is reduced to maintain 10-J output.

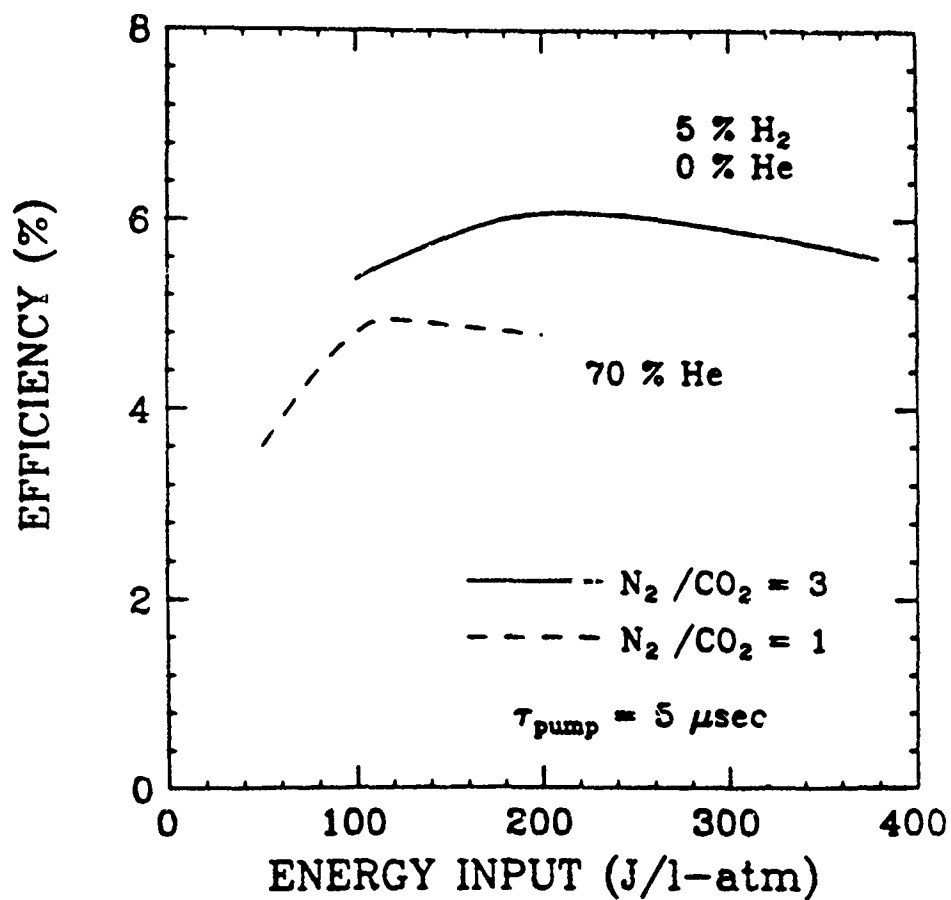
Since the pulse shape is important to the wind-sensing mission, the optical pulse waveform was computed for a variety of gas mixtures, assuming a square excitation pulse. As seen in Figure 6-6, the 5/71/24 $H_2/N_2/CO_2$ mixture produces a desirable pulse shape, in addition to high efficiency. It has a smaller gain switched spike and a faster decay after the pump pulse terminates putting more of the energy in the flat-top portion of the pulse.



Self-Sustaining, 828 R(20) 9.1μ , 380 torr

Figure 8-4. Projected Laser System Efficiency as a Function of N_2/CO_2 Ratio for Three He Concentrations.

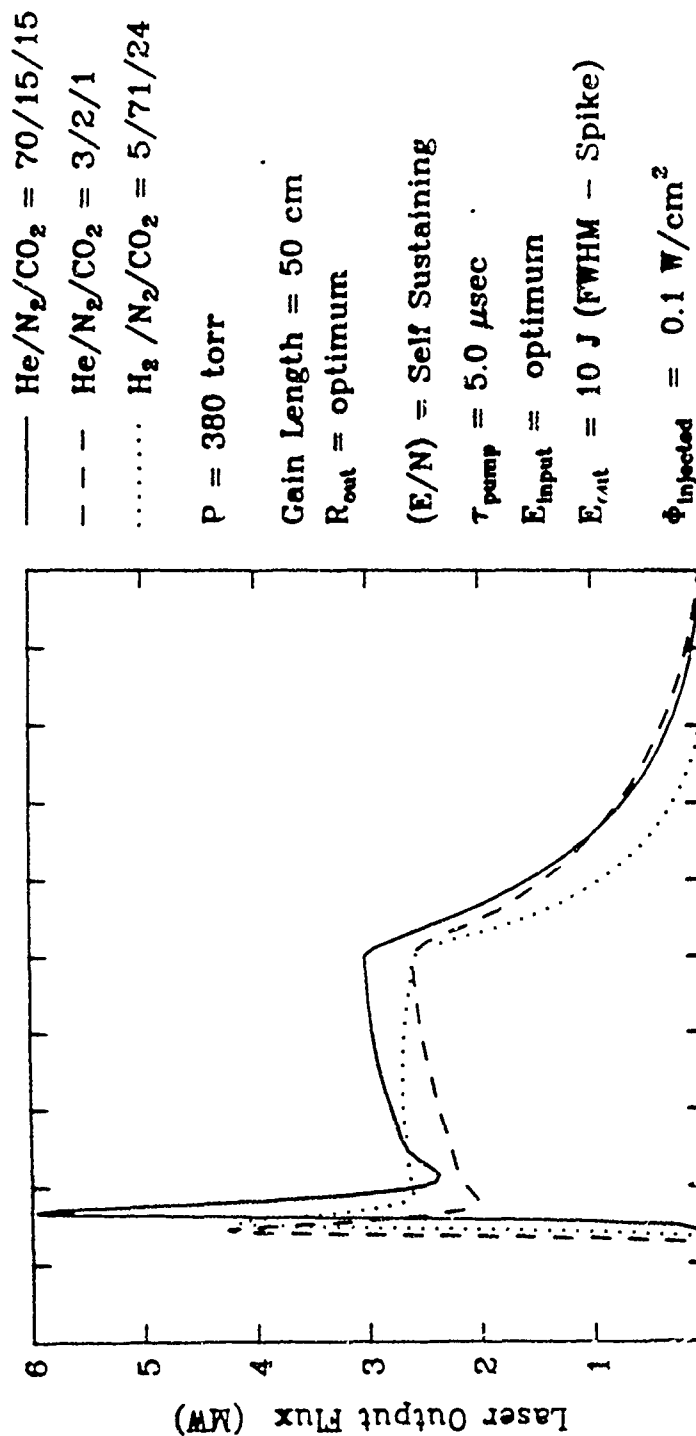
10 J, 10 Hz, 50 cm Laser



Self-Sustaining, 82% R(20) 9.1 μ , 380 torr

Figure 8-5. Projected Laser System Efficiency as a Function of Pump Energy for Two Gas Mixtures.

THEORETICAL LASER OUTPUT FLUX on 828 II-Band R(20)



Time (μsec)

Figure 6-3. Predicted Laser Pulse Shapes for Three Gas Mixtures, in a Self-Sustained Discharge Lasers.

The design study indicates that the most desirable gas mixture from both an efficiency and pulse shape aspect is the zero He mix with a 3:1 $N_2:CO_2$ ratio. This mix can also handle large energy loading without large adverse effects from gas heating. However, the required charge voltages are high due to the high N_2 and CO_2 concentrations and the effects of frequency chirp have not yet been evaluated. Our modeling indicates that at 0.5 atm, a 5 x 5 x 50-cm discharge would produce 10 J even with allowances for guard bands and extracting circular beams from a square aperture.

In addition, the experimental measurements and the modeling efforts indicate that the energy extraction and efficiency for 828 CO_2 II R(20) should be comparable or better than for 628 IP(18). The only difficulty may arise from isotope exchange between the reactive ^{18}O atoms produced in the discharge and ^{18}O atoms in the laser construction materials. Our preliminary results show that this exchange may be minimized for short times by reducing all the laser surfaces with H_2 and then treating them with $^{18}O_2$. However, much work is needed to show that a closed cycle laser using $C^{18}O_2$ can be operated sealed off for the long times and large numbers of shots ($\sim 10^9$) required for a space-based CO_2 wind lidar.

REFERENCES

1. Frederic E. Volz, "Infrared Optical Constants of Aerosols at Some Locations," Appl. Opt. 22, 3690 (1983).
2. Robert A. McClatchey and John E.A. Selby, "Atmospheric Attenuation of Laser Radiation from 0.76 to 31.25 μm ," AFCRL Technical Report AFCRL-TR-74-0003, AD779726
3. L.S. Rothman and L.D.G. Young, "Infrared Energy Levels and Intensities of Carbon Dioxide - II," J. Quant. Spec. Radiat. Transfer 25, 505 (1981).
4. L.J. Kieffer, "A compilation of Electron Collision Cross Section Data for Modeling Gas Discharge Lasers," JILA Information Center, Report #13, University of Colorado, Boulder, Colorado, 30 Sept. 1973.
5. R.L. Taylor and S. Bitterman, "Survey of Vibrational Relaxation Data for Processes Important in the $\text{CO}_2\text{-N}_2$ Laser System," Rev. Mod. Phys. 41, 26 (1969).
6. "High Energy Pulsed Laser," Final Technical Report, AVCO Everett Research Lab, March 1979.
7. R.K. Brinacombe and J. Reid, "Measurements of Anomalous Gain coefficients in Transversely Excited CO_2 Lasers," IEEE J. Quantum Electron., QE-19, 1674 (1983).
8. M.S. Abubaker and J.H. Shaw, "Carbon Dioxide Band Intensities and Linewidths in the 1-12- μm Region," Appl. Opt 25, 1196 (1986).
9. K. Siemsen, NRC Canada, Ottawa, Ontario K1A 0R6 Canada (private communication-1987).
10. L.E. Freed, C. Freed and R.G. O'Donnell, "Small Signal Gain and Saturation Intensity of $00^0_1\text{--}[10^0_0, 02^0_0]_{\text{I}}$ and $_{\text{II}}$ Vibrational Band Transitions in Sealed-off CO_2 Isotope Lasers," IEEE J. Quantum Electron., QE-18, 1226 (1982).